Control of the Electrical Transport through Single Molecules and Graphene

Dissertation
zur Erlangung des akademischen Grades
doctor rerum naturalium
(Dr. rer. nat.)

im Fach: Physik

Spezialisierung: Experimentalphysik

eingereicht an der
Mathematisch-Naturwissenschaftlichen Fakultät
der Humboldt-Universität zu Berlin
von
Dipl. Phys. -Ing. Christian Seifert

Präsidentin der Humboldt-Universität zu Berlin
Prof. Dr.-Ing. Dr. Sabine Kunst

Dekan der Mathematisch-Naturwissenschaftlichen Fakultät
Prof. Dr. Elmar Kulke

Tag der Verteidigung: 15.02.2018

Gutachter: Prof. Dr. J.P. Rabe
Prof. Dr. W. Treimer
PD Dr. A. Opitz

Zusammenfassung

Der Erste dieser zweiteiligen Arbeit befasst sich mit der STM Untersuchung einer Grenzschicht in umgebender natürlicher Atmosphäre, welche sich durch die Adsorption des leitfähigen Graphen auf einer Glimmeroberfläche ausbildet. Durch die umgebene Luftfeuchtigkeit interkalieren Wassermoleküle in diese Grenzschicht. Durch die Variation der umgebenen relativen Luftfeuchtigkeit gibt diese Wasser ab bzw. nimmt auf, und es manifestieren sich sternförmig wachsende Fraktale, in denen Graphen etwa um den Durchmesser eines Wassermoleküls an Höhe absinkt. Die STM Untersuchung, welche primär sensitiv auf die Zustandsdichte von Graphen reagiert, zeigte, dass sich scheinbar, anders als in den SFM Untersuchungen, zusätzliche signifikante Höhenänderungen von Graphen innerhalb der Fraktale bildeten. Dieses deutet auf eine Wasserschicht hin, welche Domänen mit signifikant unterscheidbaren Polarisationsrichtungen aufweisen, welche die Zustandsdichte von Graphen verändern kann. Dies ist aber gleichbedeutend mit der Annahme, dass sich in jener Grenzschicht mindestens zwei oder mehr lagen Wasser bilden müssen.

Im zweiten Teil befasst sich diese Arbeit mit der STM Untersuchung einer funktionalisierten Oberfläche die charakterisiert ist durch eine leitende Oberfläche (Graphen und HOPG) adsorbierten funktionalisierte Dyade an einer Fest-Flüssig Grenzfläche, welche ebenfalls mit einem STM untersucht wurde. Diese Dyade besteht im Wesentlichen aus einem Zink-Tetraphenylporphyrin (ZnTPP) und mit diesem über einem flexiblen Arm verbundenen Spiropyranderivat. Letztere ändert seine Konformation durch die Einstrahlung mit Licht geeigneter Wellenlänge, womit sich gleichfalls das Dipolmoment sehr stark ändert. Es zeigte sich, dass das Schaltverhalten auf einen Graphen basierenden leitenden Oberfläche mit dem Schaltverhalten einer Dyade, welche sich frei beweglich in Lösung befindet, vergleichbar ist. Dieses lässt den Schluss zu, dass das Schalteigenschaften einer einzelnen Dyade auf das adsorbierte Kollektiv übertragen werden kann, da es keine signifikanten beeinflussenden Wechselwirkungen durch die leitende Oberfläche und der benachbarten Dyaden auswirkte.

Abstract

The first of this two-part work deals with the STM investigation of an interface in the surrounding natural atmosphere, which is formed by the adsorption of the conductive graphene onto the mica surface. In this interface, water molecules may intercalate by the surrounding humidity. By varying the relative humidity, the interface is rewetted, respectively, dewetted and it manifests itself in a star shape growing fractals, where the height of graphene is decreased by approximately the diameter of one water molecule. The STM investigation - which is primarily sensitive to the density of states of graphene - shows that additional significant changes in the height of graphene are formed within the fractal, unlike in the SFM investigations. This suggests that there is a water layer by which the density of graphene is differently affected by domains with significant distinguishable polarisation alignments. However, this is equivalent to the assumption that there are two or more water layers exist within the interface.

The second part of this work deals with the STM investigation of a functionalized surface characterised by a functionalized dyad adsorbed onto a conductive surface (graphene and HOPG) at a solid-liquid interface. This dyad essentially comprises a zinc-tetraphenylporphyrin (ZnTPP) and is connected with a spiropyran derivative via a flexible linker. This changes its conformation through irradiation with light with a suitable wavelength, by which the dipole moment is also strongly changed. It was found that the switching behaviour of a graphene-based conductive surface is comparable with the switching behaviour of a dyad, which itself can move freely in solution. This leads to the conclusion that the switching properties of a single dyad can be transmitted to its collective because it affected no significant influence interactions by the conductive surface and the adjacent dyads.

CONTENTS

1. Introduction

Microelectronics play an essential role, directly or indirectly, in life of human beings. Almost all technologies and services are influenced and characterized by microelectronics. This influence cannot be and should not be avoided. The main prerequisites in this technology for their development are the miniaturization and, for functional units, the enhancement of functions itself. The miniaturization takes into account the limits which are set by quantum mechanics (see Fig. 1).

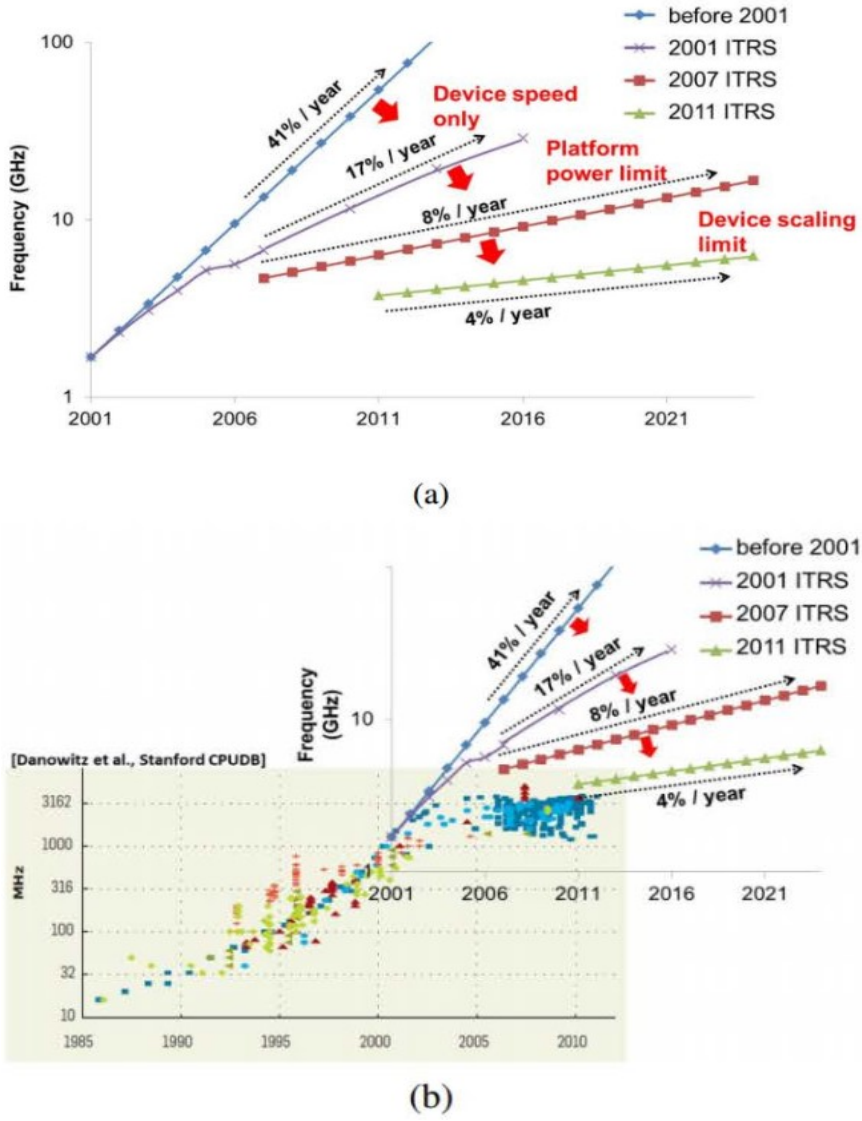

Figure 1. ITRS (online report 2013) data collection and forecast of "Moore's Law"; (a) Evaluation of the "ITRS frequency roadmap". (b) Overlay of the ITRS frequency roadmap with data from the Stanford CPUDB repository.

1. Introduction

According to the reports of the International Technology Roadmap of Semiconductors (ITRS), the long term development will be only determined by quantum mechanics [1–4]. New materials, manufacturing techniques and methods are needed. Due to the structure dimensions that shrink continuously, the ratio of the surface and the interface to its enclosed volume must be taken into account, for example. This ratio will be increased, whereby the properties of composites are determined more and more by interface and surface phenomena. The definition of interfaces or surfaces itself and their dimensions are mainly determined by the considered phenomenon (corrosion/oxidation, biological membrane, diffusion, transport, catalysis, etc.). Inspired by nature, molecular devices offer a variety of opportunities to achieve these goals. Inter alia, the functionalized surfaces constitute a highly interesting field of organic interface and surface physics. They are already exerting a strong influence in the fields of electronics [5–9] and biology, particularly medicine [10–12]. Based upon the interest, success and the outstanding opportunities, the impact will continue to increase in the coming years and decades. However, this key technology is dependent on the knowledge about surface and interface physics, since this knowledge is - beside other mentioned reasons - essential for the intended design and production of micro and nano devices. When considering the established semiconductor technology based on inorganic materials and well known production methods, it is necessary to recognize that the combination of features and characteristics of inorganic and organic matter is a logical and promising way to add this hybrid technology to semiconductor technology. One has to investigate the effects, functions and interaction mechanisms on molecular and atomic scales, to design and construct the devices in a well defined manner. The ambient conditions play an essential role (air, water, solvent, etc.). Therefore, it is required to use suitable measurement methods, because amongst other features in the measured signal, included details of individual events and their interaction mechanisms will remain hidden due to statistical averaging. Decisive contributions for studies in such small dimensions have been provided by G. Binnig, H. Rohrer, C. Gerber, E. Weibel and C. F. Quate with the development of the scanning tunnelling microscope (STM) in 1982 [13] and the scanning force microscope (SFM) in 1986 [14].

This thesis includes two parts, at first the investigation of a graphene-mica interface and its potential interaction mechanisms and secondly, the investigation of a functionalized surface, determined by a switchable dyad which is physically adsorbed onto graphene.

1.1 STM Investigation of a graphene-based Interface

Graphene, which is physically adsorbed onto mica, is determined by the surrounding atmosphere and its conditions. Water molecules may be intercalated between Mica and Graphene and constitute therefore slit pores, a few angstroms thin. The graphene and its local density of state (LDOS) may be affected by the interaction with the underlying layers, whereby the mutual influence may be indirectly measured with the STM. There are already investigations where the influence of the relative humidity (RH) on the dewetting and rewetting process of the slit pore are described, but its fundamental mechanisms are not yet completely understood [15–19]. An important means of clarifying these issues is also to determine the number of water layers, which is still an open question. An additional motivating factor comes from the fact that one also gets more information on microscopic interactions by the macroscopic thermodynamic variables. The water can be removed via reducing the RH, whereby structures appear in the shape of fractals, which always have the same depth through measurements by a SFM. However, the water cannot be completely removed via the RH rather the fractal growth stopped at a finite value unequal to zero. This suggests a mechanism where the sum of all mechanisms and their energies within the system have a global energetic minimum (balance of power) at room temperature, $kT \approx 25$ meV. Chapter 4.2 deals with this topic and expands the investigations, concerning the causes of this phenomenon, by STM.

1.2 STM Investigation of self-assembling and switch behaviour of the spiropyran-porphyrin dyad on graphene and HOPG

The production methods of interfaces and surfaces are principally distinguished in two types, namely top-down (TD) and bottom-up (BU) [20]. The TD method is used - for example - in the manufacturing of integrated electrical components. It constructs from large basic structures smaller structures with functional units. This is primarily limited by the structuring processes. For example, the photolithography is limited by the used wavelength, printing systems and photo lacquer. However, the BU method organises and arranges smallest functional units to larger units, components and devices. the mRNA (messenger Ribonucleic acid) is the program whereby the amino acids - the functional units - are organised and arranged to proteins. In comparison to the TD method, this offers the advantage that functional structures are possible at the molecular and atomic scale. Molecules - as the smallest units - are arranged on a surface to self-assembled mono- and multi-layer (SAM) by the intermolecular interaction and thus constitute a functional surface [21–27]. The production of SAMs begins with the adsorption of molecules and their spontaneous

assembling from the gas or liquid phase to a well-defined structured and - in view of the purpose of this work, i.e. chemisorption will not be considered here - non-covalently bonded aggregation (physisorption) on top of a molecular-specific surface, in which the intermolecular interaction between molecule and surface plays an important role [28]. However, in this constellation, these interaction mechanisms can lead to a change in the properties of the adsorbed molecules [29–39]. The second part of the thess is about the investigation of a switchable spiropyran-porphyrin dyad adsorbed onto HOPG and graphene: The porphyrin derivate (zinc-tetraphenylporphyrin, ZnTPP) works as an anchor and spacer, whereby nitro-spiropyran is covalently attached, switchable via light with a suitable wavelength. The nitro-spiropyran has a dipole moment that is strongly changeable via the conformational change of the isomerisation (SP↔MC) [35]. As a result, the dyad can more or less strongly interact with the surface and the adjacent dyads and thus the switching behaviour is affected more or less, respectively. The dyad has been investigated, concerning the self-assembling and switching behaviour, by the STM.

2. Basics and Methods

2.1 Introduction

This work aims to investigate self-assembled molecular layers that interact with surfaces and interfaces. Such a system has its own, remarkable characteristic properties, which were investigated with the measurement methods of Scanning Probe Microscopy (SPM). This chapter is separated into two sections: the first part deals with the molecular bonds and the interaction mechanisms, e.g. van-der-Waals (vdW), hydrogen bonds, covalent bonds, etc., and at the end of the second part, the measurement methods are considered.

2.2 Molecular Bonding

Atomic bonds are determined via the positively charged cores and their surrounding electrons, although this environment primarily refers to the valence electrons. The latter are primarily subject to an interaction (compare e.g. ionisation energy IE and electron affinity EA). There are different ways to distinguish between bonding types, depending on the bond strength, the directional dependence of the bonds, the character of the collective electron wave function, the range of interaction force and the number of the binding partners. An overview of the chemical binding types and bonding strengths is shown in Fig. 2.1 and Tab. 2.1. An additional expedient way to distinguish them is the spatial structure of molecules, which is important for the properties and functional properties (compare it with a steric hindrance). At the first level, one defines the chemical equation as the primary structure. In this way, a special spatial arrangement with symmetries, helicities, etc. can be constituted, called the secondary structure. Larger molecules are able to fold themselves, since the bonds are not absolutely fixed in the orientation. These folded and turned molecules are designated as their tertiary structure. In an ensemble of such molecules, intermolecular bonds are possible which are designated as quaternary structures. Here, for example, it is important to note that for proteins the sub-division starts with the base pair-sequences as the primary structure; and the additional structures and their properties are formed during the synthesis.

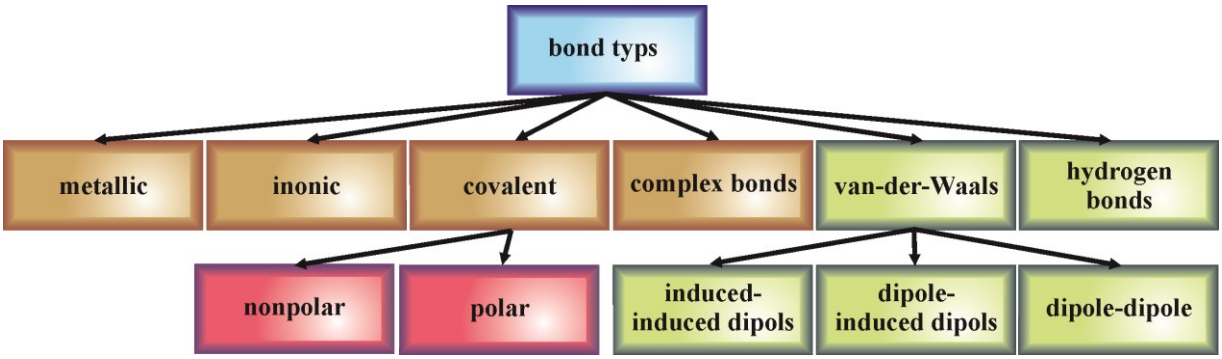

Figure 2.1a Overview of the bonding types.

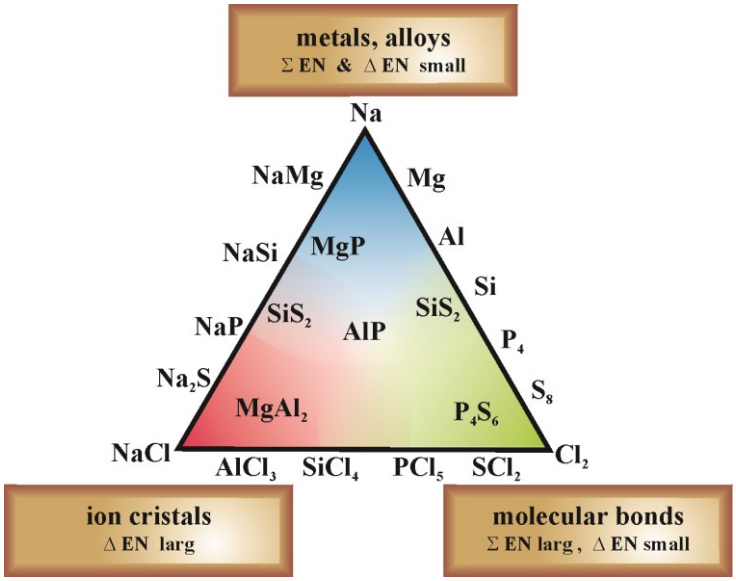

Figure 2.1b (van Arkel-Ketelaar triangle of bonding) The triangle illustrates the proportions of the bond types for a few examples. Only very few materials can be assigned a pure bond type: in most cases it is a combination of two or even three.

Table 2.1 Overview of the most important inter- and intramolecular bond types, their energy and the equivalent photon wavelength.

chemical bond	binding energy (eV)	equivalent photon wavelength (nm)	
van-der-Waals	$40 \cdot 10^{-3}$ - $80 \cdot 10^{-3}$	31100 - 15300	infrared
hydrogen bonds	1.0 - 3.0	950 - 410	IR, visible light
ionic bonds	2.0 - 4.0	620 - 310	visible light, UVA
covalent bonds	2.0 - 7.5	560 - 160	visible light, UVA-UVC

Figure 2.1a shows the sub-division of the different bonding types. Moreover, the illustration suggests that there are sharp limits of their definition. A combination of types can be found in most systems (seee Fig. 2.1b). The metallic bonds are determined via periodically arranged positively charged atom ions and their delocalised quasi-free, movable valence electrons, whereby the binding electrons are described via collective wave functions over the entire crystal. The orientation of the bonds is non-directional. This microscopic characteristic defines the macroscopic properties such as electrical conductivity, metallic lustre and ductility. The collective wave function manifests in an equivalent description in the k-space given by a Fourier transformation. The real crystal is described via an equivalent crystal in the k-space where many properties may be described or even can be read directly by means of the Fermi surface or the dispersion relation. The ionic bond is based upon a strong ionization of atoms. As in strongly heterogeneous systems (e.g. 1st or 2nd with 6th or 7th group of the PTE, respectively), the atoms differ in their electronic properties which can also be determined by their parameters, such as electron affinity EA, ionisation energy IE or electronegativity EN. The descriptive wave function of the bonding electrons is very heterogeneously distributed between the bonding partners, whereby it generates strong electrostatic fields which in turn contribute to the ionic bonds (charge neutrality). The alignment of the bonds is not firmly oriented since the electrostatic fields are homogenous and thus lead to the densest packing within a unit cell. Even here, there are tendencies towards combinations of partially metallic and covalent bond characteristics. The third important group of chemical bonds constitutes the covalently bound atoms. If two potential bonding partners become closer, there is an inevitable overlap of their wave functions of the valence electrons. Concerning single atoms, the primarily involved wave function is the occupied s-, p-, d-orbital, etc. of each atom. This overlap is not only limited to one, but rather may be affected by several orbitals (hybridization). At the first order of approximation, the combined wave function is a superposition of single electron wave functions of each atom, whereby there are new mutual wave functions and correspondingly new designations such as σ-, π-, δ- orbitals, etc. The orbitals additionally obtain the indices u or g for unsymmetric or symmetric, respectively. However, there are different nomenclatures of the designation of molecule orbitals, as shown in Fig. 2.2.

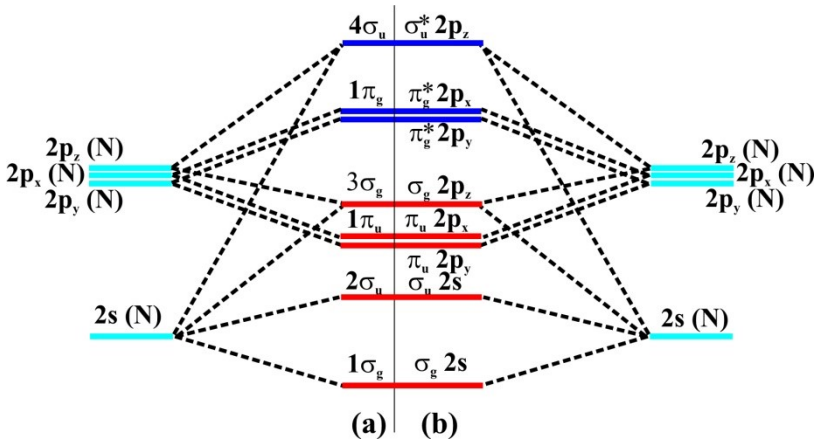

Figure 2.2 The energy scheme shows the orbitals of the N_2 molecule and its designation. Left and right are the single atom orbitals (N) and in the centre the N_2 with its two main designations.

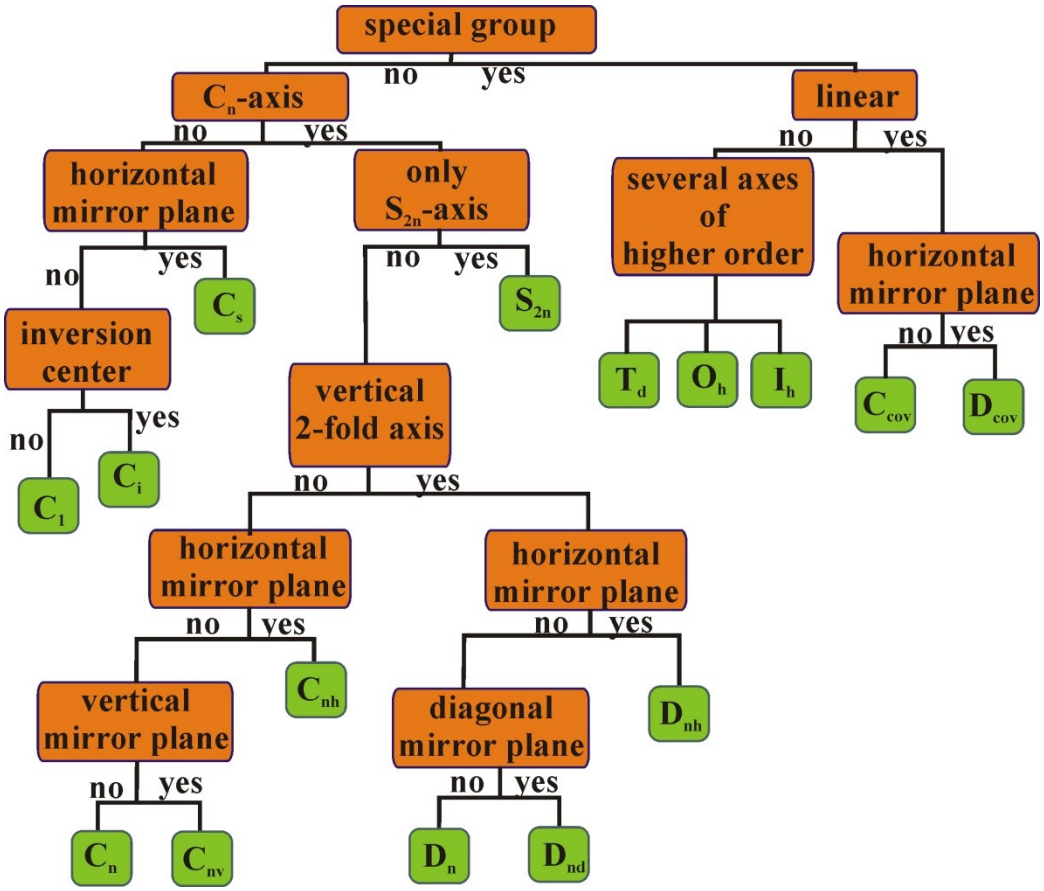

Figure 2.3 The crystallographic point groups according to Schönflies. As examples: **C_n** contain only an n-fold rotation axis; **C_{nh}** contain - additionally to the n-fold axis - a single mirror plane perpendicular to the axis of rotation; **S_n** contain only an n-fold rotation axis mirror; **D_{nh}** (they have the highest symmetry) contain all the elements of **D_n**, and an axis perpendicular to n-fold axis mirror plane.

The example is the energy scheme of the N_2 molecule. On the left and right, atomic nitrogen (N) is shown (bright blue). Each s-orbital is doubly occupied and the p-orbitals are singly occupied, as indicated via the black arrows. The centre constitutes the energy level of the N_2 molecule with its different nomenclatures (Fig. 2.2; "$1\sigma_g$" is equivalent to "σ_g 2s", where the star "*" indicates the non-bonding levels). Here, the bonding orbitals are marked red and the anti-bonding orbitals are marked blue. This nomenclature is useable for single bonds, although with complex, large but limited MOs as well as crystals, such as graphene or HOPG, availing the symmetry properties. The former is described by Schönfließ (Arthur Moritz) and the latter by Hermann Mauguin. The terminology of the symmetry point groups - i.e. the collection of symmetry operations (SO) on an object - is shown in Fig. 2.3.

The symmetry groups are based upon the symmetry of the Hamilton operator. The action of the Hamilton operator can be understood from the corresponding molecular symmetry point groups. By this means, the description of several systems with symmetry behaviour is simplified without knowledge of the exact equations of these systems. Based upon the symmetry groups, the corresponding equations of the system can be set up. The third description is equivalent to the description of metallic bonds over the reciprocal space by its periodical behaviour and thus allows the description of covalent bonded crystals, e.g. semiconductors. Another bonding type is the complex bond, a synonym is coordination chemistry. This is related to the covalent bonds. However, in contrast, the complex is defined by its Lewis base(s) and the Lewis acid. Well-known representatives include chlorophyll and haemoglobin, including the incorporated porphyrin derivatives. In most cases, the central parts are metal atoms and their corresponding ions (electron pair acceptor). The ligand frequently provides the electron pair (electron pair donator). The complex compound constitutes a Lewis-acid-base reaction and may be electrically neutral or charged in the corresponding solvent. Through the corresponding electron orbitals of the central particle, the coordinative bounds are formed over the corresponding ligand orbitals. The next bond type to be considered is the hydrogen bond. This type is primarily formed by a covalently bound hydrogen atom - which is thus partially positively charged - and another bound atom that provides an electron pair. This bond is primarily determined by an electrostatic effect and one of the weakest bond types. The last type is the van-der-Waals (vdW) bond. The vdW interaction is sub-divided into three mechanisms: the "induced dipole - induced dipole" (a), the "dipole - induced dipole" (b) and the "dipole - dipole" (c) interaction mechanism. The former ones are formed from atoms or molecules where the dipole moments are zero in the temporal average and when they are far away from each other. In the near field, the pairs can affect each other by the moving electron clouds,

whereby the mutually induced dipole moments and thus the related interaction and the total energy decrease. Accordingly, the binding energy increase. The designation "near field" is based upon the interaction range of the mechanism and has a dependency of r^{-6} in this case. This interaction mechanism is the weakest binding type. In case one partner already has a dipole moment in the temporal average, it induces a corresponding dipole moment in the other partner in the near field. The interaction range is larger than in the latter case. The strongest vdW interaction occurs between dipole and dipole. The mathematical descriptions are shown in the following equations.

a) $$V_{ind,ind} = -\left(\frac{1}{4\pi\varepsilon_0}\right)^2 \frac{3he\alpha_1\alpha_2}{8\pi\sqrt{m}\left(\sqrt{\frac{\alpha_1}{N_1}}+\sqrt{\frac{\alpha_2}{N_2}}\right)}\frac{1}{r^6} = -\frac{B}{r^6} \quad [2.1a]$$

b) $$V_{dip,ind} = -\frac{\alpha_1\mu_2^2+\alpha_2\mu_1^2}{(4\pi\varepsilon_0 r^3)^2}(3\cos^2\gamma + 1) \quad [2.1b]$$

c) $$V_{dip,dip} = -\frac{\mu_1\mu_2}{4\pi\varepsilon_0 r^3}(1 - 3\cos^2\gamma) \quad [2.1c]$$

Equation (2.1a) represents the case of two atoms or molecules where their temporal averages of the dipole moments are neutral in far distance to each other and at closer distance, with a r^{-6} dependence, permanent dipole moments are formed. Their interaction strength and the binding energy are primarily dependent on the mutual polarizabilities α_i. Anyway, the binding energy is very weak, with the very small Planck constant h and the electron charge e. The constant B may be identified with the variable in equation 2.2.b. The polarizability is determined - for example - according to Clausius-Mossotti's equation or Slater-Kirkwood [36]. 2.1b (Debye energy) μ_2 is the induced dipole moment by the permanent dipole moment μ_1, whereby a dipole moment is also induced in 1.

The physical cases that occur in this work are related to the interaction between surfaces and their emerged, intercalated molecular layers. Additional, adsorbed molecules on the top of a conductive surface ought not be excluded and can also more or less strongly interact with each other. All of these involved interaction mechanisms are collectively referred to as physisorption, which primarily includes the vdW and the hydrogen bonds. By contrast, the chemisorption primarily includes the covalent and the complex bonds. Even if the observed systems seem to be complex, one may divide them into subsystems where each single interaction mechanism may be considered in a simplified way. The first case is - for example - an adsorbing molecule on a conductive surface such as HOPG or graphene. Like in the model of the vdW interaction as discussed above, the molecule comes closer to the surface and, depending on the dipole character

of the molecule, a corresponding interaction mechanism is engendered (compare equations 2.1). Here, mirror charges are now induced in the conductive surface by the molecule. A peculiarity of the vdW interaction is that it is always attractive and never repulsive, whereby the induced dipoles always tend towards the maximum of the distance-dependent polarisation versus the own charge separation, called polarizability, i.e. the charge separation is also always limited. The limit is determined via the overlap of the electron clouds, whereby it comes to the Pauli exclusion principle, a very strong repulsive force (Lennard-Jones potential, frequently about r^{-12} dependent). The same observation may explain the inter-molecular interaction, whereby molecules interact with each other along the surface.

$$V_{LJ}^{(n,m)} = \frac{C_n}{r^n} - \frac{C_m}{r^m} = 4\epsilon \left[\left(\frac{\sigma}{r}\right)^n - \left(\frac{\sigma}{r}\right)^m \right] \qquad [2.2a]$$

$$V_{LJ}^{(12,6)} = \frac{A}{r^{12}} - \frac{B}{r^6} = 4\epsilon \left[\left(\frac{\sigma}{r}\right)^{12} - \left(\frac{\sigma}{r}\right)^6 \right] \qquad [2.2b]$$

The equation describes the Mie potential (Lennard-Jones-(n,m) potential) where $C_{n,m}$ are the substance-dependent constants, ϵ is the energy at the deepest point of the potential, σ is the distance where the potential is zero, r is the distance and n and m are exponents which - in the best known case of the Lennard-Jones-(12,6) potential - are 12 and 6, respectively.

Another approach is necessary for the complete description and thus for the overall understanding of the interaction mechanisms, using the thermodynamic potentials.

$$\Delta G = \Delta H - T\Delta S + \mu\Delta N \qquad [2.3]$$

Here, ΔG is the change of the Gibbs energy and the binding energy with ΔH as the above-described interaction potential energy - called entropy - T is the total temperature, ΔS is the change of the entropy, μ the chemical potential and ΔN the change of the adsorbed molecules. The observed system of adsorbing molecules tends towards an equilibrium where ΔG becomes zero. In case $\Delta G < 0$, the system tends towards more adsorbed molecules (spontaneous reaction) and in the opposite case of $\Delta G > 0$ molecules desorb from the surface. For example, in the case of the solid-liquid interface, an equilibrium will be set where there will be a defined concentration between adsorbed (also solvent molecules) and dissolved molecules. The new additional term is the entropy S, which is independent of the interaction potentials but depends exclusively on the symmetry character of the system (mixing entropy).

2.3 Scanning Probe Microscopy (SPM)

Scanning probe microscopy (SPM) provides a powerful tool for measuring specimen surfaces. Here, “specimen” refers to the part of physical properties of the substrate that act upon the probe through the interaction mechanism(s) (several in most cases). Two of the relevant methods in this work are scanning force microscopy (SFM) and scanning tunnelling microscopy (STM). The former - also called atomic force microscopy (AFM) - relates to the measurement of the topographic surface properties, which is usually based upon the Lennard-Jones potential and thus the implied van-der-Waals (vdW) potential and the electrostatic force interaction. There are several kinds of SFM - for example, scanning force microscopy (SFM) and scanning tunnelling microscopy (STM) - with their manufacturer-related specifications. The latter is sensitive to the electronic states on a surface, which represent the density of states of the substrate, i.e. how these states reveal themselves on the surface at last. The following two sections will cover the measurement methods STM and SFM, although only the contact mode and the tapping mode will be applied.

2.3.1 Scanning Force Microscopy (SFM)

SFM is one of the most versatile measurement instruments. The number of operating modes is not only distinguished by the interaction mechanisms but also by the particular manner of carrying out the measurements. The operating modes include contact mode (CM-SFM), non-contact (NC-SFM), intermittent contact (IC-SFM), amplitude modulation (AM-SFM), frequency modulation (FM-SFM), conductive (C-SFM), magnetic (MFM), Kelvin probe (KPM), chemical force microscopy (CFM), scanning electrochemical microscopy (SECM-SFM), force spectroscopy, tip-enhanced Raman spectroscopy (TERS) and scanning near field optical microscopy (SFM-SNOM), to name just a few. The interaction mechanisms and their related operating modes are so versatile that the measurements and their related analysis and the interpretation of the results are very complex. In the following, only the basics are considered, concerning the non-contact mode, the contact mode and the intermittent contact mode.

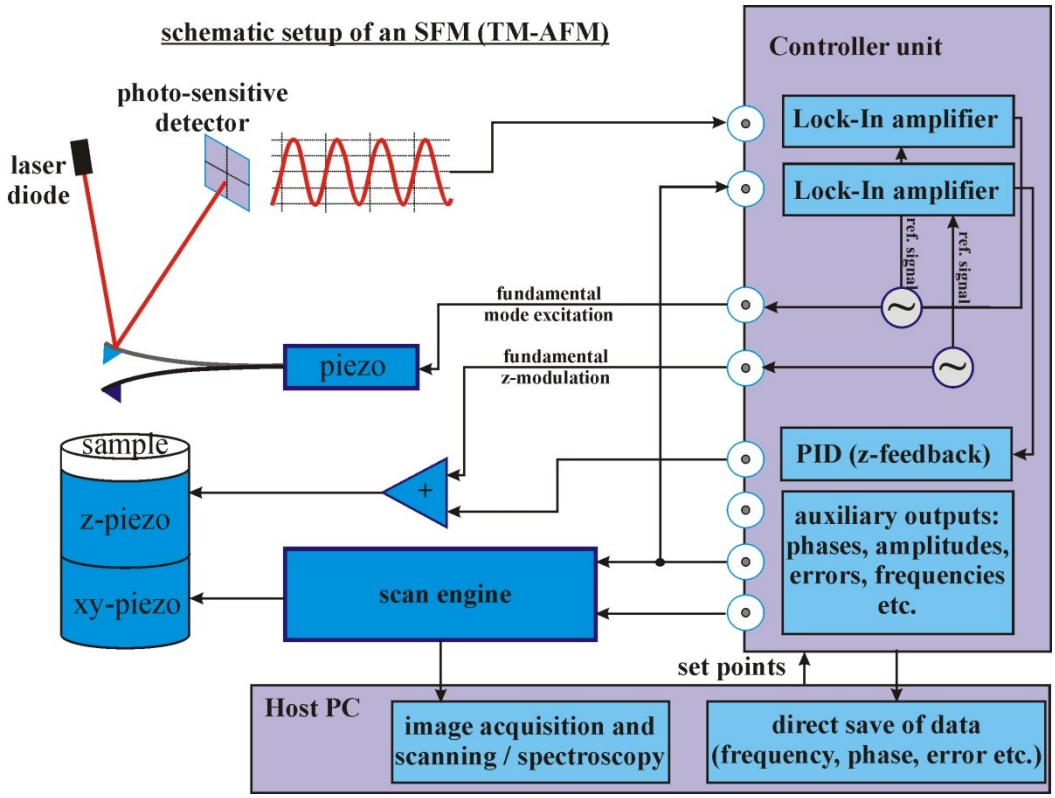

Figure 2.4 A conceivable schematic construction of an SFM [1].

All operating modes without the spectroscopy have in common that a sharp probe on a cantilever scans line-wise over the surface to obtain its spatially resolved properties. The spectroscopy measures force-distance dependencies, e.g. the strength of chemical bonds. A schematic representation of an SFM setup is shown in Fig. 2.4. The cantilever bar is optically detected by a laser, whose reflection is recorded via a four-segment field detector. The detector converts the optical signals to electrical signals, whereby the relative orientation may be detected. The relative orientation of the probe is affected by the strength of the force via the interaction mechanisms. The relative position of the surface to the probe is accomplished by piezo(s) for fine adjustment (angstrom - micrometre) and step motor(s) for larger movements (micrometre - millimetre). The electrical signals are now compared with the set points given by the user, whereby the measuring procedure is continuously adjusted to the conditions. Here, the probe now plays a central role. It comprises a sharp tip at one end that has a measurement specific apex shape, while the other end mostly consists of a large bulk for better handling and mounting. In most cases, the probes are

[1] scheme based on Zurich Instruments

made of doped silicon. The principle of the probe is essentially based upon beam bending. The spring constant and the torsion property depend on the shape of the beam. The simplest interaction mechanism that can always be found is the Lennard-Jones-(12,6) potential

Here, A and B are substance-dependent constants and r is the distance between the two partners. The second term with the r^6 dependence is called vdW potential. This interaction is not an intrinsic property of a substance, but rather only revealed in the presence of another interacting partner. A simple example is the nitrogen N_2 molecule. The time-averaged dipole moment of an isolated nitrogen atom vanishes. Only when two nitrogen atoms become closer, dipole moments induce each other and thus reveal an attractive force. The characteristics of the Lennard-Jones potential are shown in Fig. 2.5.

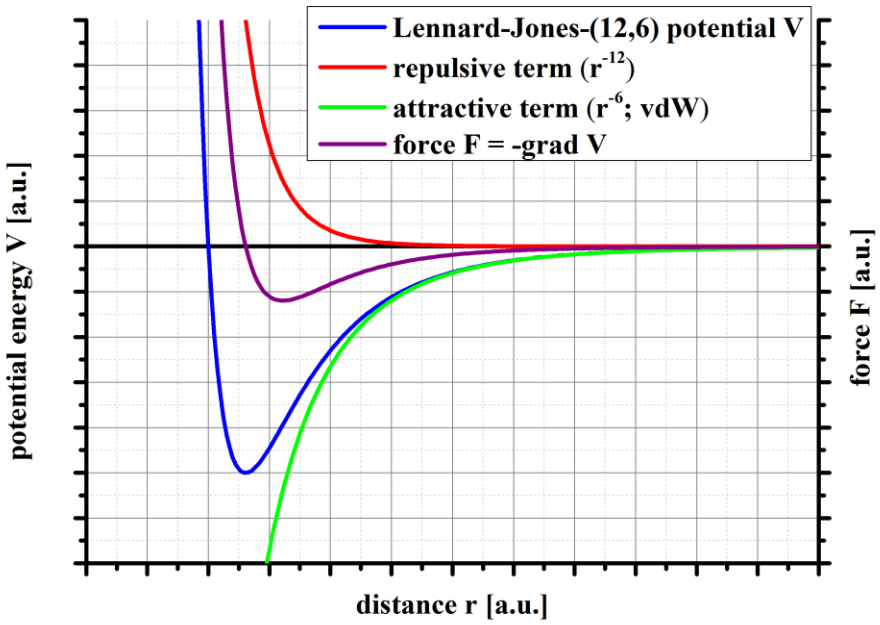

Figure 2.5 CThe Lennard-Jones-(12,6) potential, its attractive (r^{-6}) and repulsive (r^{-12}) part and the corresponding force F as a gradient of the potential energy V.

The L.-J. potential (blue) may be distinguished in a repulsive term (red), whose slope is always negative, as well as an attractive term (green), whose slope is always positive. The force F (violet) is given by the negative gradient of the potential energy V. When the sign of the force is negative, the force of both is oriented to each other and the force is oriented oppositely with a positive sign. In the point of the minimum of the potential energy, the force is zero. All operation modes where the tip is closer to the surface may be considered as the contact mode and in the opposite case the

non-contact mode. While the tip is retracted from the surface, the laser reflection on the detector constitutes the baseline or the start position. At the moment of surface-tip interaction, the cantilever bends, whereby the position of the laser reflection on the detector is moved. When the required point of bending is achieved - i.e. the required interaction force - the work state is achieved. During the scan, the distance is readjusted incessantly by the controller, which in turn incessantly compares the measured parameters with set points. This operation mode may be accomplished in the contact as well as the non-contact mode. With the illustration of Fig. 2.6, a possible problem of interpretation can be seen. When the surface is homogeneous in its physical properties, there is only one interaction potential and the measured topography of the surface mostly corresponds to the real surface topography, taking the resolution limit and other sources of errors into account. In Fig. 2.6, two potential energies V(I) and V(II) and their forces F(I) and F(II) imply that the surface comprises two different physical surface properties. The instrument typically measures the surface per cycle with only one parameter set, i.e. the differing surface properties are measured at the same interacting force between the tip and corresponding surface. During the measurement, the tip is always in the corresponding distance to the force, which was given by points set by the user, i.e. the same force F(I) = F(II) is acting, independent of the corresponding surface properties. The curves for surface I and II show that different interacting distances r(I) and r(II) are possible despiteF(I) = F(II). In addition to the "real" topographical signals, the potential and force-dependent signals are added.

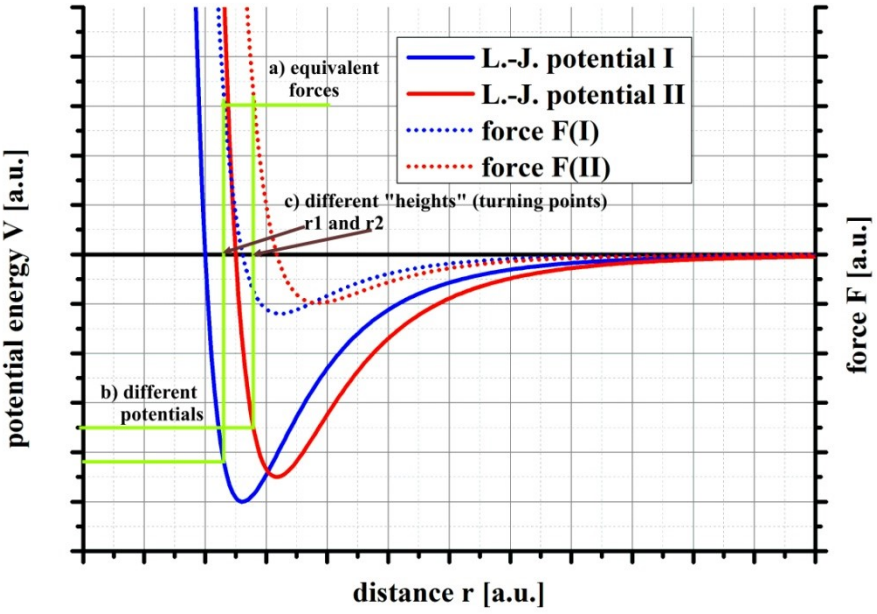

Figure 2.6 A comparison of Lennard-Jones-(12,6) potentials and their corresponding forces, whereby different heights can be measured despite the real height being the same. When the SFM measures with the same set point - i.e. the same force (**a**) a surface with two different characteristics (potential I and II) - the cantilever has several turning points (**c**), i.e. the SFM measures a height difference ($\Delta r = r_2 - r_1$) where actually there is none.

The intermittent mode provides a good solution here. This mode is also called the AC mode (alternating current, AC-AFM) or tapping mode (TM-AFM). All have in common that the tip is oscillating permanently vertical to the surface in a defined distance range. i.e. in most cases between the contact with surface and a certain distance where its interacting force approaches zero. In the following, only the mode where the beam vibrates close to its resonant frequency is discussed, though others exist, e.g. quantitative imaging (QI mode) of JPK or the PeakForce mode of Bruker. Each beam may be construed as a unilaterally mounted, oscillating beam with a resonant frequency, which depends on its material-specific and geometric properties as well as ambient conditions. For a freely vibrating and undamped beam in vacuum or air, the differential equation is applied (Meirovitch, 1967) [40],

$$EI\frac{\partial^4 u}{\partial x^4} + \rho_B A\frac{\partial^2 u}{\partial t^2} = F(x,t). \qquad [2.2]$$

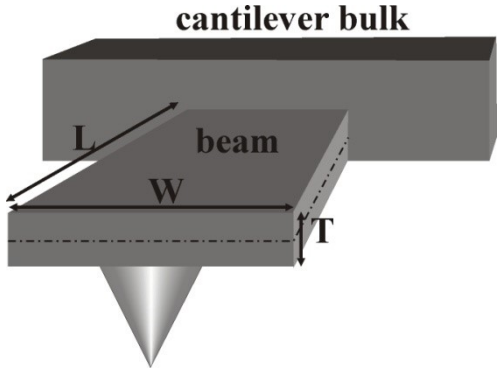

Figure 2.7 Simplified sketch of the geometry of a cantilever.

Here, E is the modulus of rigidity of the beam material if it remains constant during the bending along x, I is the moment of inertia of the beam cross-section if its shape remains during the bend, F(x,t) is the force applied on the cantilever per unit length of the cantilever at any time, $m = \rho_B A$ is the mass per unit length, where ρ_B is the material density of beam and x is the distance measured from the fixed end. The solution for the resonant frequency and its modes n can be written as

$$f_n^{vac} = \frac{\omega_n^{vac}}{2\pi} = \frac{\beta_n^2}{2\pi L^2}\sqrt{\frac{EI}{\rho_B A}} \qquad \text{with} \quad \beta_n L = \frac{(2n-1)\pi}{2} \qquad [2.3]$$

As can be seen, the modes of the resonant frequencies f_n are not multiples of L like in the case of a unmounted beam. However, in most cases, one has the case of a damped beam. The damping is engendered by the transfer of the energy from the beam to the surface, the dissipation - e.g. via a soft surface - of a water film on the surface (in air) or a measurement in a fluid cell [41–47]. The simplest case of a damped beam is given by the equation

$$f_d = \frac{\omega_d}{2\pi} = \frac{\omega_0}{2\pi}\sqrt{1-\zeta^2} \qquad [2.4]$$

When the energy transfer is from the beam to the surface, the damping ratio is $\zeta > 0$ and in the opposite case $\zeta < 0$. In both cases, there is a frequency shift to lower frequencies. For a better understanding of the influenc of damping, a corresponding equation of an embedded cantilever in a medium for the flexural mode [46] reads as

$$f_n^M = \frac{\omega_n^{vac}}{2\pi}\left(1+\frac{\pi}{4}\frac{W}{T}\frac{\rho_M}{\rho_B}\Gamma_f(n)\right)^{-\frac{1}{2}} \qquad [2.5]$$

with $\Gamma_f(n) = \frac{1+0.74\kappa+0.15\kappa^2}{1+0.74+0.35\kappa^2+0.06\kappa^3}$ and $\kappa = C_n\frac{W}{L} = \beta_n W = \frac{(2n-1)\pi}{2}\frac{W}{L}$.

Here, ρ_B and ρ_M are the density of the beam and the medium, $\Gamma_f(n)$ is the hydrodynamic function and $C_n = \beta_n L$ are the eigenvalues as solution of $1+\cos(C_n)\cosh(C_n)=0$. Therefore, one can immediately observe that, since all values have a positive sign, the shift of the frequency is always towards smaller values $f_M / f_{vac} < 1$ by the damping, i.e. there is always a dissipation from the beam towards to the surface. Only if the tip interacts with the surface rather strongly,, deformations take place and a positive frequency shift $f_M / f_{vac} > 1$ results. Interestingly, the measured interaction force is approximately given by

$$F_{int} = -\frac{A_H R}{6z^2} + \frac{12\epsilon}{r_0}\left[\left(\frac{r_0}{z}\right)^{13} - \left(\frac{r_0}{z}\right)^{7}\right]. \qquad [2.6]$$

Here, A_H is the Hamaker constant, R the tip radius and r_0 the equilibrium distance. The Hamaker constant is a substance-specific value, which is dependent on the number of interacting atoms the particle-particle interaction parameter, based upon the parameter $-B/r^6$ (vdW part) in Eq. (2.1). This fact was impressively demonstrated experimentally by Hölscher et al. (2000) [45]. The case of moderate forces can be written for the dissipative power

$$P_{diss} = P_0 + P_{int} = F_0\dot{z}_o(t) = k\left[z_{tip}(t) - z_0(t)\right]\dot{z}_0(t) \qquad [2.7]$$

Here, P_{diss} is the dissipated power, k the spring constant of the cantilever, P_0 the stimulus power - i.e. the intrinsic dissipated power of the cantilever, $z_0(t)$ the temporal stimulus amplitude, F_0 the stimulus force, $z_{tip}(t)$ the temporal amplitude of the tip and P_{int} the power of the interaction mechanism between tip and surface. With the considerations about the frequency, it still does not have an additional parameter whereby two different surface properties may be distinguished. However, there is a corresponding phase for each oscillating beam and its resonant frequencies. With the phase, the temporal correlation of the amplitude of the tip to its stimulus amplitude is related. In Eq. (2.7), the difference $[z_{tip}(t)-z_0(t)]$ is the implicit form of the phase, whereby the equation can be written as $\cos(\omega t+\Delta\varphi)$ or $\sin(\omega t+\Delta\varphi)$ with a phase shift $\Delta\varphi$. Experience has shown that it is not practical to calculate the phase, which may considerably change from cantilever to cantilever, including within a batch. An important property of the vibrating beam is the large phase change close to a resonance frequency of several ten degrees. The sketch in Fig. 2.8 illustrates the discussed subjects.

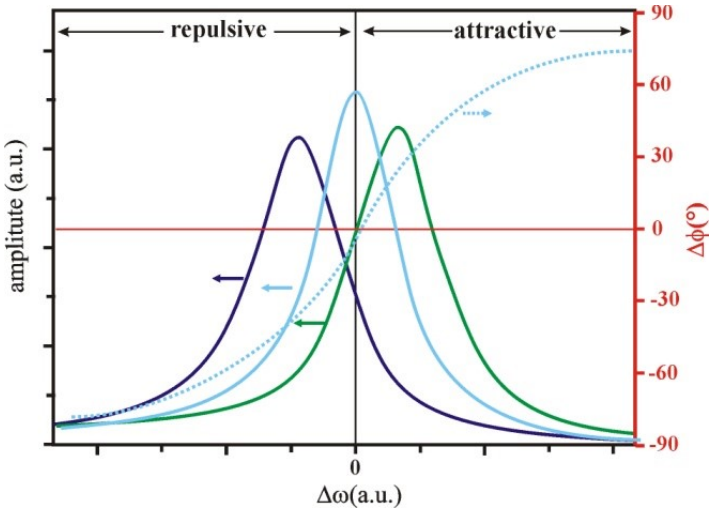

Figure 2.8 Sketch of typical behaviour of frequency and phase of a cantilever beam in tapping mode (or AC mode). The arrows indicate the affiliation to the unit (left the amplitude or right the phase shift). The middle light blue curve represents the free resonant vibration of a cantilever beam. The left dark blue and the right green curve are the damped resonant vibrations if the cantilever beam is close and in interaction with a surface whereby the amplitude is decreased. Corresponding to the energy transfer from the surface to the beam or vice versa, there is a frequency shift to shorter or longer frequencies, respectively. The behaviour of phase can be understood in analogy. The phase is very different from cantilever to cantilever and unsuitable as

an absolute value, although the relative values are useful as rough indicators to distinguish between different surface characteristics.

Figure 2.8 shows the range concerning the resonant frequency for the undamped (only intrinsically damped) and the damped cases. Typically, amplitude A has the highest value and the quality value Q the smallest. The quality value Q is the ratio of amplitude z_{tip} to its full width at half maximum (FWHM). In the case of damped oscillation, the amplitude becomes smaller, the Q value greater and there is a frequency shift towards smaller values. In Fig. 2.8b, the typical relation between the frequency and phase is shown. It should be noted that the characteristic phase course is random, i.e. the phase jump might also be inverse. In case the interaction between the surface and the beam is damped, there is - beside the frequency shift - also a more or less strong phase shift dependent on the amplitude [44]. This combination of amplitude and phase shift makes it possible to distinguish the different surface properties, whereby the measurement and analysis of the true topography is only possible via the measurement of the amplitude changes as well as the phase changes.

2.3.2. Scanning Tunnelling Microscopy (STM)

The scanning tunnelling microscopy (STM) is a powerful tool to study surfaces of conducting samples and - under certain conditions - electrically insulated thin films on top of a conductive sample [50, 51]. The strength of STM and its further developments is based on the correlation between the tip and the local surface that enables high spatial (atomic) and energy resolution by which structural, electronic and magnetic properties can be detected. In the following, the techniques and the theory of tunnelling effect are elucidated, i.e. the following part summarizes the phenomenological, physical aspects of the tunnel process with the theoretical background and thus will provide an explanation for the advantages of the STM.

The basic component of the STM consists of a probe that scans line by line over the surface, whereby it has preferably smallest lateral dimension and a distance-dependent interaction mechanism to the surface. If the strength of the interaction mechanism is kept constant, the topography is primarily measured, whereas when the distance is kept constant the strength of interaction mechanisms is primarily measured (compare Figs. 2.9 a and b). In both cases, one has to assume a homogeneous distribution of physical properties of the substrate, otherwise the analysis will be very complex.

The interaction mechanisms are based upon the probe, the electrical properties of the surface, and the ambient conditions in which it is measured. Accordingly, it needs a unit of measurement for the incoming electrical signals, which is also used as a control unit for the steering of the probe, as well as a unit that visualizes the signals. The probe ideally consists of one or a few atoms. The distance from the probe to the surface - i.e. the tunnelling distance - is typically in the range from few angstrom to about 1 nm. The incoming signal is obviously parameterized in voltage, current, scan speed and in its time-resolved parameters. The latter parameters are generated by the temporal comparison of measured voltage and current with the set points given by the user. Here, it is important to distinguish between three control loops, which can be differently found in various applications, depending on the manufacturer. The three control loops are the proportional, the integral and the differential controller. Note that the complete procedure of the control of the STM is referred to as the feedback loop. All parameters together not only control the measurement but also characterise the measurement in the two types above, called constant height and constant interaction mechanism strength (mostly called constant current mode).

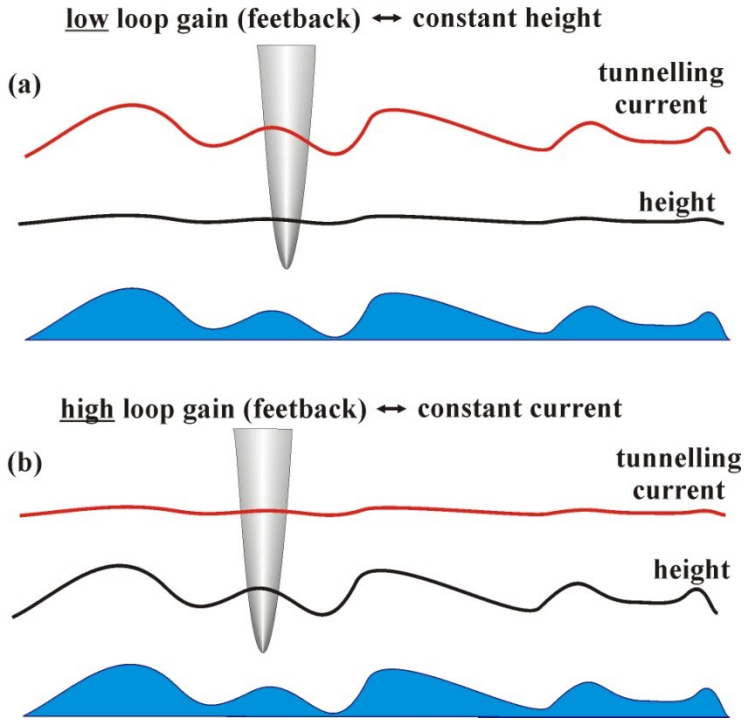

Figure 2.9 Distinction between the constant height (**a**) and constant current (**b**) mode of an STM. Blue is the surface where the STM tip (grey) moves along in the tunnelling distance. The tunnelling distance corresponds with the height but is not equal to it. The measured current is not the same as the current of tunnelling junction, since the former one results from the entire electrical "circuit

components", where the tunnelling current is only a part. During one measurement, the contribution of the components is mostly constant and only the tunnelling current and the height of the surface is variable. The comparison between single measurements is more problematic since the components such as tip, contact resistances, etc. may be different.

The constant height mode keeps the z-component of the STM tip constant and in most cases the current is measured at constant voltage. In this situation, the tilt of the surface has to be exactly equal to the tilt of the virtual scan surface, since the tunnelling distance is in the range of a few angstrom. Since the measured parameters are only the current and voltage, it is impossible to measure the tunnelling distance directly. The implementation of this mode is accomplished by the suitable choice of the time parameters. These parameters may be interpreted as an effectively more or less strong delay of the response to changes during the measurement, whereby the tip can follow the surface shape only in a time-lagged manner. When suitable parameters are chosen - i.e. the response is very strongly time-lagged - the constant height mode is apparently generated. The second mode is the constant current mode, in which efforts are made to keep the strength of the interaction mechanism constant. Since the tip remains unchanged during the scan, the local properties of the surface and substrate can only change themselves, e.g. the density of state or the height. It is not unusual that the substrate comprises different components, e.g. some molecules adsorbed on HOPG. However, it is assumed that the measured interaction mechanism may be a complex superimposition of single phenomena, i.e. a superposition where the single components do not mutually affect themselves, or an interaction mechanism as a new property of the composition, i.e. the property of the composition is different to its separated single components. From these considerations, it has to be concluded that a high degree of presupposition and previous knowledge have to exist about the substrate. The interaction principle of the essential components of the STM is shown in Fig. 3.11. The piezo includes the STM tip, whereby the relative position of the tip to the surface can be modified. The movement is along the three spatial coordinates and implemented by the voltage-dependent shape changes of the piezo: Depending on the voltage, the four piezos work against each other or thogether for the x-y direction or the z-direction, respectively. Thus, there are connections for the controlling of the piezos and a connection for the measured signal of the STM tip and its tunnelling current. The measured signal is analysed by the detector, where a preamplifier and an AD converter are also mostly involved. On the one hand, the processed signal is visualized via the PC, while on the other hand the processed signal also comes to the controller unit. The user gives the set points from the PC to the controller. There, the set points are compared with the measured parameters whereby the corresponding new control

signals are generated. The limiting units are mostly the preamplifier (low pass), the PC (clocking and bit number), the controller (clocking) and the piezo (piezo effect).

Essentially, the STM is based upon the interplay of kinetic and potential energy ($E_{kin} > E_{pot}$) of electrons in substances whereby an electron can also cross a barrier between two substances where the potential energy is higher than its kinetic part ($E_{kin} < E_{pot,barrier}$, see Fig. 2.11). The transmission probability T can be calculated by quantum mechanics as

$$T = \frac{4E(V_0-E)}{4E(V_0-E)+V_0^2\sinh^2\frac{\sqrt{2m(V_0-E)}d}{\hbar}}. \qquad [2.1]$$

Here, E is the kinetic part of the electron with its mass m, V_0 the potential energy in the barrier and d is the distance between the two substances, namely the width of the barrier. This is the simplest "classical" description of the tunnelling effect as it is derived in the textbooks. Some interesting, advanced descriptions to the tunnelling effect were published by Nicol et al. [49] (1960), Giaever [50] (1960) and Bardeen [51] (1961), i.e. even before the development of the STM.

$$I = \frac{2\pi e}{\hbar}\sum_{\mu,\nu}\{f(E_\mu)[1-f(E_\nu+eU)]-f(E_\nu+eU)[1-f(E_\mu)]\}|M_{\mu,\nu}|^2\delta(E_\mu-E_\nu) \qquad [2.2]$$

with $$M_{\mu,\nu} = \frac{-\hbar^2}{2m}\int dS\cdot\left(\Psi_\mu^*\nabla\Psi_\nu-\Psi_\nu\nabla\Psi_\mu^*\right)$$

Equation (2.2) - which is a purely formal notation of Fermi's golden rule - describes the tunnelling junction I of electrons between the two substances with statistics μ and ν, respectively. Here, f is the Fermi-Dirac distribution, U the applied gap voltage, E the energies, Ψ the wave functions of the electronic states and $M_{\mu,\nu}$ the matrix elements. Since the wave functions may also include the spin, one can recognize that spin dependence measurements are possible with a suitable setup. The specific geometry of a STM was first described by Tersoff and Hamann [52, 53] (1983 and 1985, valid one to three years after the development of the STM). The model makes two essential presumptions: on the one hand it is assumed that the STM tip has a spherical geometry with radius R in the essential surface of tunnelling junction; while on the other hand, it is assumed that the tip and the sample can be described by the Bloch function, i.e. both have a periodic lattice structure.

$$\Psi_\nu = \Omega_s^{-\frac{1}{2}}\sum_G\left(a_G\cdot e^{-\sqrt{k^2+|\vec{k}_\parallel+\vec{G}|^2}z}\cdot e^{i(\vec{k}_\parallel+\vec{G})\vec{x}}\right) \qquad [2.3a]$$

with $$k = \frac{2\pi}{\lambda} = \frac{p}{\hbar} = \frac{\sqrt{2m\Phi}}{\hbar}$$

with Ω_s as the volume of the sample, k the wave number of the electronic state with a work function Φ.

$$\Psi_\mu = \Omega_t^{-\frac{1}{2}} c_t k R e^{kR} \frac{e^{-k|\vec{r}-\vec{r_0}|}}{k|\vec{r}-\vec{r_0}|} \qquad [2.3b]$$

with Ω_t as the tip volume and R the radius of the tip apex. The wave function of the tip implies a s-wave, since the other terms can be disregarded. Thus, the matrix element $M_{\mu,\nu}$ can be written as

$$M_{\mu,\nu} = \frac{\hbar^2}{2m} 4\pi k^{-1} \Omega_t^{-\frac{1}{2}} k R e^{kR} \Psi_\nu(\vec{r}_0) \qquad [2.4]$$

With the assumption of a Taylor series of the Fermi distribution

$$f(E_\mu + eU) = f(E_\mu) + eU \cdot f'(E_\mu)$$

the tunnelling current can be calculated as

$$I = 32\pi^3 \hbar^{-1} e^2 U \Phi^2 \rho_t(E_F) R^2 k^{-4} e^{2kR} \sum_\nu |\Psi_\nu(\vec{r}_0)|^2 \delta(E_\nu - E_F)$$

$$I \propto U \cdot \rho_t(E_F) \cdot \rho_s(E_F, \vec{r}_0) \cdot e^{-kd} \qquad [2.5]$$

Here, it is also assumed that the Fermi distribution f is a Heaviside step function, i.e. at very low temperature, whereby the first derivative becomes the δ distribution. Equation (2.5) thus tells us that the tunnelling current depends primarily linear on the applied voltage U and exponentially on the distance between tip and surface at the place of the tip, albeit under the following conditions:

- the tip has a uniform density of state (Bloch function);
- the tip wave functions are approximately s-waves (R much larger than distance d);
- very low temperature (Fermi distribution as Heaviside step function);
- the applied gap voltage is very small (first derivative of Heaviside function); and
- no scattering inside the barrier (missing scattering term).

For any applied voltage U, the tunnelling junction can be analytically calculated using the WKB approximation (almost simultaneous publications in 1926 of G. Wentzel [54], H.A. Kramers [55] and L. Brillouin). For the tunnelling current, the following integral has to be calculated

$$I \propto \int_0^{eU} dE \cdot \rho_s(\vec{r}_0, E) \rho_t(\vec{r}_0, E - eU) exp\left(-\frac{2\sqrt{2m}}{\hbar} d \sqrt{\frac{\Phi_s + \Phi_t}{2} + \frac{eU}{2} - E} \right) \qquad [2.6]$$

Besides the linear dependence in Eq. (2.5) at low applied voltages, the exponential dependence is added at high applied voltages. Here, $\Phi_{s,t}$ are the work functions of the sample and the tip, respectively. These relations are shown in Fig. 2.11.

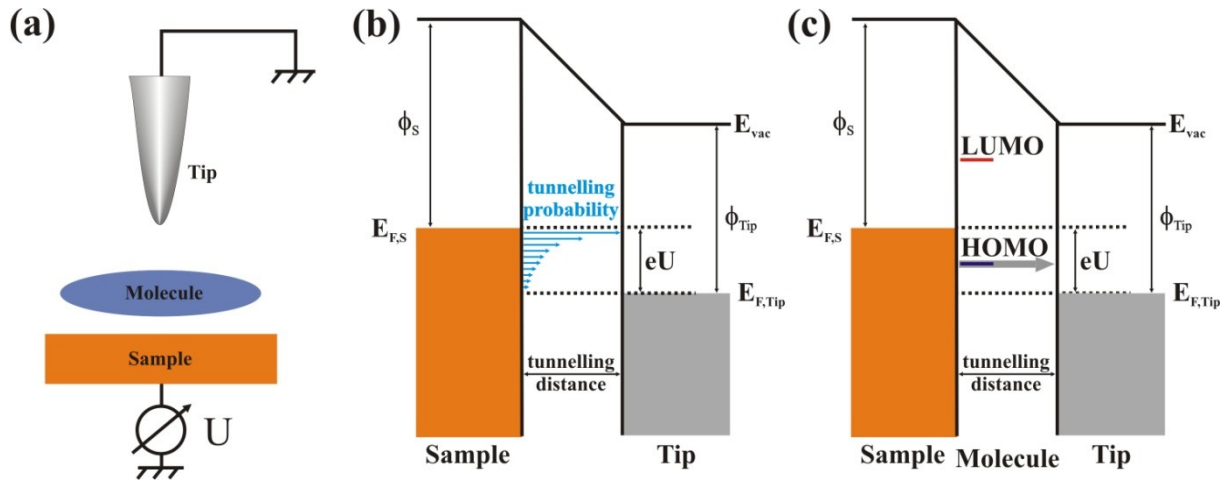

Figure 2.11 Principle of the tunnelling junction without (**b**) and an additional resonant tunnelling effect through a intervening molecule (**c**). In **a**), a simplified electrical circuit of a STM is shown with the surface (orange), molecule (blue) and the tip (grey), where the tip and the surface are electrically connected with an adjustable power supply. In **b**) (at first without molecules for a better understanding), the dependence of the tunnelling junction and its corresponding current from the voltage is shown,compare Eq. (2.6). **c)** In addition to the tunnelling junction, there is a resonant tunnelling junction through the energy level of the molecule, which results in an increased measuring signal where the contrast may become much more pronounced between the surface and the molecules. However, since the set points - such as the current and the voltage - are constant, the tunnelling distance - which corresponds with the height - is also increased, whereby one has to recognize that the measured heights may be very different from the real heights.

However, what is still missing is the temperature and the average of the barrier. The temperature smudges the Fermi-Dirac f(E,T) distribution around the Fermi energy, although since the temperature equivalent energy kT is much smaller (some 10 to 100 meV) than the Fermi energy (some eV), this effect is correspondingly low.

$$f(E,T)=\frac{1}{1+\exp\left(\frac{(E-E_F)}{kT}\right)} \qquad [2.7]$$

When the STM measurement is carried out on a solid-liquid interface - whereby the system changes from vacuum with simple conditions to a medium with very complex conditions - the

influence of the medium of the barrier to the measured current cannot be calculated analytically any longer., e.g. due to scattering. The influence is comparable with the dynamic electrochemistry (e.g. cyclic voltammetry), which is about the processes in current-carrying electrochemical systems. However, every solvent and the therein dissolved molecules constitute a current-carrying electrochemical system. In this context, the STM on a solid-liquid interface constitutes an electrochemical cell. Electrochemical cells can be essentially sub-divided into electrolysis cells and electrochemical elements. In galvanic elements, the electrode reactions are exergonic without additional electricity supply ($\Delta G<0$). In electrolytic cells, substances are decomposed electrochemically by supplying power ($\Delta G>0$). The central cause for the reactions is the difference in the respective chemical potential of the electrodes and the molecules, reflecting one reason why the electrodes - e.g. graphite, graphene or the Pl / Ir tip - have to be chemically inert. In addition, one endeavours to choose a non-electrolytically acting solvent. However, this only succeeds conditionally, since only in certain solvents the properties of the molecule are explicitly known (solubility, adsorption, solvatochromism, switching capability, etc.). Even if the tunnelling distance is smaller than 1 nm but with an applied gap voltage of 1V, there is a field strength of about 10^9 V/m. Therefore, there may be voltage-dependent reactions, which may affect the STM measurements, whereby the solution of solvent and molecules affect each other in the presence of electrodes and the variable applied voltage [54–59].

3. Materials and Experimental Setup

3.1 Introduction

This chapter is sub-divided into two parts: first, we give an introduction to the used materials and secondly, the experimental setup is described, i.e. the STM which is expanded via an optical microscope and the SFM (Scanning Force Microscopy).

3.2 Materials

The used materials in this section are HOPG (Highly-Oriented Pyrolytic Graphite), single- and multi-layer graphene and mica as substrate, elemental water (H_2O) - where also the elementary compounds OH^- and H_3O^+ are considered - and finally the porphyrin-spiropyran dyad with its compounds zinc-tetraphenylporphyrin (ZnTPP; 5,10,15,20-tetraphenyl-21H,23H-porphine zinc) and nitro-spiropyran (1',3'-dihydro-1',3',3'-trimethyl-6-nitrospiro[2H-1-benzopyran-2,2'-(2H)-indole]).

3.2.1 HOPG and Graphene

Highly oriented pyrolytic graphite - also known as highly ordered pyrolytic graphite (HOPG) - is a high purity and highly oriented graphite crystal produced via a pyrolysis process and growth from a gas phase. The basic structure is determined by a hexagonal, covalent bound of carbon atoms - also called "honeycomb" or "chicken wire" - along a basal plane (compare Fig. 3.1). The crystal planes are oriented parallel to each other in the ideal case with a shift of a half unit cell in a unit vector direction, which results in a ABAB or ABC structure. Precisely, the HOPG gets its electrical and mechanical properties from the sp2 hybridisation along one basal plane (compare Fig. 3.2) [60–63]. However, these properties differ along the perpendicular axis, where the planes are very weakly bonded to each other via vdW interaction. Rather, the π-electron "cloud" [64], which lies between the basal planes and where the electrons are delocalised along the planes to constitute a collective wave function, leads to a metallic bond character.. The binding energy between carbon atoms with covalent sp^2 bondsis about 4.3eV[2]. By contrast, the binding energy of the planes to each other is only about 70 meV. If compared to the thermal energy at room temperature, $kT \approx 25$ meV, the planes may be easily separated mechanically from each other in a stochastic manner. In reality however, the ideal case of one single, infinitely extended plane does not apply in reality. Accordingly, the epitaxially grown planes have different size, are inclined to

[2] Please note that the basal plane effectively comprises each 1.5 double bond (~4.3eV) in temporal average and not each double bond (C=C) with an energy of ~6.2eV (C-C single bonding energy ~3.6eV).

each other, contain point, line, area and room defects (0D, 1D, 2D and 3D defects). The planes of each domain may be also turned, i.e. misaligned to each other, i.e. they do not follow the ABAB or ABC layering (Moiré pattern in a STM measurement [65]). The Moiré pattern of a graphene layer on top of a HOPG provides an indication of the surface sensitivity of the STM measurements and the underlying layers of graphene (multilayer graphene). One parameter for the classification and evaluation is the mosaic spread angle, which is 0.4° ± 0.1° for an ZYA crystal and 0.8° ± 0.2° in case of ZYB (Advanced Ceramics), where the individual domains of a crystal are inclined to each other with an average angle of 0.4° and 0.8° for ZYA and ZYB, respectively. However, the size of the domains and therefore the size of the graphene layers after have via exfoliation from a HOPG (see chapter 4.2.1.1). An important property of HOPG is its surface lattice structure, which makes it so useful. The surface structure is similar to a variety of organic molecules such as HBC derivatives (hexabenzocoronene), dehydrobenzo [12] annulene derivatives (DBA), porphyrinderivatives, etc. They adsorb particularly well and thus offer a wide field of manipulable adsorption characteristics [66, 67]. This characteristic can be well observed at the system with unsubstituted HBC (uHBC) on HOPG. Via STM, the molecule as well as the HOPG structure can be simultaneously observed [68]. Many experiments are carried out in solution or atmosphere, rather than in an ideal system like vacuum. The surface must not react chemically with these surrounding materials. HOPG is a such material which is inert to the most solvents and the constituents of air. In an obvious manner, the close relationship of graphene to HOPG - as a monolayer - extends the experimental opportunities.

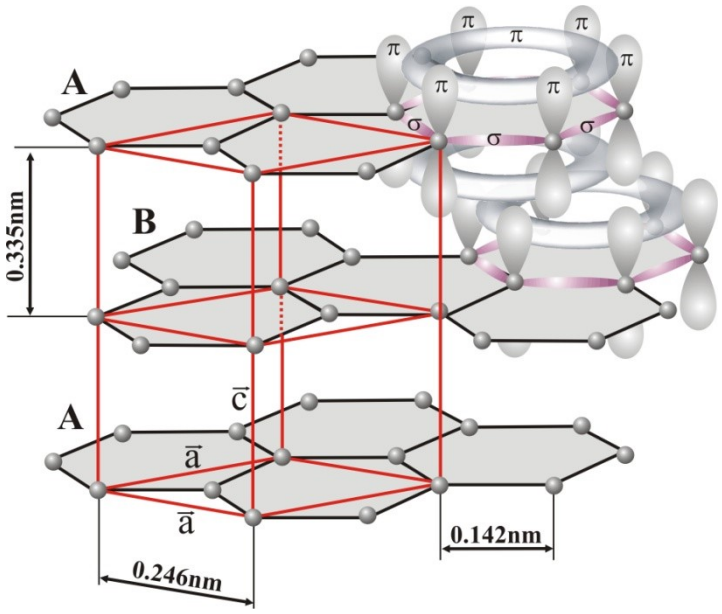

Figure 3.1 The lattice structure of a HOPG (hcp: hexagonal close-packed), which belongs to the D_{6h} (dihexagonal - dipyramidal) symmetry point group. The red lines indicate the unit cell of the ABAB package. ABAB means that the planes are shifted to each other by a half unit cell in the same direction. The σ (violet) and π (grey) orbitals indicate the principle of the van-der-Waals bond. The π electron orbitals - a collective effect - are freely movable along the plane axes.

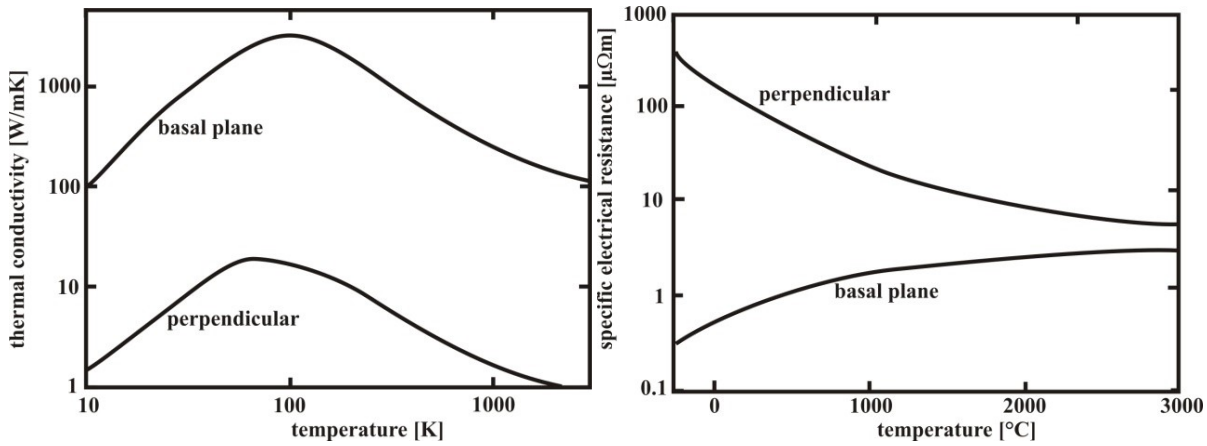

Figure 3.2 Both sketches indicate different properties of HOPG between the c-axis (perpendicular) and the pane-axes (basal).

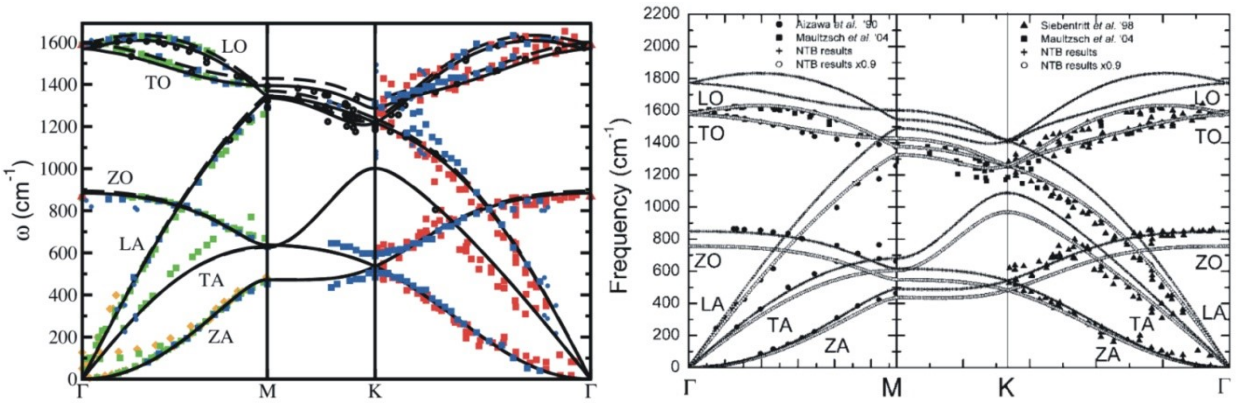

Figure 3.3 Phonon dispersion of HOPG (left) and (right) graphene. Experimental data are represented by dots [70, 71].

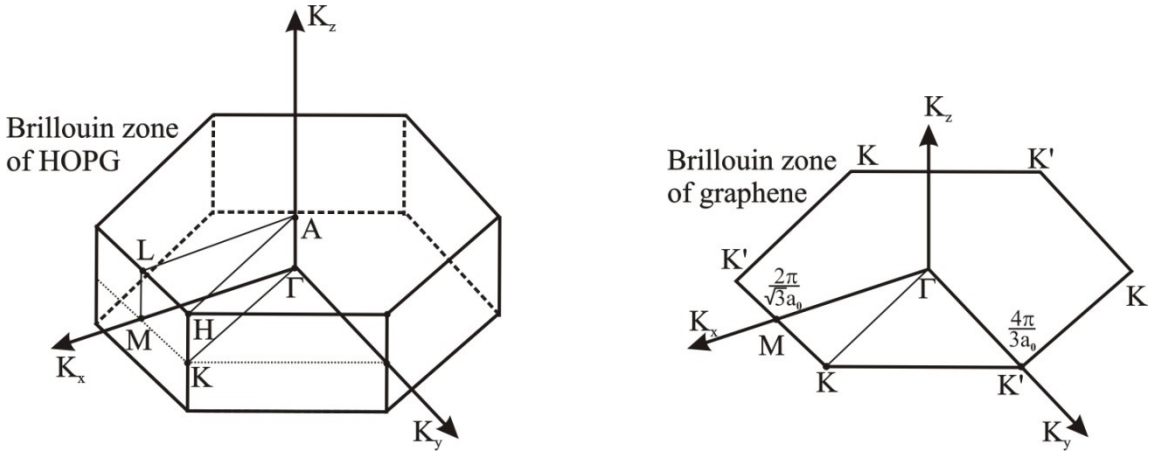

Figure 3.4 Brillouin zones of HOPG (left) and of graphene (right).

Graphene is practically considered as one basal plane of HOPG and is obtained by exfoliation (mechanical cleavage). Further forms of "graphene" determined by its production methods are epitaxial graphene (chemical vapour deposition, CVD) [72] and reduced graphene-oxide (GO, by chemical reduction of HOPG) [73], which should be called - if any - graphene-like rather than graphene, because the properties are only similar and not completely identical. Graphene has the same lattice structure as the sp^2 hybridisation of carbon atoms and - obviously - resembles many properties of HOPG [74–83]. In Fig. 3.3, a theoretical and experimental comparison of the dispersion relation between HOPG and graphene is shown. Beside the properties discussed so far, graphene also has high flexibility and stretchability of the atomically thin monolayer [81, 82]. In Fig. 3.4, the Brillouin zone and the band structure of HOPG and graphene are shown, respectively. The Brillouin zone of HOPG is a hexagonal prism with some of the most important points Γ ,K ,A and H [83]. Here, Γ is the centre of the Brillouin zone, where the wave number $k = 2\pi / \lambda$ is zero and thus the wavelength is infinitely extended, although this does not mean the frequency is also zero. The point K is the centre of an edge, which connects two rectangular faces. The point A is the centre of a hexagonal face and H is a corner. The Brillouin zone of graphene is a flat two-dimensional hexagonal lattice, where - in comparison to HOPG - the points Γ and A and the points K and H coincide, i.e. there are only the points Γ and K. Perhaps the most famous property of graphene can be found in the K and K' symmetry points, where the electrons are massless Dirac fermions due to the linear dispersion of cones around the K, K' points [84]. The same phenomenon is even observable at the HOPG, not in the K but rather in the H symmetry points [85]. For better understanding, one goes virtually from the Γ point over A to the H point and recognizes how the wave character changes itself. The collective electron wavelength is equal to the length of the unit vector **c** with the orientation along the c-axis, i.e. the amplitude has a phase shift of π (180°) from basal plane to the respective adjacent planes. The second component of H (vector component K) of the collective electron wave has a wave length of two times the unit vector **a** and is oriented along the zigzag direction (unit vector **a**), i.e. perpendicular to the armchair. The phenomenon of HOPG and the massless Dirac fermions is a collective effect of all electrons with the same energy level with and close to the Fermi energy, extending over the entire crystal. The difference between the K to the H point in the HOPG crystal is that the phase shift in K is zero in opposite to a phase shift of π in the symmetry point H. Therefore, it seems that the graphene and HOPG are electrically very sensitive to adsorbents and defects [86–91]. The mechanical load capacity of graphene is important during SFM and STM measurements, since the mechanical tensile strength is just 1.25×10^{11} Pa, albeit only in the ideal state of graphene [75]. For an assessment, one may compare the load capacity with pressures that can occur during SFM measurements. When the forces are

typically in the range of 1 μN to 1 nN and dependent on the contact faces of the cantilevers used, the pressures are in the range of $1 \cdot 10^6$ Pa to $1 \cdot 10^{12}$ Pa. Therefore, it is possible that the graphene can tear during SFM and STM measurements. However, such a problem is not known for HOPG.

3.2.2 Mica

Mica is a layer crystal and belongs to the phyllosilicates whose single layers are very weakly bound to each other by layers of potassium counter ions [92]. In this work, muscovite mica $KAl_2(Si_3,Al)O_{10}(OH)_2$ was used solely (Fig. 3.5). This material turned out to be a useful substrate due to several reasons. It is birefringent and optically transparent with a common, light colouring. Muscovite is an umbrella term: There are various species due to the differing intercalated ions such as manganese, calcium, chrome, etc., which exhibit themselves in their bright colouring. When the crystal is cleaved (by tweezers and razor), one can obtain a very clean and atomically flat surface. The cleavage is mostly along the potassium ions K^+, whereby it may be assumed in a good approximation that a statistically equal number of ions should be distributed onto newly obtained surfaces. The further chronological evolution of the ions is not entirely clear. For example, it is known that the ions may chemically react with water in the exergonic mode. Without the potassium ions K^+ on top of the surface, the negatively charged oxygen $O(\delta^-)$ constitutes the surface, the oxygen atoms are covalently bound with Si or Al where the electron clouds are closer to the oxygen atoms and thus a negatively charged surface is formed. Despite surface coverage, mica has a corresponding surface charge in each case.

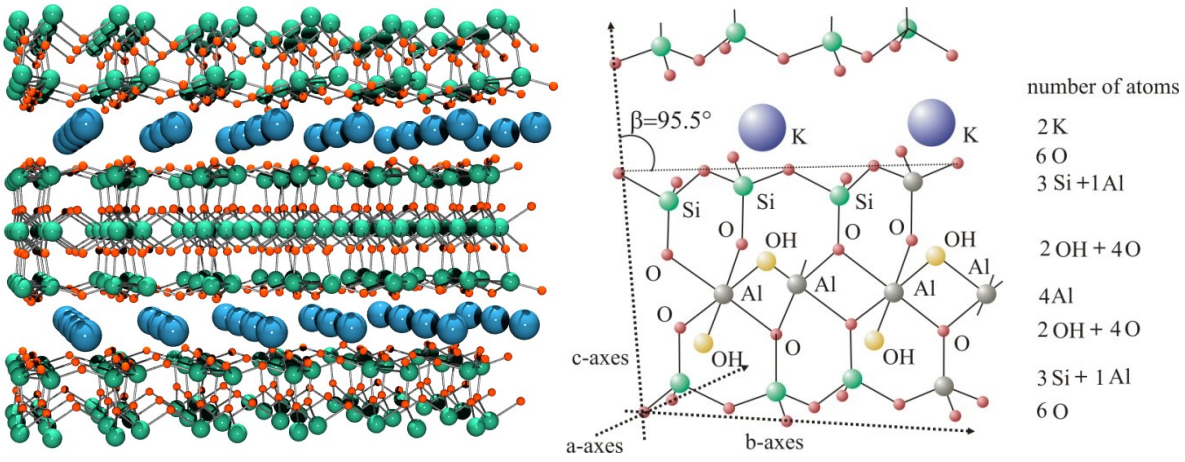

Figure 3.5 Mica is a layered crystal. On the left, a simplified scheme shows three planes that are bonded through the potassium ion layers, where primarily vdW forces occur [3]. The right side shows the unit cell with its atoms/ions [4].

[3] posted by Mark Foreman's Blog, 2012
[4] based on Hu et al., 2003; (redesigned)

Beside the atomically flat surface, mica also has a clean surface after a fresh cleavage. These features make mica a prototypical surface and substrate for experimental investigations of surface and interface, such as in combination with graphene.

3.2.3 Water

Water is an omnipresent material: in all three aggregate states, water is more or less always present with many exceptional properties [93–96]. It is almost impossible to keep the water away from experiments or to remove it from surfaces, pores and interfaces. Water in its molecular appearance is a sp^3 hybridized molecule (symmetry point group C_{2v}), where the two hydrogen atoms are covalently bound to oxygen (Fig. 3.6). The electron clouds are closer to the oxygen whereby a negatively charged oxygen δ^- and positively charged hydrogen atoms δ^+ form and constitute a strong dipole moment of about 1.85 D.

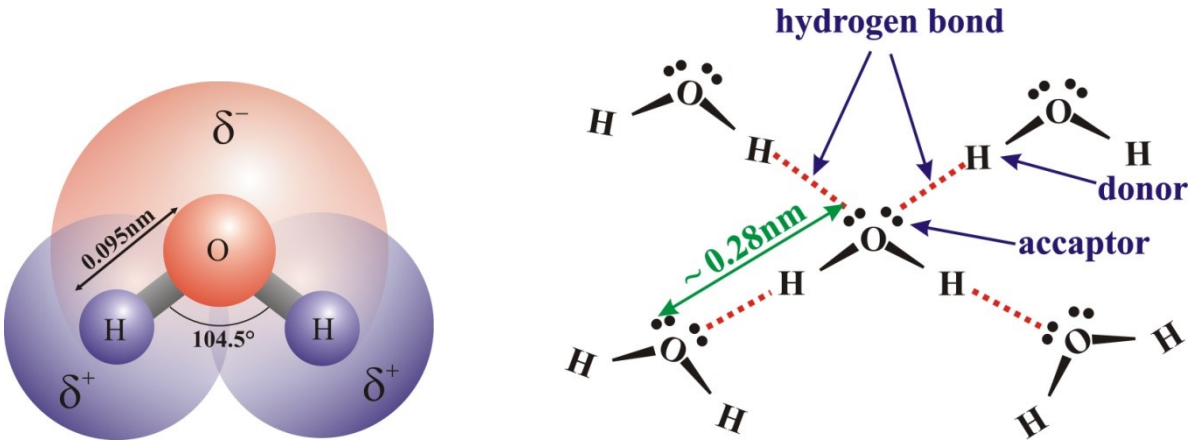

Figure 3.6 The left sketch shows the water molecule and its polar charges δ^- (red) and δ^+ (blue). On the right a scheme of a conceivable water network is shown, where the hydrogen bonds (red dots) act between the molecules. Interestingly, the average distance between the molecules is about 0.28 nm, which will be further explored in Chapter 4.2.

There is a characterisation of the adsorption property of water onto surfaces, although this concept is not really useful since this implies a not clearly defined limiting value for distinguishing if a surface is hydrophobic or hydrophilic. In principle, water adsorbs onto all surfaces, albeit with more or less strong adsorption energies and forces. For example, the adsorption of water onto the mica surface [97, 98] is stronger due to the polarised surface (dipole - dipole interaction) than onto graphene [99] due to the delocalised π-electron surface (dipole - induced dipole interaction). The adsorption of water onto graphene counteracts the desorption which is dependent on the thermal energy kT and the relative humidity, which leads to a very low coverage of the graphene surface.

It is known that water forms networks where water dissociates from H_2O to H_3O^+ and H^- and back, respectively (Grotthuss mechanism) [100–103]. Less known is the behaviour of water in a more or less strong, electrostatic field [104–107]. The phenomenon is observable in a simple experiment when a stream of tap water is close to an electrostatic field such as an electrically charged rod. The dipoles of water molecules are aligned along the field, whereby an attractive force always occurs in direction of the rod. This phenomenon is independent of the sign of the charges. At higher electrostatic field strength above 10^9 Vm^{-1}, there are further interesting phenomena dependent upon in which state water or ice is arranged. Accordingly, the dissociation might take place, a reorganization of the crystal structure or conversion into another phase [108]. These field strengths are easily accessible in very small distances (10^{-9} m) m, since the revealed voltage via the surface charges is around 1 V (i.e. 1 V / nm). As a comparison, one may consider a capacitor

$$E = \frac{U}{d} = \frac{1}{\varepsilon_0}\frac{Q}{A} \Rightarrow \frac{Q}{A} = \sigma = E\varepsilon_0 = 8.85 \cdot 10^{-7}\,\frac{As}{cm^2} = 5.5 \cdot 10^{12}\,\frac{charges}{cm^2} \qquad [2.8]$$

The surface charges at those field strengths are comparable with those of mica without potassium ions of about 2.1×10^{14} charges per cm^2 and mica with potassium of about $1.1 \cdot \times 10^{12}$ charges per cm^2 [109–111]. Water is always present and adsorbed very well onto the polar mica, whereby "graphene covered mica" constitutes a prototypical system where water can be intercalated via the adjustable relative humidity [16].

3.2.4 The Porphyrin-Spiropyran Dyad and their Components

The porphyrin-spiropyran dyad used in this work was synthesized by Chandan Maity[5]. The dyad is constituted by zinc-tetraphenylporphyrin (5,10,15,20-tetraphenyl-21H,23H-porphine zinc) and nitro-spiropyran (1',3'-dihydro-1',3',3'-trimethyl-6-nitrospiro[2H-1-benzopyran-2,2'-(2H)-indole], which was attached via a flexible 1,2,3-triazol linker (/spacer) (fig. 3.7). The dyad was selected with the intention to control the electrical transport through a single molecule, which should adsorb as a monolayer onto a suitable surface such as HOPG or graphene. The most appropriate experimental setup is based upon the STM technique that will be presented in the following section. As mentioned above, HOPG is a very appropriate substrate for these investigations. However, it requires appropriate requirements on the dyad. On the other hand, the dyad should have a function whereby the electrical transport - i.e. the electrons in the tunnelling junction - can be selectively controlled. These goals are best reached with a merger of single molecules with the suitable functions, thus merged to a dyad. The feature of an anchor has been accomplished by the tetraphenylporphyrin, which is from the group of heterocyclic macro cycles and well known - with suitable substituents - to adsorb well onto HOPG [112–115]. According to Liao and Scheiner [116], one may recognize the effect of the complex bound of the central zinc ion to HOPG. The nitro-spiropyran takes on the role of the functionalized unit, which may change to its isomer merocyanine via incident light with a suitable wavelength (Fig. 3.7). With respect to its switching behaviour, the nitro-spiropyran in use is a very complex molecule [35, 117, 118]. Here, "spiropyran" refers to the closed form, where the C-O bond still exists. As soon as this bond is detached, the open form is called "merocyanine". There are many different conformations that differ through the line along central five carbon atom bonds from nitrogen to oxygen. Both *trans* (T) and *cis* (C) exist for the planar conformations and TS# (# numbers) for the turned ones. The energy differences between the individual conformations are thoroughly in the eV range. A peculiarity of the spiropyran turn to merocyanine is the change of the strong dipole moment of about 10 to 15 Debye [119]. Based upon this switching behaviour and its equilibrium states, the solvatochromism has a strong effect via the variation of polarity of solvents, which may be explained essentially by two different mechanisms. The first one is the change of the equilibrium states of isomers through the shift of their energy levels relative to each other, because the effects of the solvent to each isomer are different. The second mechanism is a general phenomenon of the solvatochromism based upon the solute-solvent interaction, determined through the interaction of

[5] AG Prof. Hecht, Department of Chemistry, Brook-Taylor-Str. 2, Humboldt-Univerität zu Berlin, 12489 Berlin Germany

respective dipoles and their screening effect. The isomers feature a more or less strong, different dipole moment to each other, whereby the respective effect is also different. Based upon the strong dipole moment, the isomers also have an effect on each other, manifest through the J-aggregation and the H-aggregation [35, 120–124]. This phenomenon is especially observable at the planar merocyanine. J-aggregation describes a stacking that is determined through the parallel alignment of the dipoles, while H-aggregation means that the dipoles are aligned anti-parallel to each other. These phenomena could become interesting when the dyads are adsorbed onto HOPG or graphene, interact with the dissolved dyads and attend through a solvent with its affects.

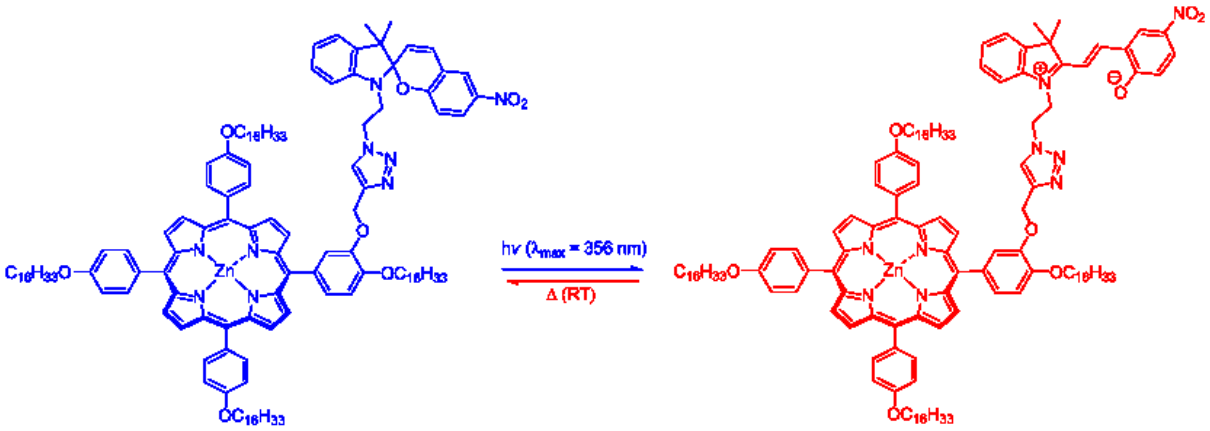

Figure 3.7 The porphyrin-spiropyran dyad and its isomerisation to the merocyanin dyad by means of irradiation with a suitable wavelength. The merocyanine (right) has a TTC form and is one of several metastable conformations of the open isomers.

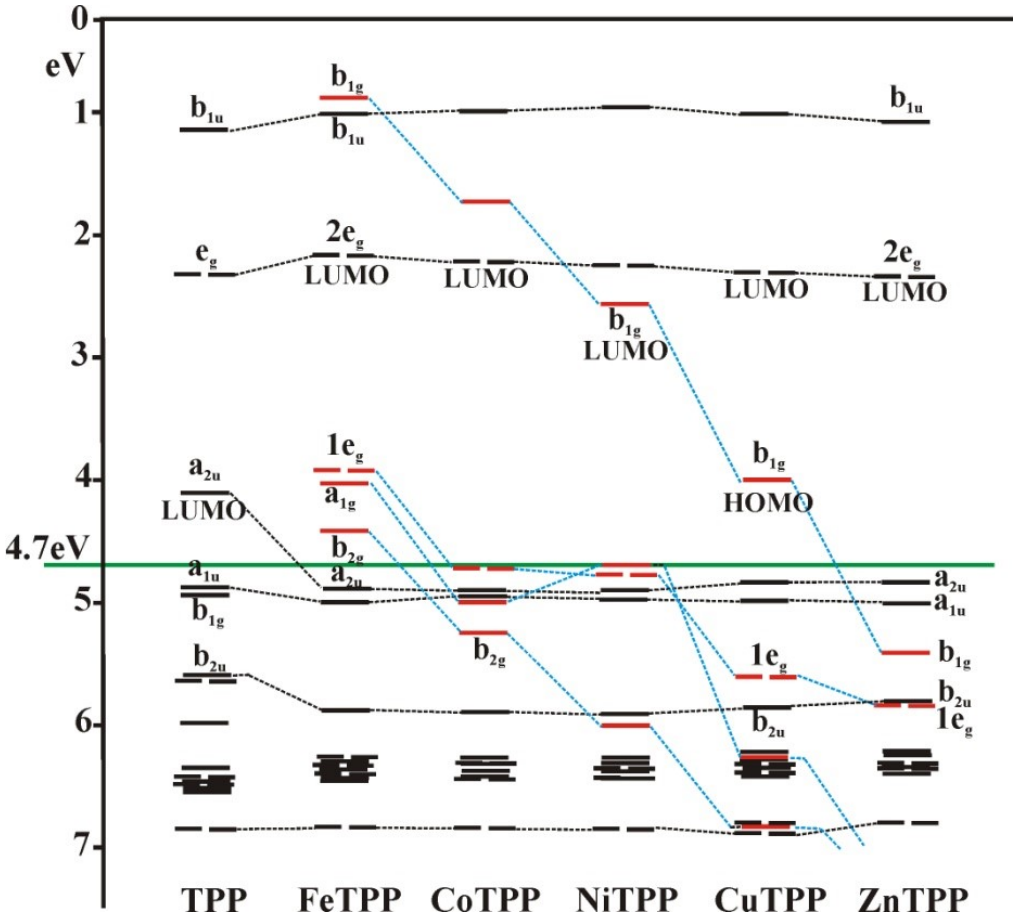

Figure 3.8 The energy schemes of some metal porphyrin derivates (MTTP). The green line indicates the Fermi energy of graphene (for HOPG, the Fermi energy changes to about 4.6 eV).

The UV / VIS investigation of the porphyrin-spiropyran dyad in use and its corresponding nitro-spiropyran derivative are shown in Figs. 3.9 and 3.10, respectively. The spectra in (a) show the spiropyran → merocyanine isomerisation via the irradiation at 357 nm. The start spectrum (black) has maxima in the UV region, while no intensity is observed at wavelengths above of 420 nm. During the irradiation, the intensities are increased between (360 - 460) nm and (460 - 650)nm, as indicated by the black arrows. The thermal back reaction at 10°C is shown in (b) and leads back again to the start line. This switch behaviour is reversible. The results are typical for the spiropyran merocyanine isomerisation, when one considers the solvatochromism through the solvent 1-octanol [128–132]. The spectroscopic results of dyad in the UV / VIS are shown in Fig. 3.10. Now, the start spectrum of the dyad is that of the ZnTPP. The band at 427 nm is caused by the two Soret and B bands, whereas the peaks in the region from about 500 nm to 650 nm are those of four possible Q bands. The latter could be understood as a transition between the a_{1u}, a_{2u} and the two e_g states (compare Fig. 3.8). There are simultaneously two B bands - which constitute the transition between ground state and the second excited state, and the four Q bands. Therefore, the states a_{1u} and a_{2u} are presented separately, i.e. both have different energies and the two e_g states are doubly degenerated. Based upon the equivalent absorption spectra of the dyad and its single components, one may assume that the components connected to the dyad do not affect each another. The thermal back reaction of the dyad has a time constant $\tau = (35{,}7 \pm 1{,}8)$ min and is calculated by

$$y(t) = y_0 \cdot \exp\left(-\frac{t}{\tau}\right). \qquad [4.11]$$

Here, y(t) are the time-resolved intensities at 561 nm, y_0 is the start intensity, t the time and τ the time constant at which the intensity is dropped to e^{-1} times of y_0. This time constant is taken as a the reference for the comparability with the switch experiments on the surface. Since the setup, the irradiation geometry and thus the intensities are different from the solute-solution system and the surface adsorbed dyad, the "switch on" time constant τ_{on} is not suitable as a comparative parameter.

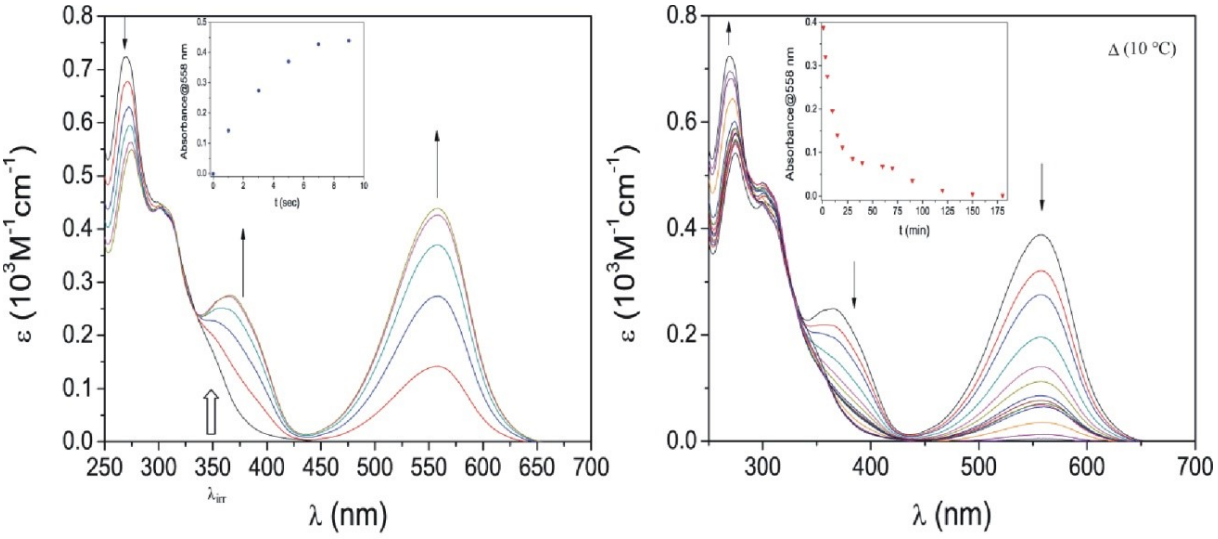

Figure 3.9 The UV / VIS spectrum of the separate spiropyran derivate used in the dyad. The left image shows the isomerisation to the open form, dissolved in 1-octanol and irradiated at 356 nm.

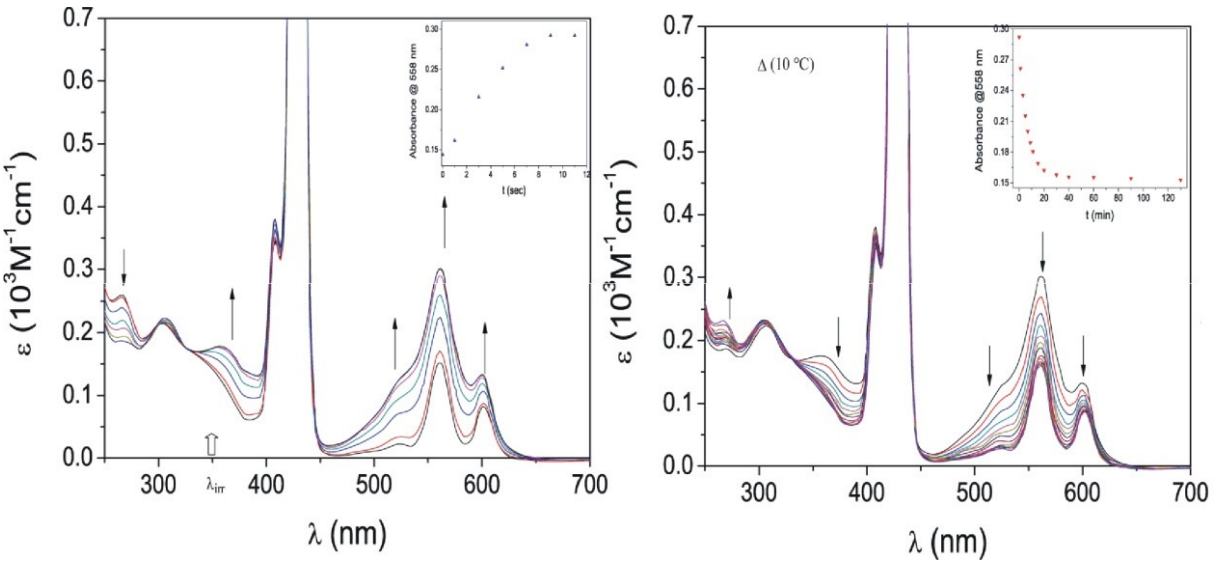

Figure 3.10 Absorption spectrum of porphyrin-spiropyran dyad (c = 1 × 10^{-5} M) in 1-octanol. Left: spectra recorded at varying intervals during irradiation with light of 357 nm wavelength; right: spectra recorded at varying time intervals after irradiation at 357 nm for 15 sec (thermal back reaction at 10 °C).

3.3 Experimental Setup

The experiential setup, which is essentially used for the surface as well as interface investigations, is a combination of our self-made STM with a commercial reflected light microscope (AXIO Observer A1m, Zeiss). The schematic layout of the setup is shown in Fig. 3.11 and the corresponding, labelled images are shown in Fig. 3.12. The STM comprises the STM head, controller (Omicron) and a commercial PC with the software Scala Pro. The self-made STM head comprises three identical drooping piezos, which are attached to the basic frame via a circular aluminum plate and three springs. The basic frame stands firmly on the reflective microscope. Through the drooping piezos, the sample holder can be mounted magnetically on the bottom side, whereby the sample is accessible for the microscope. Via the three springs, both plates are held together with flexibility, quasi free-floating. In the centre of the top plate, the tip holder - which comprises an identical piezo as the other ones - is firmly attached and penetrates through a hole in the centre of the bottom plate. The relative position can be set via three finely thread screws. These penetrate through the top plate with the corresponding inner thread and thus keep a distance from the bottom plate. Therefore, the bottom plate with the piezos and thus the sample is freely swivel-mounted around the tip in all three directions (x,y- plane and in z-direction, the distance between tip and sample). The threads have a pitch of 500 µm per full turn, i.e. a rotation of 1° has as a z-shift of about 1.4 µm and thus approximately the same shift in the other directions. Since the graphene pieces are typically smaller than 10 µm × 10 µm, the pitch is relatively large to adjust the tip onto the graphene. The tunnelling currents are amplified and converted in a voltage by a preamplifier. These signals are used by the controller unit for their visualization, as well as controlling the piezos via adjustment with the set points given by the user (compare PID controller). The optical reflective microscope is a commercial device from Zeiss company, the AXIO Observer A1m. The essential constituents are the light source, an input-side transmission filter, an objective revolver, two polarisers crossed by 90°, camera output, an eyepiece and various slides for changing optical paths.

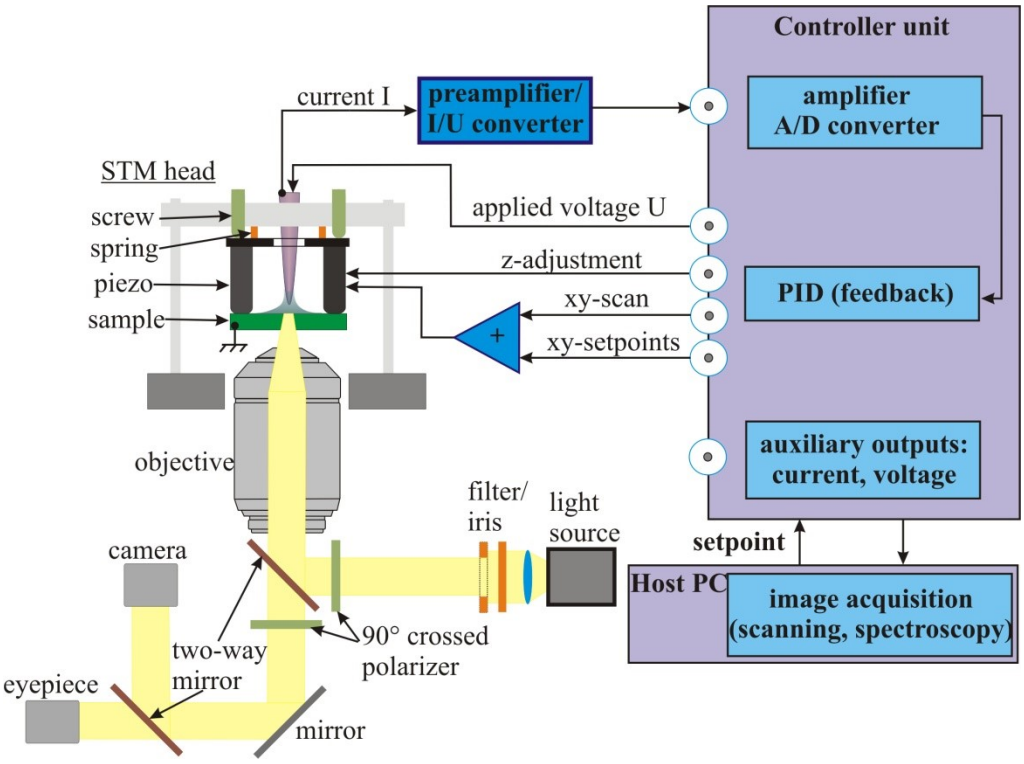

Figure 3.11 The experimental setup of the used STM, which was extended by a reflected light microscope.

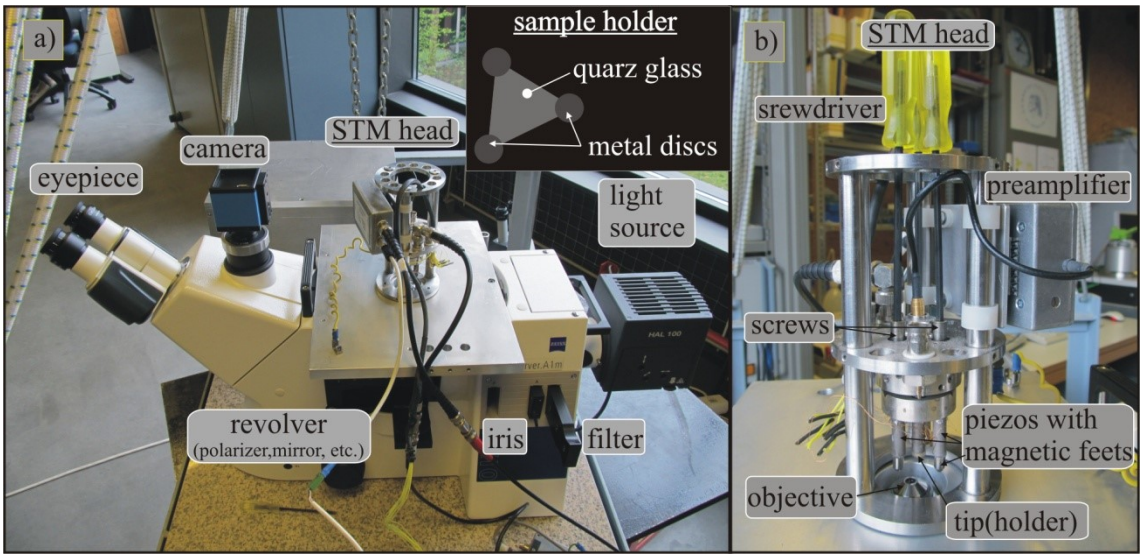

Figure 3.12 The images show the STM setup.

4. Results and Discussion

The experimental investigation of functionalized surfaces begins with the choice of the suitable substrates and investigation methods. In the ideal case, the substrate has a well-defined and prototypical character with well-known and accessible properties. The combination of optical microscopy with scanning probe microscopy (SPM) - especially the STM – provides a promising possibility for time-resolved, high spatial resolution measurements. However, this means that the substrate is also optically transparent and electrically conductive. Therefore, this chapter deals with the characterisation of the sample. Besides, the investigation of interfaces with high, i.e. atomic resolution and surface phenomena based upon mono- and multi-layer graphene samples is considered and potential mechanisms are discussed at the end.

4.1 The Optical Properties of the GMQ Sample and the Behaviour of Solvent 1-Octanol

4.1.1 Introduction

As already introduced in detail in chapter 3.2.1, graphene is a hexagonal lattice of carbon atoms that are covalently bonded via sp^2 hybridisation. Graphene is similar in the surface structure and the electronic properties to HOPG and thus has wide usage as a substrate in science [74]. The spatial structure results in remarkable mechanical properties, especially a large Young's modulus (E = 1.0 TPa) and a high stiffness (D = 2TPa) [75]. The unique electronic band structure (linear dispersion relation in the k, k' points [76, 77]) manifests itself, for example, in a carrier density ($n_e = 5 \cdot 10^9$ cm^{-2}), carrier mobility ($2 \cdot 10^5$ cm^2/Vs) [78] and a visual transparency of about 98% [79]. Due to these properties, graphene is an ideal material for well-defined prototypical substrates as well as samples itself (see chapter 4.2). However, the first big challenge was the preparation of clean and graphene, as large as possible, onto freshly cleaved mica. In the following, the sample was characterised especially by STM.

Despite these mechanical properties, graphene has to be mechanically supported by mica and quartz glass to be used in STM measurements. This combination of graphene onto mica and onto quartz glass is called “GMQ sample”. Here, mica plays the role of an atomically flat and visually transparent substrate for graphene. Nevertheless, the system “graphene on mica” is still too susceptible for acoustical influence in conditions of the natural environment, whereby graphene onto mica has to be additionally supported via a quartz glass holder. The graphene flakes had a typical area less than 100 μm^2. As mentioned in the previous chapter, the adjustment of the

STM tip on top of the graphene was in the same range. Therefore, the approaching had to be supported by the optical microscope (compare Fig. 4.4). Because the optical path was through the GMQ sample, it had to be ensured that there is distortion-free optical imaging and a sufficiently high intensity over a wide wavelength range. Furthermore, the dyad absorbed onto graphene was switched with light with a wavelength of 365 nm. Therefore, it had to be ascertained whether the sample was suitable for this way of experiments for a functionalized surface.

The experiments began under conditions of natural environment (room temperature, humidity) and were continued on a solid-liquid interface with the solvents 1-phenyloctane and 1-octanol. The latter was used for the switching experiments on the STM. 1-phenyloctane is a well-known solvent in terms of usage on a STM without significant influence on the measurements, and was used for the characterisation of the sample as the first choice. In contrast, the 1-octanol was previously unknown but indispensable for the investigation of switching behaviours of the dyad. Therefore, in the following sections we consider the characterisation of the GMQ sample and its optical properties as well as the effect of the solvent 1-octanol on the STM measurements.

4.1.2 GMQ Sample: Optical Properties

The quartz glass holder was cleaned up sequentially by dish soap, acetone and ethanol in an ultra-sonic bath, before being purged with distilled water and then dried in air. The used mica was from Ratan Mica Exports (V1 - optical quality). For the characterisation of the optical properties, mainly at the 365 nm line, optical transmission measurements were carried out at different thickness of mica. Mica has to be always cleaved for a clean surface where the graphene can be set on top. After one-time cleaving – now called “thick” - mica had one clean surface, while the non-cleaved opposite side was still contaminated. After mica was cleaved a second time, one obtained a piece - termed as “medium” - where both sides were clean. The thinnest mica piece that could be cleaved in a meaningful manner was referred to as “thin”; it was expected to have the best optical properties. The main disadvantage, however, was the mechanical instability. The transmission measurements were performed at natural ambient conditions. Each one of the samples described above, quartz glass and mica pieces, were measured separately. A holder at the instrument ensured an almost perpendicular incidence of the light onto the samples. The reference signal of the optical sample path was obtained through air.

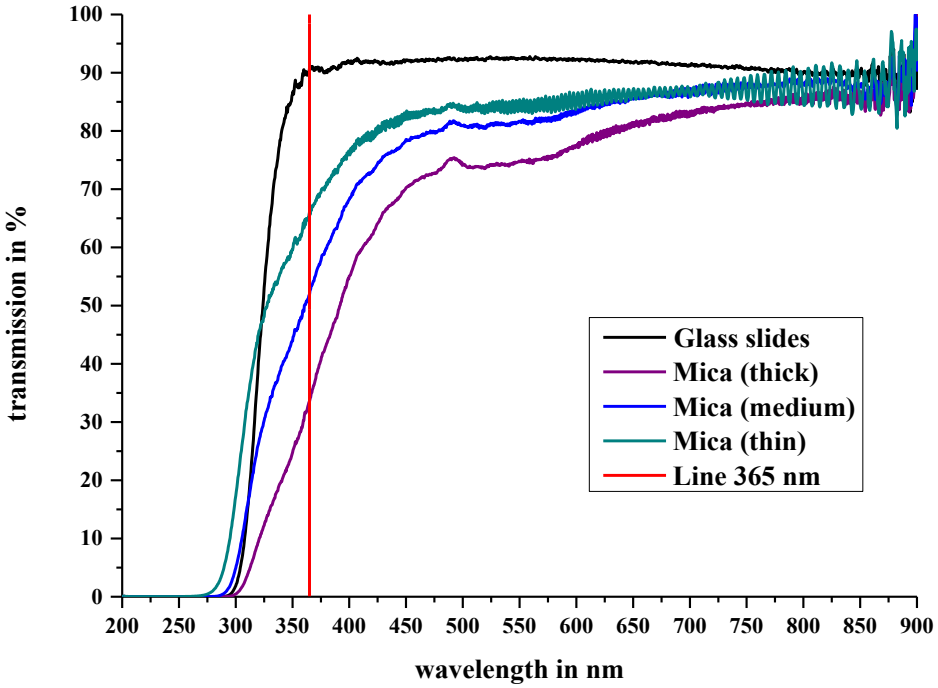

Figure 4.1 Spectroscopic transmission measurements of the four samples: quartz glass (black), thick mica (one times cleaved), medium mica (both sides one time cleaved) and thin mica (thinnest). The red line indicates the 365 nm wavelength, which was used during the switch experiments. The mica pieces used for the switch experiments had a transmission from 50 % to 65 % at 365 nm.

The results of the transmission measurements are shown in Fig. 4.1. The first curve (black) shows the transmission spectrum of quartz glass. The region of the spectrum is relatively flat and features a transmission of more than 90 % for wavelengths longer than 350 nm. For wavelengths below 350 nm, the curve had a very steep decrease (cut at 305 nm; slope of 10 %). The spectra of thick mica (violet) show a slight decrease, but the steepest of all shown, with a transmission from 85 % to 65 % in the wavelength range from 900 nm until about 450 nm, respectively, followed by a steep decrease at wavelengths of below 450 nm (from 65 % to about 0 %). The medium mica (blue) shows a slighter decrease of the transmission from 85 % to 75 % than the thick mica in the same wavelength range. The slope is a little steeper and thus the curve always has a higher transmission than thick mica. The spectra of the thin mica (turquoise) shows a fluctuation of the transmission for wavelengths below 900 nm, which becomes smaller with a shorter wavelength. The reason for this is the interference of reflected and transmitted light on both surfaces of mica (note the short coherence length and divergence of light source and beam path of an UV / VIS

spectrometer). The red line indicates the light with a wavelength of 365 nm, i.e. the wavelength for a conformation change of the dyad. The intersections of the red 365 nm line with corresponding transmission spectra indicates the weakening of the intensity at 365 nm when passing through the sample. In summary, the transmission is 90 % for glass, 65 % for the thin, 50 % for the medium and 30 % for the thick mica. The optical microscope generated a measured radiation power density of P_{obj} = 685 mW / cm² at the 365 nm wavelength behind the objective and at the relative position of the GMQ sample (cf. the setup, as described in chapter 3.2).

The radiation power density of 685 mW / cm² was primarily the result of the light source (Hg lamp) and the objective "EC Plan-Neofluar 40 ×/ 0,75 M27". The low-pressure Hg lamp has a powerful 365 nm line and the objective increased the power density of the incident light through the 40 × magnification as well as the numerical aperture (NA) of 0.75 despite the transmission of the objective of 60 % at 365 nm. The light had to penetrate the GMQ sample to illuminate the dyads adsorbed on graphene. Thus, one obtains the resulting radiation power density for the illumination of the dyads by the following Eq. [4.1].

$$P_{STM} = P_{obj} \cdot \left(T_{glass} \cdot T_{mica} \cdot T_{gr}\right) \qquad [4.1]$$

Here, P_{STM} is the expected power density for the adsorbed dyads, P_{obj} is the incident power density onto the sample and T is the transmission of each corresponding component (glass, mica pieces and graphene). Equation 4.1 exposed, together with the transmission spectra, the strong influence of the transmission of each component at a wavelength of 365 nm. The contribution of mica pieces is much larger than of quartz glass (about 90%) and graphene (98%). The mica pieces had a transmission that was very dependent on their thickness, from 30 % for thick mica to 65 % for thin mica. Accordingly, for the cleaved mica with the thickness in use, the transmission T_{mica} was in the range of 50 % - 65 %. The power density was

$$P_{STM}\ (\lambda = 365\ nm)^{6} \in [\ 302\ ,\ 393\ ]\ mW / cm^2$$

It still needs to be clarified whether the illumination power density is sufficient. We estimate the rate how many photons encounter a adsorbed dyad. The dyad has a object field of about A_{dyad} = 7.85 10^{-17} cm² and the energy of the photon with the wavelength at 365 nm is E_{ph} (365nm) = 5.45 10^{-19} J = 3.4 eV. Thus, the rate is calculated by the following equation

[6] This means that, due to the uncontrollable thickness preparation of mica pieces for switch experiments (see section 4.3), an irradiation power density from 302 mW / cm² to 393 mW / cm² was available.

$$\Gamma = \frac{P_{STM} A_{dyad}}{E_{ph}} . \qquad [4.2]$$

The explicit unit of Γ is photons per second and dyad (s^{-1}). Thus, the rate is in the range of $\Gamma \in [45 , 57] s^{-1}$, i.e. one dyad may be hit by 45 to 57 photons per second. However, this does not mean the photons interact with the dyad. The absorption cross-section - which induces a switch event - is approximately in the magnitude of about $\sigma_{switch} \in (10^{-18} , 10^{-21})cm^2$. Therefore, one may assume that the adsorbed dyads will have a switch event within some minutes, approximately one hour. Finally, one may assume that the irradiation power density at a wavelength of 365 nm should be sufficient for the switch experiment with the STM because both time scales, the line wise scan of STM and the switching events that are determined by the incident number of photons, are of the same magnitude.

4.1.3 The Solvent 1-Octanol: Properties and Implications for the Experiments

The used solvent 1-octanol was manufactured by Sigma Aldrich. For the measurement of the ionic character of the solvent, a small quartz glass slide was used, a non-insulated Pt / Ir wire (diameter 250 µm, 80 % Pt and 20 % Ir) for oneelectrode (probe), HOPG which is freshly cleaved on both sides (ZYG, Advanced Ceramics) for the other electrode and a current-voltage measuring device (Keithley Digital). The glass slide was cleaned up via glass slide soap in a ultra-sonic bath, before being purged successively with distilled water, ethanol and 1-octanol and finally dried in air. With object holders, the HOPG was attached as well as the wire in the glass slide filled with 1-octanol. The contact area of the HOPG was almost as large as the full crystal - i.e. without the metal discs - whereby only the HOPG was in contact with the solvent. The contact area of the wire probe was about A_{probe} = 4 mm². The current-voltage measurement was carried out by pre-setting the applied constant voltage and the subsequent measurement of the current after a suitable delay time (in this case some ten seconds). The delay time became necessary because the 1-octanol exhibited a polarity effect, whereby after the change of voltage the current exponentially changed.

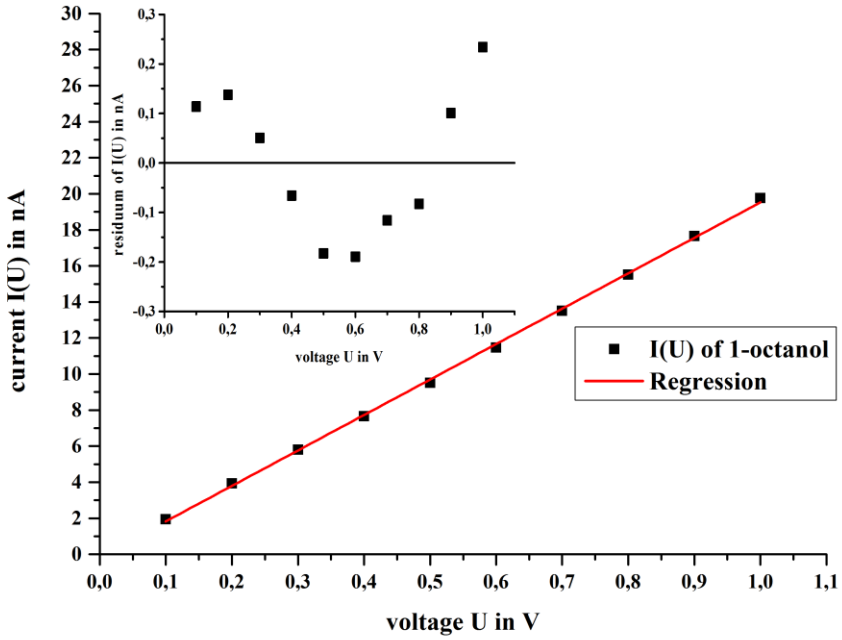

Figure 4.2 Current I [nA] of 1-octanol in dependence of voltage U [V]. Solid rectangles are the measured values, the red line is the linear regression of the measurements $I(U) = I_0 + R^{-1} \bullet U$ with $I_0 = -(0.1 \pm 0.1)$ nA and $R = (51 \pm 6)$ MΩ. The inset shows the residuum of the regression. A probe area of about A_{probe} = 2 mm² results in a specific resistance of about $\rho = 102\ \Omega\ m^2$.

Figure 4.2 shows the result of the current-voltage measurement. The solid rectangles are the measured values and the red line is the regression calculated by the following equation

$$I(U) = I_0 + \frac{U}{R} . \qquad [4.2]$$

Here, $I_0 = -(0.14 \pm 0.11)$ nA is the current at U = 0V, U is the applied constant voltage in a region of [0.1, 1.0] V , R = (51 ± 6) MΩ is the ohmic resistance. I_0 should be close to the coordinate origin (zero) due to the ohmic character of the measurement. In this way, I_0 indicates the correctness of the measurements being carried out, which is the case here. For the estimation of the additional current at the STM by the 1-octanol, the specific resistance ρ [Ωm²] and resultant current have to be calculated under the estimation that the contact area of the STM tip with the solvent is A_{STM} = 400 µm².

$$\rho = R \cdot A_{probe} \qquad [4.3a]$$

$$I_{ion} = U_{gap} \frac{A_{tip}}{\rho} \qquad [4.3b]$$

The specific resistance of 1-octanol was calculated to about ρ = 102 Ω m² with a contact area of the probe of A_{probe} = 2 mm². With the estimation that the applied gap voltage of the STM was typically in the range of U ∈ [0.3 , 1.3] V, an additional current range could be estimated to I_{ion} ∈ [1.2 , 5.0] pA, which depends on the voltage. For comparison, the applied current was typically in the range of I_{gap} ∈ [10 , 60] pA at the STM in the imaging mode and independent of the voltage.

It turned out that the used solvents 1-phenyloctane and 1,2,4- trichlorobenzene (1,2,4-TCB) - which could have been used at the STM - were unsuitable for the switch experiment, because the switch spiropyran as well as the dyad did not exhibit an indication for a reversible isomerisation: more precisely, the dyad and the spiropyran showed indications that the molecules were destroyed. However, the dissolved dyads in 1-octanol revealed a stable reversible isomerisation. This solvent had a voltage-dependent ohmic current I_{ion}, which was about one-tenth of the applied gap current I_{gap}. The reason of the ionic current is that the 1-octanol may be a Lewis base as well as an acid in combination with the applied gap voltage of the STM. Thus, the quality of the STM measurements significantly deteriorated. The reason for this phenomenon can be found in the exponential distance dependence of the tunnelling current and the superposed linear distance dependence of the ohmic current. In other words, the tunnelling current depends exponentially on the distance and forms a small tunnelling current tube between the tip and the conductive surface, thus ensuring

atomic resolution. The ionic current depends linearly on the distance according to the ohmic law, thus ensuring a superposition of the ionic current of a large area around the tunnelling current tube and resulting in a significant deterioration of the resolution. At low voltage, the tunnelling current dominates (< 0.6 V) and at higher voltages (> 0.7 V), the ionic current until the measured current will be too strong and the tip is retracted. In the present case of the dyad, the detection limit is approximately at values of > 0.5 V. Furthermore, fluctuations in the ion current also cause disturbances. These are so strong that the scanning tunnelling spectroscopy (STS) could not be performed: The noise of the ionic current was stronger than the true measurement signal. The STS measurements would have been useful to obtain the HOMO and LUMO level(s) of the molecules.

4.2 STM Investigations of a Graphene-Based Interface and Surface

4.2.0 Introduction

i) Graphene onto mica constitutes an interface and thus forms a slit pore in which the intercalated water always exists at ambient conditions with relative humidity (below 4 % to over 60 %). The interaction between graphene and mica affects the manifestation of enclosed water [16]. In this process, mica and graphene together play an important role due to the surface properties of mica and the electrical properties of graphene during the draining (dewetting) and filling (rewetting) of the slit pore with water at the corresponding relative humidity. This behaviour has been investigated well by SFM, Raman and Kelvin Probe Force Microscopy (KPFM, resp. Surface Potential Microscopy SPoM), but is not fully understood [15–19].

An additional investigation method is STM, which contains topological as well as electrical investigations, as presented in the first part of this section.

ii) Functionalized surfaces constitute a special subarea of the surface and induce interface phenomena. In particular, the intended interaction of the surface with its surroundings can be manipulated by different external influencing factors [5–12]. The functional module spiropyran-porphyrin dyad adsorbed self-assembled onto HOPG or graphene and thus constitutes a functionalized surface, which can be switched by light with a suitable wavelength of 365 nm. This switch mechanism may be affected by the intermolecular interaction with neighbouring molecules and the interaction with the conductive surface, e.g. steric hindrance or quenching [26–34].

In the second part of the following section, the the switch behaviour of the adsorbed spiropyran-porphyrin dyad onto HOPG is investigated, as well as on single- and multi-layer graphene at the solid-liquid interface and at room temperature.

4.2.1 STM Investigations of a Graphene-Based Interface at Different Relative Humidities

4.2.1.1 Graphene on Mica: Roughness and Flatness

The quartz glass holder was cut via a glass cutter from a purchased ordinary quartz glass slide to an equilateral triangle with an edge length of about (3 – 3.5) cm. The glass was cleaned up with ethanol and three small metal plates were attached via superglue at each one of the three corners. Thereafter, the triangular quartz glass holder with the three small metal disks at the corners was cleaned up again via dish soap in an ultra-sonic bath and subsequently purged with distilled water and ethanol and finally dried in air. The first mica piece was cut out from a bulk, purchased mica piece (Ratan mica Exports, V1 (optical quality)) via scissors (no razor, due to - among other things - the very high number of few broken, nm-sized mica pieces). In this process, the mica piece was cracked sideways caused by the cutting motion of the scissors. This piece had to be sufficiently large to maintain an adequately large, available area which exhibited no cracks for the subsequent exfoliation of graphene. This mica piece was cleaved at least twice by a razor blade to obtain a clean piece on both sides. During this procedure, the mica pieces were held with purified tweezers and the hands did not touch the sample at any time. HOPG (ZYB, Advanced Ceramics) was used to obtain graphene via exfoliation. The HOPG was cleaved via adhesive tape to obtain a clean surface. HOPG may be considered as multi-layered graphene. In some cases, one end of a multi-layer graphene flake was detached from the HOPG and could be handled with tweezers to obtain a small mono- and multi-layer graphene piece. The results of graphene production are random to a large extent: the graphite flake adheres onto the mica surface and the graphene flakes are weakly bonded to each other with the same force. The direction of the tear off is oriented along a random graphite (graphene) plane, with statistical fluctuations. This flake was placed onto the prepared mica surface and gently pressed via the tweezers. For an increased chance of receiving more graphene, the mica was covered entirely with more flakes of graphene, aside from the cracked edges. Subsequently, the multi-layer graphene flakes were stripped onto mica with tweezers. Nonetheless, the yield of sufficiently large graphene (several nm in size) was very low.

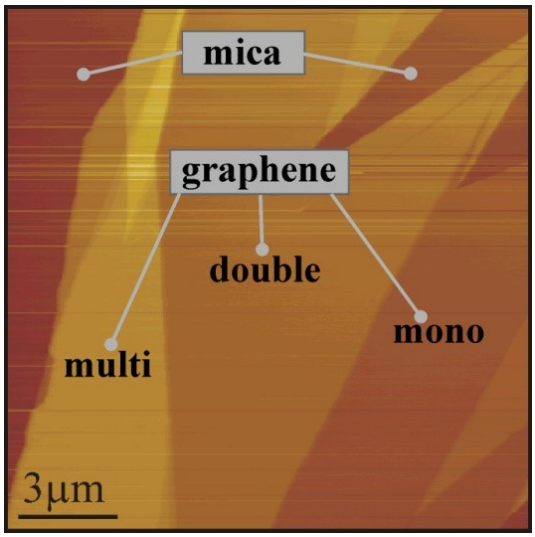

Figure 4.3 Typical SFM height image of a mono- and multi-layer graphene on mica at natural ambient conditions.

After evaluating the graphene (compare Fig. 4.3) through SFM (JPK AG, NanoWizard® III), mica layers oppositely to the graphene were removed until the remaining graphene-mica compound was sufficiently thin (c.f. Sect. 4.1.2; transmission at wavelength of 365 nm). Subsequently, the thin graphene-mica sample was cut to the side of the quartz glass holder via scissors. Now, there were also no cracks at the edges due to the cuts, because the mica piece was too thin. The graphene-mica sample was placed onto the quartz glass holder. Through the two-component silver conductive glue, the metal plates were connected with the multi-layer graphene of which the monolayer graphene was a part. Additionally, the mica was also fixed on the glass holder with the glue. Thereby, a GMQ sample was obtained for the STM investigations, which were carried out by the self-built STM with an Omicron controller (Omicron NanoTechnology GmbH) with Scala Pro V5.0 software (c.f. chapter 3.3). The cap of the STM and the table of the optical microscope constitute a closed chamber, in which nitrogen could be purged for an adjustable relative humidity. The humidified nitrogen was prepared using a bottle purged with nitrogen (water bubbler), which was filled with distilled water. The relative humidity could be regulated with the flow rate.

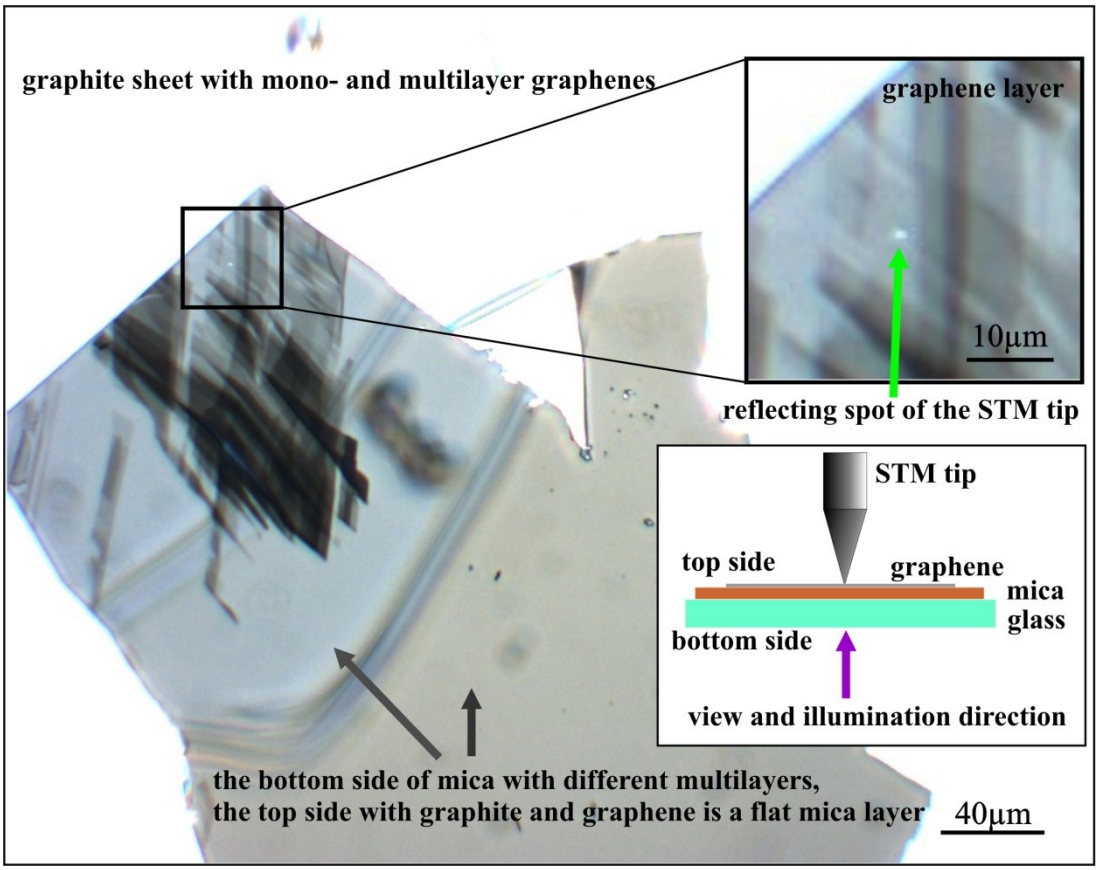

Figure 4.4 The image shows the GMQ sample, viewed in the direction as seen in the sketch. The bright spot is the reflection of the STM tip, which is seen in further detail in the upper right inset. The tip is approached on top of the graphene layer, i.e. in the tunnelling distance of less than 1 nm. During the approach, the spot changes its brightness mutually between dark and bright, owing to interference of the incident light between tip and graphene.

The first step was to evaluate the sample flatness and roughness by the STM, carried out at the solid-liquid interface (1-phenyloctane) for a higher resolution. The approach of the tip onto the graphene was carried out in dry condition at the beginning, because the visual supervision via the optical microscope only works without liquid film on the surface. A liquid thin film caused - among other effects - interference and distortions to the image of the reflective STM tip , as long it is still far above the sample. In detail, closer to the surface but still far away from the tunnelling distance, a meniscus would be formed out from the surface up to the tip and distorts the image of the tip. Therefore, the approach of the tip onto the surface becomes impossible in wet conditions. Accordingly, following the approach of the tip onto the graphene in dryness (in tunnelling distance), the solvent 1-phenyloctan was added via a syringe[7], whereby the solvent enclosed the

[7] The used syringes were examined in advance and did not show any emission in the compound of 1-phenyloctan and 1-octanol, which might have otherwise affected the measurements and investigations.

tip as well as the surface. The scan area was from (150 × 150) nm² to (4.5 × 4.5) µm². In this range, it had been measured with the intention to obtain the flatness and roughness of the monolayer graphene on an atomically flat mica surface. The STM has a scale limit of about (6.5 × 6.5) µm² ($\frac{1}{\sqrt{2}}$ 6.5 µm = 4.6 µm at 45° turning of the scan area).

In Fig. 4.5, two representative STM height images of monolayer graphene on atomically flat mica are shown. The used parameters for the left image were U_{gap} = –0.14 V (gap voltage), I_{set} = 59.5 pA (feedback set), LG = 39.6 % (loop gain) and v = 17438.6 nm / s (scan speed). For the right image, the parameters were U_{gap} = –0.91 V, I_{set} = 43.0 pA, LG = 89.3 % and v = 2929.69 nm / s . The left image in Fig. 4.4.1 shows a scan area of 2 µm × 2 µm, while the right image 4.4.2 displays a scan area of 150 nm × 150 nm; both had the same resolution of (1024 × 1024) pixel. The images are not drift-corrected. The right image also contains a cross-section (white horizontal line, fast scan direction), which is shown in the inset. Both images are line-wise corrected for flatness (SPIP; LMS fit degree 1, i.e. linear).

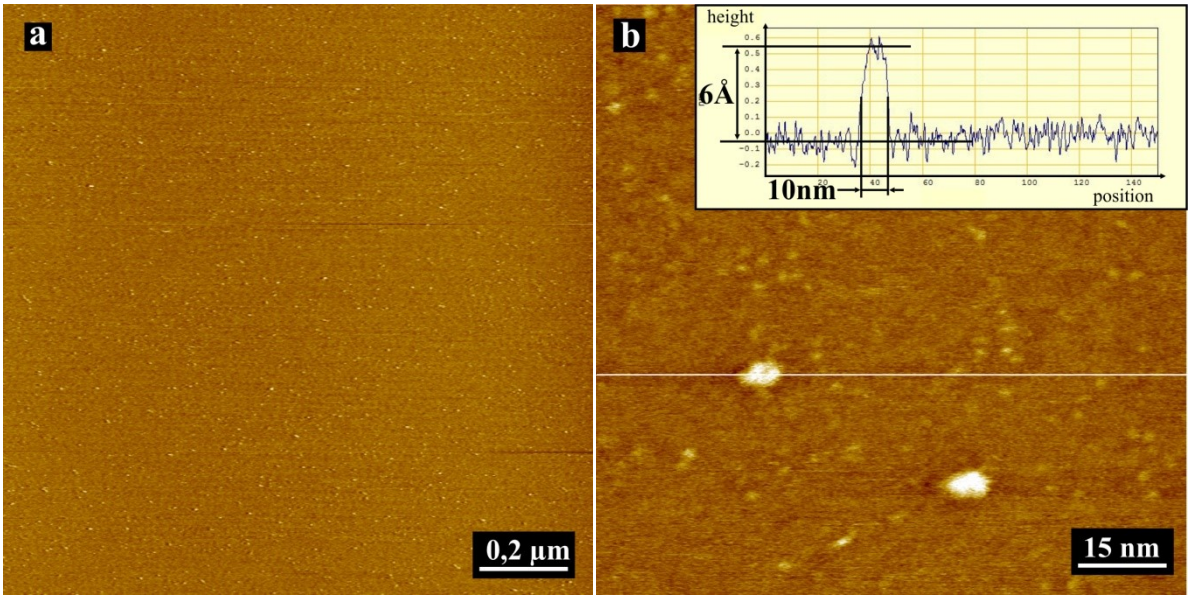

Figure 4.5 STM height images of graphene with a size of 2 µm × 2 µm (left, U_{gap} = –0.14 V, I_{set} = 59.5 pA) and 150 nm × 150 nm (right, U_{gap} = –0.91 V, I_{set} = 43.0 pA). Both images have a pixel resolution of 1024 × 1024. The two dots on the right side are particles on top of the graphene.

In the left image 4.4.1, one can see a more or less homogeneous distribution of very small irregularities on the surface, which seems very flat otherwise. In the right image 4.4.2, about 13 times magnified, one can distinctly see two large (white) irregularities surrounded by other smaller irregularities. The height of the irregularities was smaller than about 1 nm (compare Tab. 4.2), as

one can see in the cross-section (0.6 nm in the cross-section). The roughness of the graphene on the atomically flat mica surface was quantified via the root-mean-square S_q (rms; Eq. (4.4a)) and via the ten-point height S_z (equation 4.4b), which were calculated by SPIP (ISO 4287/1).

$$S_q = \sqrt{\frac{1}{mn}\sum_{k=0}^{m-1}\sum_{l=0}^{n-1}(z(x_k, y_l))^2} \qquad [4.4a]$$

Here, it can be noted that the mean value is not subtracted from the individual values ($z - \bar{z}$; difference of one measured value z and the mean value $\bar{z}$), because the mean value is subtracted via the line-wise or plane correction at zero degrees and higher. Without these corrections, an incorrect value is obtained.

$$S_z = \frac{1}{5}\left(\sum_{i=0}^{5}|z_{pi}| + \sum_{i=0}^{5}|z_{vi}|\right) \qquad [4.4b]$$

Here, z_{pi} and z_{vi} are the heights of the five highest local maximums and the five lowest local minimums, respectively. However, only at a previous plane or for line-wise correction a correct and useful value is received for S_z. Thereby, the values were calculated for the image 4.3.1 to S_q = (42 ± 2) pm, S_z = (0.8 ± 0.1) nm and for the image 4.3.2 to S_q = (76 ± 4) pm, S_z = (1.1 ± 0.1) nm. For a better overview, the values are shown again in the following tables.

Table 4.1 Parameters of the STM height images in Fig. 4.5

image	**gap voltage U_{gap} = [V]**	**current set I_{set} = [pA]**	**loop gain LG = [%]**	**image speed v = [nm/s]**	**object cut-out C = [µm]**	**grid numbers g = [pixel]**
4.4.1	–0.14	59.5	39.6	17438.6	2.0 × 2.0	1024 x 1024
4.4.2	–0.91	43.0	89.3	2929.69	0.15 × 0.15	1024 x 1024

Table 4.2 Roughness values (SPIP, ISO 4287/1) of the STM height images in Fig. 4.5 and the data for its validation.

image	**rms S_q[a] = [pm]**	**ten-point height S_z[a] = [nm]**	**grid resolution R_g[b] = [nm/pixel]**	**scan resolution R_s[b] = [nm]**	**relation R_s / R_g = [pixel]**
4.4.1	42 ± 2	0.8 ± 0.1	1.95	5.87	3.01
4.4.2	76 ± 4	1.1 ± 0.1	0.146	0.43	2.99

a : the values S_q and S_z have been calculated by Eq.s. (4.4a) and (4.4b), respectively.
b : the values R_g and R_s have been calculated by Eqs. (4.5a) and (4.5b), respectively.

$$R_g = \frac{c}{g} \qquad [4.5a]$$

$$R_s = \frac{v}{LG \cdot f_0} \qquad [4.5b]$$

In Tab. 4.2, three further values R_g , R_s and their relation - with the threshold (cut-off) frequency f_0 = 7.5 kHz - are shown. This frequency is given by the hardware of the STM (primarily the preamplifier). The values R_g, R_s determine the maximum response time of the STM. The STM can respond to changes in the measured parameters, which also determines its resolution capability. Therefore, these three values are used to evaluate the characteristic parameters root-mean-square (rms) and ten-point height of the measured STM height images. The time constant $\tau = (LG \cdot f_0)^{-1}$ approximately represents the response time of the controller on an input signal that is similar to a Heaviside step function ($1\tau \equiv 63\%$; $3\tau \equiv 95\%$). This time constant is converted to the length scale via the scan speed v. Hence, the scan resolution R_s, can be derived, which approximately defines the minimum object size that the controller device can resolve. However, the object is scanned on a grid, i.e. the scan is discrete, whereby data of the object may be lost (Nyquist's sampling theorem). Consequently, the grid resolution R_g should be finer than the scan resolution R_s. This fact is implied in the relation R_s / R_g. For both images, the value was about R_s / R_g = 3, i.e. in the fast scan direction the minimum object size of R_s = 5.87 nm and R_s = 0.43 nm, respectively, were sampled with three pixels (this corresponds to 3τ). The roughness parameters S_q and S_z imply that all objects larger than 5.87 nm and 0.43 nm, respectively, have been considered and all smaller objects have not. The electronic noise of the STM - which was measured with the retracted tip - was $S_q = (4.5 \pm 0.1)$ pm, being one magnitude smaller than the roughness. The electronic noise should be therefore not responsible for these values.

In both cases, the roughness of the graphene on mica surface - expressed by root-mean-square values - in relationship to the line-wise correction via SPIP implies an atomically flat surface. Additional, the ten-point height values of about 1 nm imply that the irregularities that one may identify as small dust particles mostly lie on top of graphene and not below, if one assumes that all the particles that were higher than 1 nm are wiped by the STM tip.

4.2.1.2 Graphene on Mica: Lattice Structure

The results of the investigation of the lattice structure of the GMQ sample at a solid-liquid interface via the STM measurements (1-phenyloctan) are now presented and discussed below. The preparation is the same as described in 4.2.2.1. After approaching the tip onto the graphene, it was necessary to wait until the STM signal had achieved a marginal constant noise and drift (in the lateral and z-direction) to enclose finally the tip and the surface by the solvent 1-phenyloctane. Two types of measurements were carried out: the current images, where the height was kept constant; and the height images, where the current was kept constant. These were implemented via the variation of the scan speed v and loop gain LG, whereby the gap voltage U_{gap} and the current set I_{set} were kept constant. The results of the height and current imaging of the graphene lattice structure are representatively shown in Figs. 4.6 a) and b) as well as c) and d), respectively. The corresponding parameters are listed in Tab. 4.3.

Table 4.3. Measurement parameters of the images in Fig. 4.6 and the corresponding calculated resolution capabilities.

image	**gap voltage U_{gap} = [mV]**	**current set I_{set} = [pA]**	**loop gain LG = [%]**	**image speed v = [nm/s]**	**grid res. R_g=[pm/pixel]**	**scan res. R_s = [pm]**
a) & b)	−104	641	14.03	162.760	4.88[a]	154.7[b]
c) & d)	−104	641	0.370	244.141	4.88[a]	8799

a): Object cut-out 5 nm × 5 nm and grid size 1024 pixel × 1024 pixel;
b: C-C bond length of graphene is 142 pm and the length of each unit cell vector 246 pm.

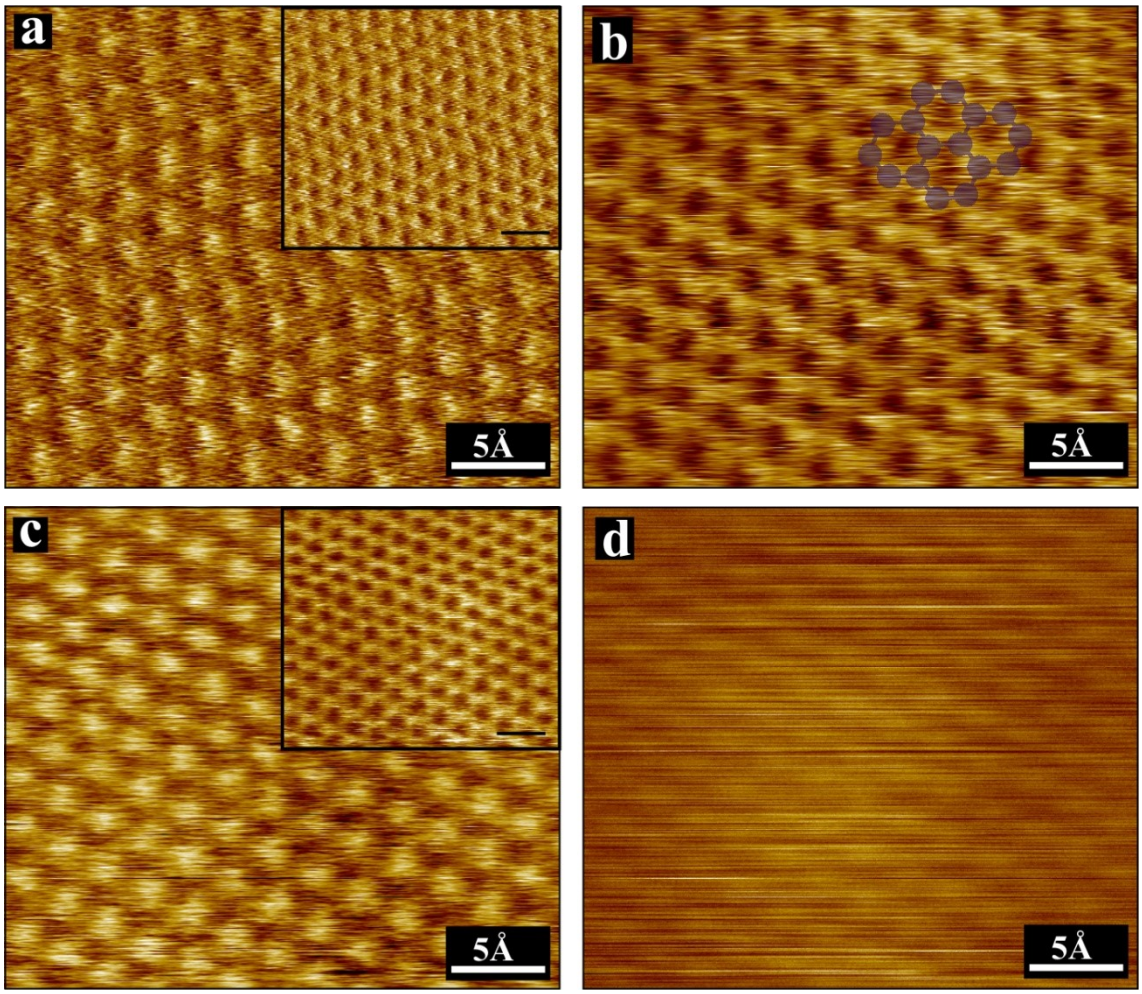

Figure 4.6 The images show four STM measurements of a monolayer graphene on mica at solid-liquid interface; each two current images (**a** & **c**) with their corresponding height images (**b** & **d**). The sign-corrected current images are shown in the respective upper right corners, whereby the typical honeycomb structure appears. The images **a**) and **c**) show the constant height mode and the images **b**) and **d**) show the constant current mode. The honeycomb structure is homogenously flat. The parameters are shown in Tab. 4.3.

Table 4.3 is organized in a part concerning the measurement parameters (gap voltage U_{gap}, current set I_{set}, loop gain LG, image speed v) and a part concerning the evaluation parameters (grid resolution R_g and scan resolution R_s). For the respective images, height and current, the gap voltage and current have been kept constant. Therefore, the tunnelling distance has also been kept constant. However, what has changed is the scan resolution R_s (not to be confused with grid resolution R_g) via the scan speed and the loop gain, i.e. the sensitivity: With high sensitivity, one scans more height and less current, while with low sensitivity, one scans more current and less height. The scan resolution of image 4.4.1 of about R_s = 155 pm was in the order of the magnitude of a C-C bond length of 142 pm and the unit cell vector length of 246 pm. For better understanding, a brief

explanation of the evaluation of the STM measurement data via the program SPIP (Image Metrology) follows. The STM saves the current with its correct sign, corresponding to the applied voltage which is set by the gap voltage U_{gap}. A negative applied voltage results from a negative current and vice versa. Due to the feedback loop, the tip is retracted via the applied piezo voltage by the controller, when the level of the current is too high. Via this voltage, one obtains the height image, whereby the value of the current corresponds to the height. SPIP shows the data with the correct sign. However, this also means that the highest negative values of current are also represented by darkest colors (deepest). Thus, one obtains a current image suggesting that the bright dots are associated with the highest values of current. For the correct representation, one has to take the amount of the values of current. In the following figure, the histogram of image 4.4 c) with the corresponding response of the system (STM controller) is shown.

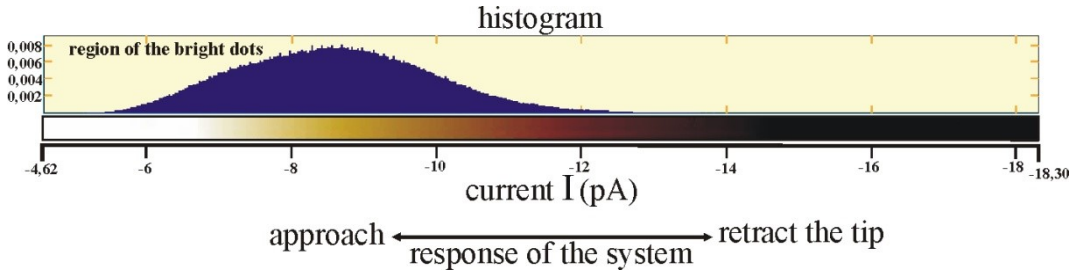

Figure 4.7 The histogram of the measured current-signal (one data file). Weaker current values are displayed as higher points by SPIP than the stronger current data, which leads to a wrong representation of data (compare with Fig. 4.4).

The histogram shows the low current values on the left side (corresponding to the bright dots in the image) and the highest current values on the right side (darker regions). The amount values of the current are shown in the right upper corner of the corresponding image. In these images, one may see a honeycomb lattice, whereby the carbon atoms and the bonds have the highest current values and thus the highest local density of states (LDOS) of the graphene. In Fig. 4.6, the honeycomb structure - i.e. the density of states and not the carbon atoms themselves - is shown.

However, at a relative humidity below 4 %, fractals were revealed where graphene no longer lies on the monolayer water but rather on the pure mica surface, following the currently favoured opinion [15–17, 19, 130]. Now, one can measure graphene on different surfaces and thus investigate the relative interaction of the surface with the graphene via the change of the LDOS of the graphene. This will be described and discussed accordingly in the following section.

4.2.1.3 Graphene-Mica Interface at Different Relative Humidities

In this section, the previously described GMQ sample was used at different relative humidities. Graphene on mica constitutes an interface where the density of states is affected by the interaction of the surface charges of mica. However, this method provides an ideal possibility for the atomically resolved investigation of the LDOS of graphene and thus for the derivation of conclusions concerning the interaction mechanism between graphene and mica. Therefore, the questions which arise are: Which relative different LDOS may be measured and how insight into the interaction mechanism may be inferred from these measurements?

The STM standard setup was expanded by a meter of humidity (testo 635 from Testo GmbH) and a port which is adjusted to the relative humidity of the chamber via humidified nitrogen flow. The latter comprised a bottle (water bubbler) filled with distilled water (Milli-Q) through which the dry clean nitrogen gas was humidified. The dry nitrogen was taken from the in-house system. The investigation focused on the different LDOS of graphene on different surfaces and not the dynamics of the dewetting and rewetting of the slit pore itself. Therefore, the measurements were only carried out at humidities below 4 % and over 60 % (two thresholds). It should be noted that the STM chamber could not be sealed airtight for many reasons.

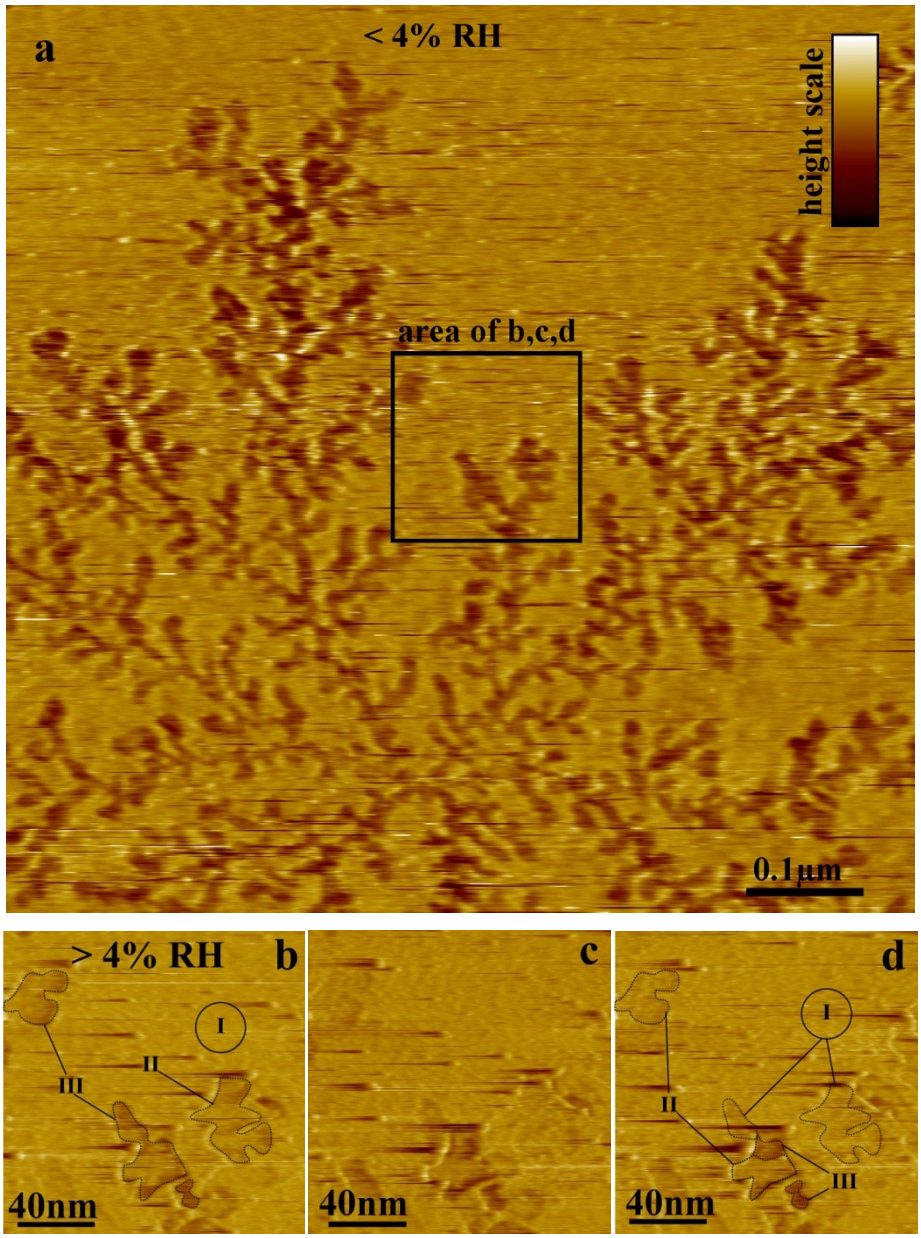

Figure 4.8 The STM height image a) shows a fractal at below 4 % relative humidity (RH). The star-shaped fractals had a width in the magnitude of a few micrometres. The black rectangle is the area of the time-resolved height images b), c) and d), with a delay time between the images of about 2 min. Just after the scan of image a), the slow nitrogen flow was steered through the water bubbler, whereby the RH was increased. 6 min after the image a) and while the nitrogen was purged in the bubbler, the sequential scans for images b) to d) were started. Height changes are visible. The analysis can be found in Tab. 4.4. All measurements (a - d) were carried out at the same parameters U= –1.05 V, I = 40.4 pA, LG = 100 %.

In Fig. 4.8, a representative STM height image is shown for the measurements of graphene with fractals below 4 % relative humidity. The images are not drift-corrected. The sequence of images b) to d) shows a zoom-in area of image a) (black rectangle). Just after the scan of image a), the nitrogen flow was steered through the water bubbler, whereby the RH increased. 6 min after the image a) and while the nitrogen was purged inthe bubbler, the sequential scans of images b) to d) were started. In a), one may see the graphene surface with fractal-like branches. These structures had mostly one centre from which the structure grew star-shaped to a fractal. The branches of indentations had a width of about (10 – 20) nm. The size of the fractals was larger than 1 µm in the diameter. These two parameters are merely for guidance. The structures with their corresponding characteristics are identified as fractals by Severin, N. et al [16]. The focus lies on the "depth" of the fractals (compare it with Fig. 4.9) and thus allows inferring to the LDOS of graphene and interaction strengths between the different surfaces and graphene. The depth of the fractals was analysed by SPIP (line-wise correction degree zero, global correction degree one). Here, the three height images b) to d) have been analysed. The procedure implied the mean value determination of several subareas within a structure edge and thus of different surface types. Finally, all mean values of the same surface type were averaged. Thus, the analysis and evaluation resulted in three different mean values, which are shown in the following table and illustrated in Fig. 4.9.

Table 4.4 S_i are the mean values of the fractal heights and $\Delta S_{I,j}$ are the differences of depths in relation to S_I.

	S_I [Å]	S_{II} [Å]	S_{III} [Å]	$\Delta S_{I,II}$ [Å]	$\Delta S_{I,III}$ [Å]
mean values	+ (0.5 ± 0.2)	- (1.3 ± 0.2)	- (2.9 ± 0.5)	1.8	3.4

For the following interpretation of the measurements and the results of the analysis, a question emerges: What is known and what may be supposed about the present system? Graphene is a highly conductive, atomically flat monolayer that follows very well the shape of the surface [131], whereby the smallest atomic height changes of the surface are mapped by graphene. Mica is a layered crystal, whereby along the cleaving plane an atomic flat and clean surface is formed. It is supposed that both cleaving planes have a statistically equal number of potassium ions. However, an explicit proof is not possible with respect to the distribution of potassium ions and the reaction with parts of air during the applied preparation procedure. Here, some brief comments concerning potassium are necessary, which are not discussed in the literature in this context. At first, it is assumed the potassium is homogeneously distributed over the surface, although this was not yet

proven by an experiment. It is known that pure potassium undergoes a rapid, exothermic reaction with water and the oxygen from air ($\Delta H_R < 0$). In such cases, the processes are exergonic ($\Delta G_R < 0$), too. The significant reaction equations are as follows:

$$K + O_2 \rightarrow KO_2 \qquad [4.6a]$$

$$2K + O_2 \rightarrow K_2O_2 \qquad [4.6b]$$

$$2K + H_2O \rightarrow 2KOH + H_2 \qquad [4.6c]$$

$$K_2O + H_2O \rightarrow 2KOH \qquad [4.6d]$$

However, whether a reaction occurs by itself ($\Delta G_R < 0$) is dependent on the total energy balance, which is implicitly written as follows:

$$\Delta G_R = \Delta H_R - T\Delta S \qquad [4.7]$$

In the case of potassium on mica, the question emerges concerning which sign the entropy change ΔS has at room temperature. With a positive sign, the reaction is exergonic ($\Delta G_R < 0$). With a negative sign and if the entropy change ΔS is sufficiently large, then potassium ions may exist on the mica surface. Since the end products of Eqs [4.6] may not necessarily exist in the ambient air on mica - i.e. the partial pressure is zero - these molecules are quite likely removed from the mica surface by the concentration-dependent balancing processes and e.g. replaced by water. Since in the literature this specific case is not described, the status of potassium ions on mica could not be clarified, although all discussed processes have to be considered. Whether with or without potassium ions on the surface, the mica surface exhibits a global as well as local surface charge density σ_m (x,y) [132]. In order to verify, by which the LDOS of graphene may be affected and how it can be measured by the STM, the following part of this section is sub-divided in two parts, first the most likely mechanisms are discussed and secondly, a model is developed.

The determination of the locations of the potassium ions is important, because the existence of potassium ions (K+) may strongly determine the processes within the slit pore. It is already stated that the water layer that lies in-between is a monolayer. The height measurements of this sample by SFM in this work exhibited no additional height difference between the water layer and a possible K^+ layer. Maybe the effective diameters of water and of K^+ are consistent within the measurement accuracy of a SFM. However, other measurement methods also did not indicate the

location or the distribution of the potassium ions within the slit pore. The major reasons for this "blindness" of methods are the coarse resolution capability and the superposition of signals, whereby significant single signals are hidden as well as the fact that the water and potassium layers are covered by mica and graphene, whereby significant signals are screened or scattered. The effective ion diameter of potassium lies between 2.76 Å [135] and 3.04 Å [136].The size of water ranges between 2.82Å [137] and 3.2Å [138]. Hence, the measured height of both is not necessarily different, presupposing that this simple model is correct. The distances of the ions, molecules and atoms (K^+, H_2O, OH^-, H^+ and products like Eqs. 4.6) to the mica and graphene depend on each part of the ionic and van-der-Waals bond energies and forces, whereby the higher the ionic part, the closer the molecule and the potassium ion to the surfaces. The same fact is also applicable to the graphene on mica or a layer on mica, making it plausible that the measured height differences are primarily determined. However, much more important is the fact that each component affects the LDOS of graphene differently, which can be measured by STM. Here, it is useful to distinguish between three different observable systems on which graphene may adsorb: i) pure mica (negatively charged), ii) closest packing of potassium ions (positively charged) and iii) homogeneous packing of potassium ions (neutral). The aspects have been described theoretically in the publications of Rudenko et al. [139]. This involves the investigation of the surface charges of mica in three cases of potassium coverage (neutral, positive and negative) as well as the influence on graphene that lies on top of these surface types (without water). The calculation of the surface charges in the special case of the "neutral" coverage led to a non-zero global field strength that exists in the near field. This has an effect on the DOS of the on top-lying graphene, which has a small Fermi level shift to a lower work function ($WF = E_{vac} - E_F$) and thus is coupled with an n-type doping of graphene (+ 0.02 e^-/cell), as well as the adhesion energy of graphene (–29.3 meV / C-atom) with a vdW part of 92 % between mica and graphene. The graphene is doped strongly positive (+ 0.91 e^-/cell; n-type) and negative (– 0.50 e^-/cell; p-type) at negatively and positively charged mica surfaces, respectively. Therefore, the three mica surfaces should be clearly distinguishable indirectly by the coverage of graphene and the measurement by STM. However, there is also the water layer, which changed the DOS and the Fermi level and thus the doping of graphene. The influence of the water to graphene is described theoretically in the publications of Leenaerts et al. [140] and Freitas et al. [141]. The publications are consistent in the fact that the relative adsorption energy and the influence on the DOS depend on the relative orientation of the dipole moment of the water to the surface of graphene, whereby the collinear alignment of the H-O binding arms is stronger than every perpendicular alignment. The relative strength and the type of the doping effect are experimentally confirmed by Schedin et al. [91]:

water is a weak acceptor and there is a p-type doping effect of graphene. Note that the doping effect depends on the isotropy of the underlying water layer (see Leenaerts et al. [140]). As the doping effect of the negatively and positively charged mica surface is stronger than the water, the STM detection of separated domains (the negative, positive and water-layered negative mica surface) have to be clearly measurable. There is only one problematic case concerning the almost homogeneous distribution of the potassium water layer, constituting a stand-alone acting layer. Therefore, one has to assume that water and potassium ions may not be distinguished. The distribution of potassium ions and water on the mica surface is described theoretically by Malani and Ayappa (2011) [97]. The result of a 3D distribution of water and potassium ions has been described by Odelius et al. in 1996 [142]. The major results are that there are four layers of water and two layers at very low pressure. The first layer is at the level of the potassium ions and has a strong alignment of the dipoles perpendicular to the surfaces. The second layer is less ordered and lies over the first layer of potassium and the first layer of water. Both layers cannot be completely removed by reducing the partial pressure. The third layer is mostly disordered and is only removable at low pressure ($p/p_0 < 10^{-2}$). The forth layer is disordered and has a distance to the third layer of about 2.7 Å. The preparation of the sample in a glove box takes about 10 min. In this time and at a partial pressure of about $p/p_0 = 10^{-6}$ (p_0 = 35 mbar), the average number of collisions Z with the surface is given by

$$Z = \frac{p}{\sqrt{2\pi mkT}}. \qquad [4.8]$$

Here, *m* is the molecular weight of water, *p* the partial pressure, *T* the room temperature and *k* the Boltzmann constant. Thus, one obtains for the average number of collisions $Z = 1.25 \times 10^{16}$ $cm^{-2}s^{-1}$, i.e. 1.25×10^{16} water molecules collide onto the mica surface of 1 cm^2 per second. For comparison, after the mica cleaving the subsequent preparation time was several 10 min. According to the above mentioned theory, one can thus assume that the first two water layers always exist - including in a glove box - and constitute a homogeneous layer even if one considers that water molecules can be desorbed again. Through the additional graphene layer lying on top, one may assume that the electrostatic effect is enhanced (compare image charges over a metal surface, or Ren et al. [143]). Strikingly, the theoretically assumed distance between the third and fourth layer of about 2.7 Å was also measured for a fractal depth by a SFM (2.8 ± 0.5 Å). The facts described above of a few water layers on mica match well the results of the humidity-dependent investigation by Hu et al. [144]. Even if there are indeed these two layers, it is thus not yet proven. In relation to the results obtained by the STM, it has to be mentioned briefy again, that the STM

is sensitive to the LDOS. Moreover, the measured height is not the real height of the surface structure, but rather a superposition of the real height with the tunnelling distance given by the set parameters of the STM, which results in tunnelling resistance, respectively. The coincidence of the measured STM height with the value via SFM is rather random here. Therefore, it should be assumed that the results of the STM measurements can be only interpreted in two ways, either by the aforementioned theses (primer by Malani and Ayappa [97]) or the theories are wrong and there is only one water and potassium layer. The latter case may be excluded because there are no experimental and theoretical counterproofs at all: note for example Beaglehole and Christenson (thickness measurement by ellipsometry) [145] and Balmer et al. (thickness measurement by interferometery) [146]. The former - the multi-layer of water - is seemingly confirmed experimentally by Shim et al. [17]. The graphene on water was p-type doped $(9 \pm 2) \times 10^{12}$ cm^{-2} and was also p-type doped after the drying process, with much less surface charges similar to few-layer graphene (compare: the surface charges of graphene above "neutral" mica surface are given by Rudenko et al. with 0.02 e^- per cell $\equiv -3.8 \times 10^{13}$ cm^{-2} (n-type)). When one takes into consideration the results presented in Tab. 4.4 and Fig. 4.8, the fractal depth of $\Delta S_{I,III} = 3.4$ Å is similar to the depth measured by the SFM (2.8 ± 0.5 Å). The second fractal depth of $\Delta S_{I,II} = 1.8$Å was not observed with the SFM. Therefore, it can be assumed that this effect is specific to the STM. In relation to the fast scan direction, this phenomenon of heights was independent of the fast scan direction and reproducible on different, locally limited areas. Consequently, the observed additional depth is not a scan artifact. Since the STM is sensitive to the LDOS of graphene and it was found that there are water molecule layers under the graphene, it can be concluded that the relative alignment of the dipole moments is responsible for the change of the LDOS of graphene and thus for the additional depth.

This chapter should not be finished without taking a position on the most striking phenomenon of this slit pore. It is well known that the slit pore cannot be dried completely via reducing the relative humidity. According to the above discussion with a multilayer water, the drying process implies removing the top water layer in the pore. Accordingly, a possible explanation should be given in the following. For theoretical considerations, the slit pore is approximated as a spatial capacitor, as shown in the schematic sketch of Fig. 4.9. The charges of mica induce charges into graphene, depending on the layer lying in between, e.g. water or ethanol. Furthermore, the Fermi level of graphene is shifted according to the induced charges in graphene. The work function $WF = (E_{vac} - E_F)$ of graphene is equal to its electron affinity $EA = (E_{vac} - E_{cond})$ (energies are E_{vac} vacuum, E_F Fermi and E_{cond} conduction band), because there is no band gap.

When an absorber - e.g. water - comes into contact with graphene, a global equilibrium is established with a corresponding charge density as well as an alignment of the dipole moments of water. Depending on whether the EA of water is higher or lower than the WF of graphene, an n-type or p-type doping of graphene occurs, respectively. The layer in between has been approximated as a homogenous layer with parameters such as the dielectric constant ε_r, polarizability α and dipole moment **p**.

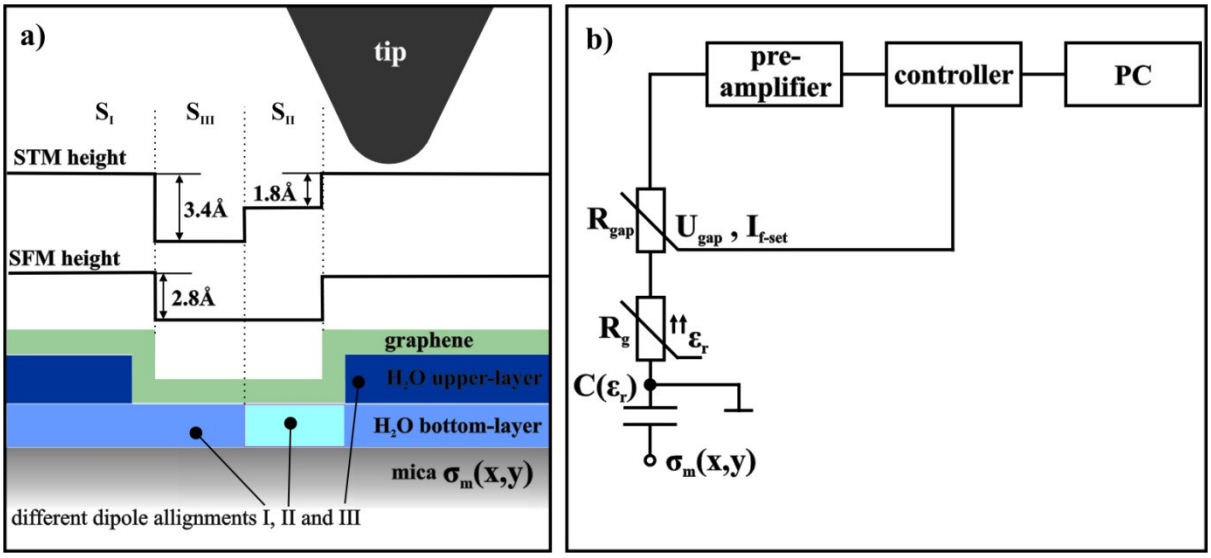

Figure 4.9 Sketch **a)** shows a cross-section of the sample with its measured heights by SFM and STM, which differ in their sensitivities. The bottom water layer contains two different domains (sky blue and bright blue) of water that are determined by the collective alignment of their dipoles. Sketch **b)** depicts the simplified electric circuit of the STM, where it is implied that the sample is an ordinary capacitor, affected by the dielectric. The graphene and its LDOS are constituted as a variable resistance, affected by the capacitor and thus the dielectric.

In Fig. 4.9, a schematic cross-section through the sample (a) and an equivalent circuit diagram of the STM (b) are shown. The cross-section shows the mica piece that has a surface charge density σ_m with the graphene sheet on top. In the slit pore, the water molecules are partially intercalated and these domains are highlighted in different colours. Steps in the graphene layer show a correlation with the number of water layers. In the above sketch, the cross-section of the height images by SFM and STM, respectively, is shown. Where the height is constant but the LDOS changes through the alignment of water dipoles, a height difference may also be measured by the STM in the constant current mode, where the SFM is not sensitive. The equivalent circuit diagram of the STM (b) includes the slit pore as a capacitor $C(\varepsilon_r)$ with a spatially changeable dielectric part. One side of the capacitor is charged equal to the mica surface charge σ_m. The other side - the

graphene sheet - is charged by mica surface charges but is also influenced by the dielectric.That is, when graphene lies directly on mica, the surface charges are equal, with a different dielectric constant ($\varepsilon_r > 1$). Therefore, this capacitor is different from conventional capacitors. The plates of a conventional capacitor are connected electrically via a constant voltage source, whereby a corresponding potential equalisation can be obtained between the plates. When both models are compared to each other with a dielectric constant of $\varepsilon_r \rightarrow \infty$ - i.e. complete compensation of the electric field - a conventional capacitor has an equal number of charges on both plates. In the case of graphene on mica, mica has surface charges and graphene is neutral in charge, whereby the electrical fields of mica surface charges cannot induce mirror charges in opposing graphene. The electrical resistance of graphene as a function of LDOS of graphene, affected by its surface charges (implicit by the mica and its ε_r), is represented by the symbol of a resistance R_g. The resistance of the tunnelling current is represented by R_{gap}. Its parameters are determined by the bias U_{gap} and the set current I_{set}. The initial equations are the modified Maxwell equations.

$$\mathrm{rot}\, E = 0 \qquad [4.8a]$$

$$\mathrm{div}\, D = \rho \qquad [4.8b]$$

$$\mathrm{rot}\, H - \dot{D} = j = 0 \qquad [4.8c]$$

The parameters used for the following approximation and the simplified sketch are shown in detail in Fig. 4.10. The piece of mica is sketched with edge lengths a and b. On top, two different domains I and II are located with the variable edge length b, (a-x) and c_I, or b, x and c_{II}, respectively. The coordinate system lies with x and y in the surface area and z is perpendicular to the surface.

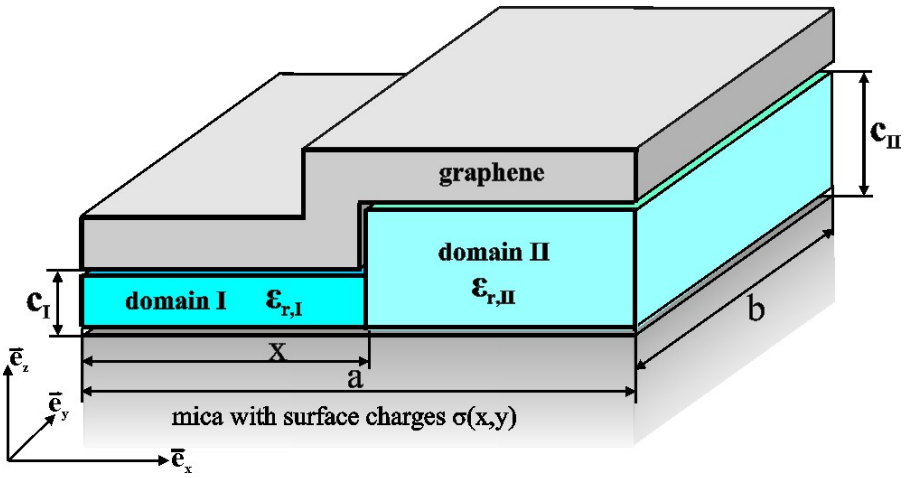

Figure 4.10 The sketch shows the simplified model of the slit pore as an ordinary capacitor with two domains and different heights. The growth of the domains is determined by the variable x for domain I and (a-x) for domain II with the condition that the surface area of mica A = a b = x b + (a - x) b is constant.

The surface charges of mica are not moveable, although the induced charges into graphene can be changed via the dielectric layers. Therefore, the global charges of graphene are dependent on the respective parts of both domains.

$$D_i = \varepsilon_0 \varepsilon_i E_i \quad i \in I, II \qquad [4.9a]$$

and in this special case the electric displacement field **D** is also given by

$$D_i = \sigma_i = \frac{Q_i}{A_i} \qquad [4.9b]$$

The energy W of the capacitor is the integral over the scalar product of the electric field **E** and the electric displacement field **D** and can be simplified by the following equation in the special geometry.

$$W = \frac{1}{2}\int d^3r\, \vec{E}\cdot\vec{D} = \frac{1}{2}(E_I D_I A_I c_I + E_{II} D_{II} A_{II} c_{II})$$

$$W = \frac{A}{2\varepsilon_0}\left[\frac{\sigma_I^2}{\varepsilon_I} c_I (1-\theta) + \frac{\sigma_{II}^2}{\varepsilon_{II}} c_{II}\theta\right] \qquad \text{with } \theta = \frac{x}{a} \qquad [4.10a]$$

The relationship of the energy W and its resultant force is determined by the gradient of this energy.

$$\vec{F} = -\mathrm{grad}(W)$$

and for the x-direction, the force can be written as

$$\vec{F}_x = -\frac{dW}{dx}\vec{e}_x = \frac{b}{2\varepsilon_0}\left(\frac{\sigma_I^2}{\varepsilon_I}c_I - \frac{\sigma_{II}^2}{\varepsilon_{II}}c_{II}\right)\vec{e}_x \qquad [4.10b]$$

Now, it is not surprising that, having presupposed a model of a capacitor, one also has to derive equations of a capacitor, although the focus lies on the parameters and its relations. For the verification of these results (Eq.uation 4.10), the system where each single parameter is varied successively and the others are kept constant should be considered. The squares of surface charges σ_i^2 are included in these equations, whereby the sign of each charge is independent from the force direction and the phenomenological appearance of fractals. When the relation of the surface charges is $\sigma_I < \sigma_{II}$, the total energy W can only decrease if the domain I is displaced through domain II. In the opposite case, $\sigma_I > \sigma_{II}$, the domain II is displaced through the domain I. This fact is also mirrored by the force. In the first case, $\sigma_I < \sigma_{II}$, the total force is positive and thus the force is oriented in the x-direction and in the other case in the (−x)-direction. Since the dielectric is beneath the fraction line, the partial energy becomes smaller the greater the dielectric constant, and vice versa. Therefore, the domain grows the greater the dielectric constant and the greater the dipole moment in the electric field direction. This also applies for the force, i.e. when the domain II has the greater dielectric constant ($\varepsilon_I > \varepsilon_{II}$), it cannot be displaced through the domain I. Since the real height differences Δc are small, the effects on the energy and force are also small.

4.2.1.4 Conclusion

The work in this section covered the investigation of the mica-graphene interface with the STM, where the amount of intercalated water could be adjusted via the relative humidity. While recent publications on this topic use SFM and Raman spectroscopy, exclusively providing phenomenological descriptions, the STM investigation revealed the same characteristic phenomenon. At relative humidity below 4 %, the fractal growth process is started. This describes a process where the water in the graphene-mica interface (slit pore) is removed, thus leaving the fractal structure which is nothing more than defects which were replaced by the lowered graphene. It was not obvious until now why the growth stopped at a certain, total fractal size, independent of the size of the graphene piece and the aggregate state of the water, as well as how many layers are there on mica and therefore in the slit pore. Based upon theoretical as well as experimental data, it must be assumed that the mica has a strongly charged surface, which differs in sign and strength according to the coverage with potassium ions. The graphene that lies on top constitutes a conductive layer which adapts the underlying charge distribution according to the model of mirror charges. The charge distribution changes the local density of state (LDOS) of graphene. The STM measures the spatially resolved LDOS, whereby it could be assumed that the sign of the charges or at least the different orientations of the dipoles of water can be measured indirectly. In contrast to the SFM measurements where only one homogeneous depth of fractals was measured, two distinguishable depths could be significantly measured with the STM. Based upon the results of this work and the theoretical and experimental results presented in other publications, it was possible to develop a model that can explain the wetting and dewetting phenomenon of fractals as well as the idea that the water dipoles and its domains have a different alignment relative to each other. The model is based upon a plate capacitor with different distances and different dielectric constants for the corresponding domains. Since the graphene is in the near field of the mica surface charges, there is a very strong electrical field strength of about 10^9 V/m. The model revealed that the phenomenon of fractal growth is independent of the sign of the surface charges.Based on the strong electrical field strength, the growth of fractals may be stopped independent of the size of the graphene piece, when the energy of the capacitor is larger than the thermal energy kT of the water layers. Furthermore, the assumption has to be made that the number of water layers is larger than only one. In contrast, the assumption suggests that the graphene ought to be adsorbed onto the "pure" mica surface in the fractals based on the AFM measurements. However, if the mica surface and the water layer also dope the graphene with the corresponding different sign, the respective measurements would have to reveal this fact. Nonetheless, the results of the Raman

investigation revealed the same sign. Furthermore, the STM measurements have shown different heights (depths) of fractals, which may be described with a further water layer where the dipole moments have different alignments, whereby the graphene is slightly differently doped but with the same sign, which is in accordance with the results from the Raman measurements.

4.2.2 Controlling the Electrical Transport through Single Molecules and Graphene

4.2.2.1 Introduction

Functionalized surfaces are of particular interest not only for research but also for the economy and medicine, since they offer a wide field of applications as, for example, transistors, sensors, tools for medical diagnosis and therapy and many more. The customized implementation of (multi-) functional elements and structures is one of the most important ideas behind the functionalized surfaces, to cope with many challenges. For the implementation of these ideas the knowledge about the basic mechanisms is essential. The hybrid types of inorganic and organic systems form a sub-category of the functionalized surfaces. The roles which both play are mostly versatile and dependent on the application and challenges. The objects of this work were hybrid systems of inorganic substrates that establish the basic structure, where functionalized macromolecules are physically or chemically adsorbed via self-assembly. The used macromolecule, namely the porphyrin-spiropyran-dyad, was synthesised with significant functions, e.g. special properties of the functional unit (the switch spiropyran) and tuning of self-assembling and its suitable spacing for the switch. Nevertheless, the functional unit - an optically switchable spiropyran derivative - might be more or less strongly affected, inter alia, by its substrate as well as neighbouring dyads, in which the effect of different solvents initially remains disregarded. One of the most difficult issues was the prediction of the cumulative effect of all influences on the behaviour of the dyad and its properties. For this purpose, the dyad has been investigated in two different systems, either dissolved in solution with a suitable low concentration or adsorbed onto surfaces of graphene and HOPG. The former approach was carried out by Chandan Maity, who had also synthesised the porphyrin-spiropyran-dyad in use and the results are presented and discussed above. Thus, the following chapter deals with the behaviour of dyads adsorbed and immobilised from the solution and the concluding discussion of both results.

4.2.2.2 Photo-Switching Behaviour of the Dyad adsorbed onto the Surface

For the investigation of the photo-switching behaviour of the porphyrin-spiropyran dyad, adsorbed onto (multi-layer) graphene, the above-described setup (chapter 3.3) was used where the STM was extended with a reflected light microscope (AXIO Observer A1m, Zeiss). A band pass transmission filter was used at λ_{max} = 365 nm, a two-way mirror 20/80 (20 % transmission, 80 % reflection to the sample), optimized for the 365 nm wavelength. The light source was a low-pressure Hg lamp, whereby the 365 nm line was used. Therefore, an incident light power density

onto the top side of sample (adsorbed dyad layer) of (394 ± 51) mW/cm² was achieved, which was primarily dependent on the thickness of mica pieces (compare chapter 4.1.2). Additionally, two polarizers crossed by 90° (as explained above) with a 50/50 two-way mirror was used during the STM tip approach for the optical support. The used graphite (HOPG grade ZYB, Advanced Ceramics) was cleaved freshly before each measurement and a separate graphite was also used for each of the solvents. The preparation and the properties of the GMQ sample were already described in detail above (chapter 4.1). For the investigation of the lattice structure of the dyad 1-phenyloctane was used and for the switch experiments 1-octanol (both Sigma Aldrich).

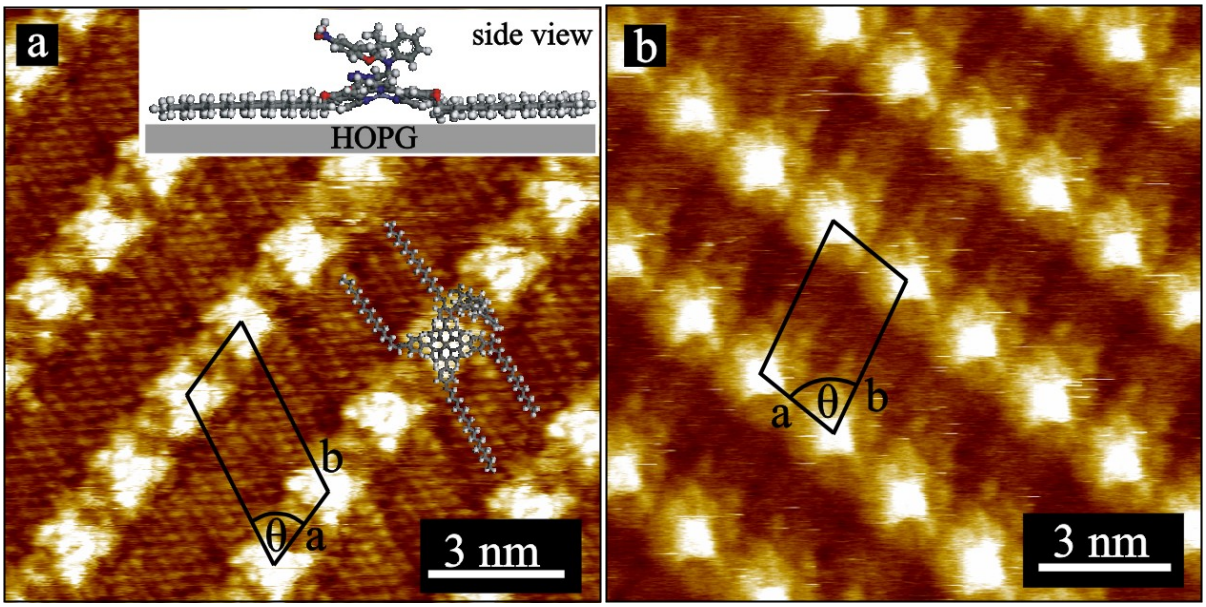

Figure 4.11 STM height image of **a)** the porphyrin-spiropyran dyad and a side view (inset, designed by MS Modelling) of a model of dyad adsorbed on graphite (HOPG) and **b)** ZnTPP under the same conditions as a); both unit cells are equal. Parameters for a) U= –58.7 mV, I = 63.3 pA, LG = 4.97 % and b) U = –0.67 V, I = 19.1 pA, LG = 10.0 %.

The dyad was also synthesized with the intention that the anchor porphyrin should adsorb onto the surface and the switch spiropyran is directed into the solution, away from the surface to allow an unaffected switch without e.g. a steric hindrance. Hence, the first step aimed to determine the lattice structure of the adsorbed dyad onto the surface. The 1-octanol features a weak electrical conductivity, which is also superimposed by the tunnelling current and thus degrades the sub-molecular resolution. For this reason, the solvent 1-phenyloctan was used at first as well as graphite. The latter was used because it has the same lattice structure as graphene and allows to carry out measurements of the lattice structure much more frequently, with the highest possible resolution. In order to clarify the position of the switch spiropyran, the dyad and ZnTPP (zinc-

tetraphenylporphyrin without spirpyran) were measured at equal conditions. The STM measurements were carried out in a droplet of solution (solid-liquid interface). The analysis of the ZnTPP was based upon five images and the dyad with the switch was based upon eight records. Representative height images of the dyad with (a) and without the switch (b) are shown in Fig. 4.11. The analysis of these images exhibit a bright rectangular pattern for both cases, arranged in rows. This characteristic may be identified as the porphyrin unit cell. The gaps between the rows of porphyrin exhibit an alternating contrast of dots (Fig. 4.11 a). This pattern looks like adsorbed alkyl chains with a head group, where the distance of the alkyl chains is not correlated with the pattern of the graphite and thus the LDOS is different. Due to the estimated maximum length of the side chains of the dyad of 2.4 nm (MS Modelling) and the gap width - which is smaller than (2.8 ± 0.3) nm, it is assumed that the side chains are completely extended and lie perpendicular to the porphyrin rows. The scaled model of the dyad with switch confirmed and illustrated this assumption (see Fig. 4.11a). The analysis of the unit cells revealed the results listed in Tab. 4.5:

Table 4.5 The unit cell of the dyad in comparison with the unit cell of the ZnTPP. Both unit cells are identical, whereby it can be recognized that the switch spiropyran of the dyad is not adsorbed onto the surface.

	a **[nm]**	**b** **[nm]**	**θ** **[°]**	**A** **[nm²]**
ZnTPP	1.9 ± 0.1	3.5 ± 0.2	76.4 ± 3.8	6.5 ± 0.3
dyad	1.9 ± 0.1	3.4 ± 0.2	78.7 ± 3.9	6.4 ± 0.3

In the table, parameters are given for each unit cell: **a** as the small and **b** large vector length, θ the enclosed angle and A the enclosed area. The comparison of the two unit cells - shown in Fig. 4.11 – revealed that the switch is not adsorbed on the surface, because otherwise it would be necessary to assume that the dyad with an adsorbed spiropyran has a larger unit cell, which was not the case. In fact, the unit cells have the same size. Therefore, it has to be assumed that the switch was directed into the solution, away from the surface, and that the switch was not steric hindrance. However, the relative position of the moveable spiropyran to its adsorbed anchor porphyrin could not be observed by the STM with scan speeds of 210 nm/s in the fast and 0.2 nm/s in the slow direction. The energy levels of spiropyran are out of the applied gap voltage of the STM in relation to the Femi level (relative energy levels will be described in the following paragraph). This point remained unknown.

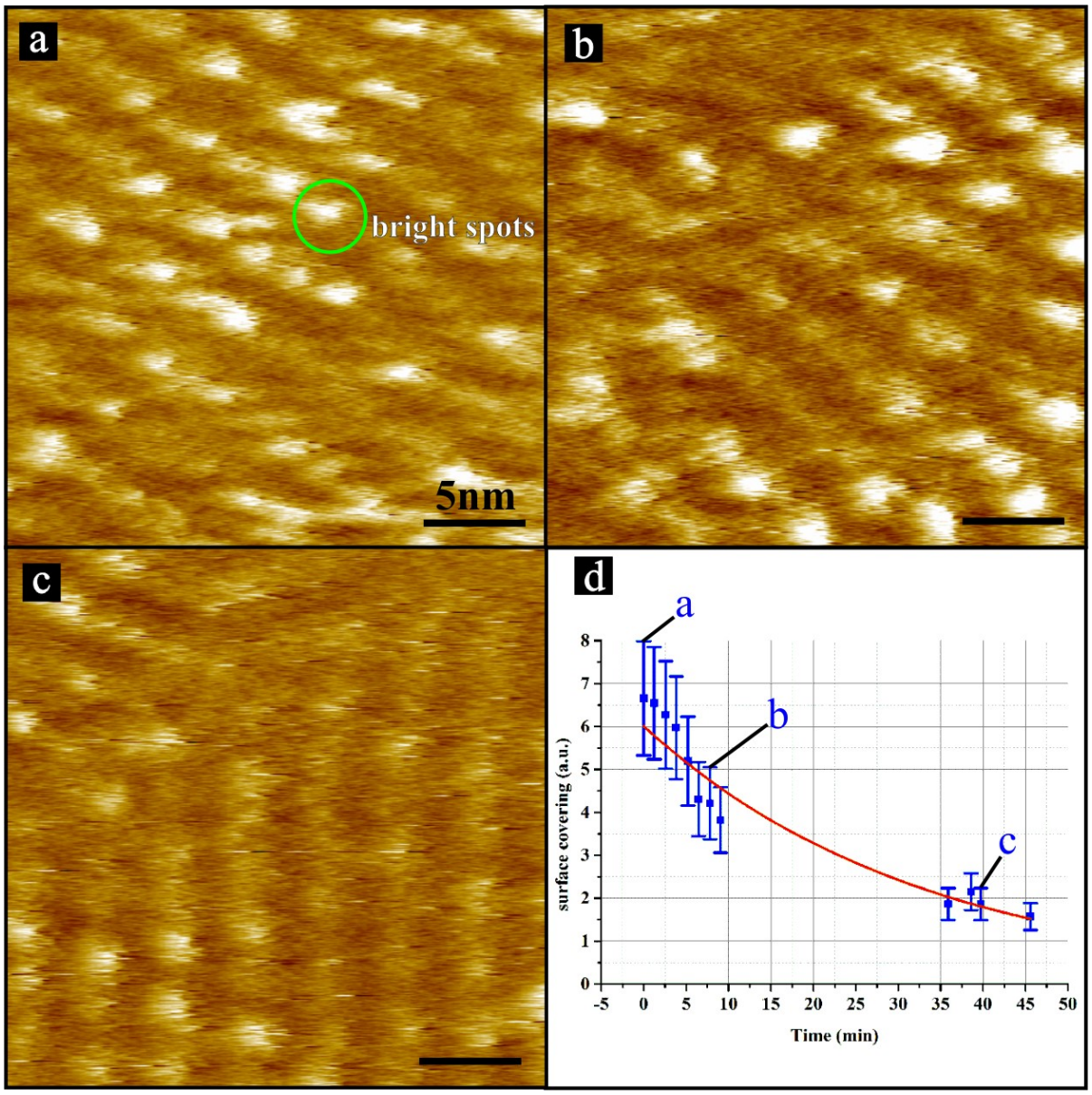

Figure 4.12 STM height images of **a**), **b)** and **c)** the porphyrin-spiropyran-dyad after illumination at 365 nm and **d**) the mean value of surface covering (a.u. unit) of bright spots over the time (min) due to the measured sequence of STM height images like a), b) and c). During the measurements, the light was switched off. All measurements were carried out at the same parameters U = –0.69 V, I = 8.3 pA, LG = 31.6 %.

The switch experiments - which also include the immediate preparation - were carried out solely in darkness and at room temperature (about 16 - 23 °C, testo 635 of Testo GmbH). The darkness was important as the light sensitive dyad should not be at risk of switching via external light sources, neither during the immediate preparation nor during the measurements themselves. The tip was approached and supported via the optical microscope. Following the approach, a relatively large period of waiting time (some 10 min) is required for the minimization of the x-y

drift as well as the z drift, on top of the adjacent multi-layer graphene. Via an octanol resistant syringe, a drop of the dyad dissolved in 1-octanol (c = (9.0 ± 0.5) $\times 10^{-4}$ mol/l) was dropped very gently onto the surface close to the tip, while the lamp of the monitor donated sufficient light. Finally, the setup could be changed to the filter set optimized for 365 nm and the intensity from the Hg lamp, already at the operating temperature, could be changed according to necessity via a shutter and the variable iris diaphragm. After the illumination at 365 nm, chronological images - represented in Figure 4.12 a), b) and c) - showed bright dyads whose number decreased with time. The time constant of the thermal back reaction is determined by

$$y(t) = y_0 \cdot \exp\left(-\frac{t}{\tau}\right). \qquad [4.11]$$

Here, is y(t) the time-dependent number of switched dyads, y_0 the approximated number of switched dyads at the start time, t the time and τ the time constant. The equation implies a complete back reaction from merocyanine to spiropyran. The evaluation determined a time constant of the thermal back reaction of τ = (33.1 ± 2.7) min. For comparison, the time constant of the solute was τ = (35.7 ± 1.8) min, thus reflecting no significant difference. The exact reason for the bright contrast of the switched dyads could not yet be clarified, although one may assume that the optical switching of spiropyran will cause a change of its dipole moment (spiropyran 3-5 D and merocyanine 15-18 D). Due to the nature of the STM measurement, there is an "external" electric field between the STM tip and the surface, which is influenced by the HOMO LUMO levels of the adsorbed dyads as well as the dipole moments of the open and closed switch. The gap voltage between tip and surface causes unoccupied levels on the one side and occupied levels on the opposite side, causing the tunnelling current at the corresponding distance. The molecular energy level lying in between the gap voltage can also cause a resonant tunnelling current. The dipole moments also have an impact on the tunnelling current through an additional electrostatic field, depending on its orientation. The requirement is that several energy levels of the dyad - which are closer to graphene than to the tip - are close to the Fermi level of graphene as well as in the range of the applied gap voltage. In the above chapter, it was discussed that the adsorption spectra in solution provides an indication that the energy levels of the porphyrin and spiropyran together - as a dyad - are equal to its separated forms. The starting point is the work function of graphene on water layer(s) and mica, which has been experimentally determined to 4.70 eV (HOPG has 4.6 eV, STM tip: work function of pure Pt ~ 5.32 V, Ir ~ 5.30 eV, Pt80 / Ir20 is unknown).

Based upon the absorption spectra of the spiropyran, the relative HOMO-LUMO gaps can be determined by

$$E\,[eV] = \frac{hc}{\lambda e}. \qquad [4.11]$$

Here, *E* is the energy gap of the absorption band gap in eV and *h*, *c*, and *e* the Planck constant, light velocity and elementary charge, respectively. Therefore, the lowest energy gap of the spiropyran is determined as E (λ = 430 nm) = 4.6 eV. By contrast, the lowest energy gap of merocyanine is determined as E (λ = 650 nm) = 3.1 eV. Even if the porphyrin is adsorbed onto the graphene as a 2D crystal, the absorption spectra should serve to estimate the relative energy level relative to the graphene at first. Thus, the energy gap of the porphyrin derivative is determined as E (λ = 625 nm) = 3.2 eV. The used STM gap voltages were about –0.5 V to –0.7 V. The negative voltage means the sample had an excess of electrons opposite to an electron deficiency of the Pt/Ir tip. These energy values can now be compared with the literature for the evaluation and interpretation (compare Fig. 3.8 and 4.13). The first molecule should be the metal tetraphenylporphyrin (MTPP, ZnTPP). According to Lioa and Scheiner [116], the TPP has a HOMO level (a_{2u}, ~ 4.1 eV) above and a LUMO level (a_{1u}, ~ 4.8 eV) closely below the Fermi level of HOPG (4.6 eV). Through the additional zinc atom, the a_{2u} goes to the HOMO level (4.1 eV to 4.7 eV) very close to the Fermi level and the a_{1u} state is now the $HOMO^{+1}$ (4.7 eV to 5.0 eV). Additionally, there are five d orbitals from the zinc atom (d_{xy}, d_{xz}, d_{yz}, d_{z^2} and $d_{x^2-y^2}$). Two of them are in the range of the gap voltage of the STM, the b_{1g} ($d_{x^2-y^2}$) and the doubly degenerate level $1e_g$ (d_π), which is close to b_{2u}. The doubly degenerate level $2e_g$ is the new LUMO level (2.2 eV) and thus far away from the Fermi level. For the ZnTPP, a HOMO-LUMO gap emerges at 2.49 eV in relation to UHV. One has to note that there is a very strong hypochromic shift of the energy level and the band gap by the dipole moment of the solvent 1-octanol (1.8D). The comparison with the vacuum-like situation shows a shift of peak maxima of about Δλ = 120 nm, resulting in a band gap of about E (λ = 810 nm) = 2.45 eV ("Chemistry and Applications of Leuco Dyes" [147]), in good agreement with the theoretical value. The second molecule is the spiropyran and the merocyanine. As an orientation, one may start with the publications of Minkin [38], Sheng et al [120] and Bronner et al. [121]. The latter described the relative position of the energy level of an adsorbed nitro-spiropyran on an Au[111] surface. The Au[111] surface has a work function of about (5.3 - 5.5) eV and a large band gap in contrast to that of HOPG or graphene. This work function is very sensitive to the surface dipole moments [148] (5.15 eV with SP and 4.71 eV with MC). The relative position of the energy level of SP and MC can be only estimated, because there are no comparable

publications. However, because the HOMO levels of SP (1.54 eV) and that of MC (1.77 eV) are below the Fermi level, one may assume that the HOMO levels have the same relative position to the Fermi level of HOPG (4.6 eV) and graphene (4.7 eV) and thus are also not between the gap voltage of −0.68 V. The same also applies to the LUMO levels. In conclusion, it may be assumed that the SP as well as the MC have not contributed to the resonant tunnelling effect and thus have not directly affected the contrast in the STM images. In addition, this matter is further aggravated because the local dipole moment changes via the isomerisation, also changing the relative position of the energy level of its molecule. The approximation can be written as

$$\Delta\varphi[\mathrm{eV}] = \frac{\mathrm{n}\mu\,\sin(\theta)}{\varepsilon_0\varepsilon_\mathrm{r}}. \qquad [4.12]$$

Here, n is the dipole density of the SP or MC, respectively, , μ the strength of the dipole moment, sin(θ) the horizontal part of the dipole moment to the surface, ε_0 the dielectric constant and ε_r the dielectric constant of the adsorbed molecule (ZnTPP). For approximation, one may take the results of Fukagava et al., in which the dielectric number of OTi-phthalocyanine (OTiPC) on HOPG was determined to ε_r =1.22. With a range of $1 < \varepsilon_r < 5$, one assumes that the energy shift is approximately about 87 meV < Δφ < 435 meV. These strong values are based upon the strong dipole moment change from SP to MC. The results of the discussion above are shown in Fig. 4.13.

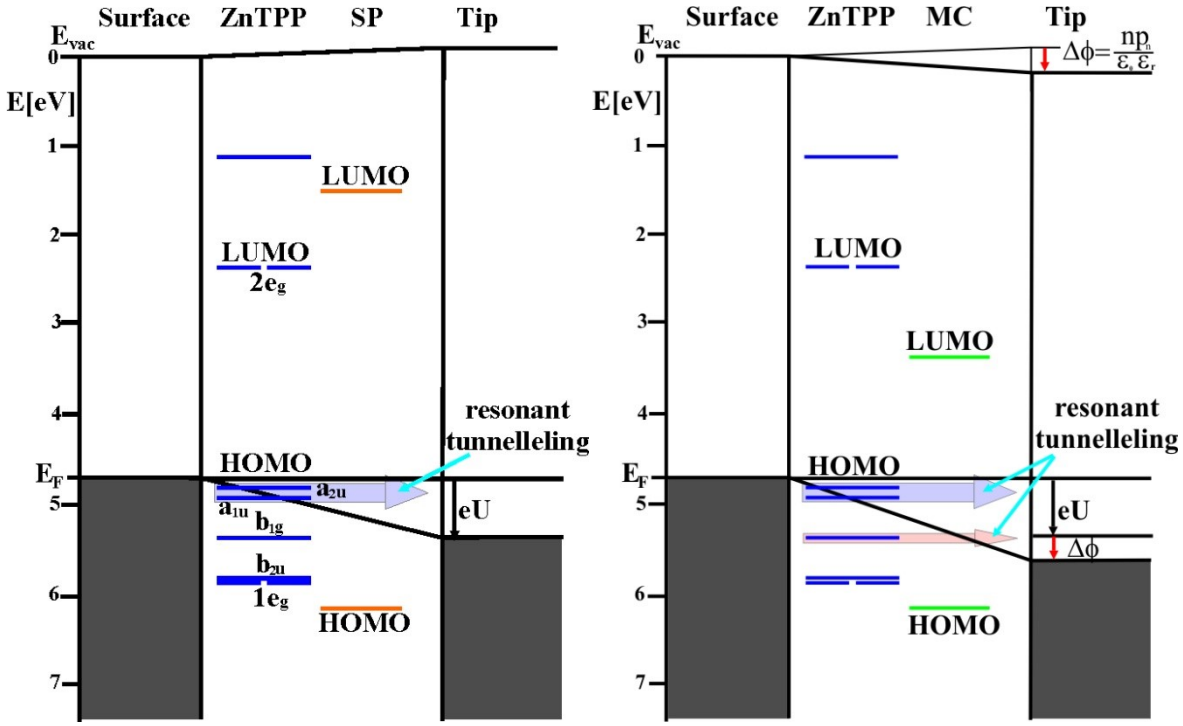

Figure 4.13 Energy scheme for the one explanation of the bright contrast after the illumination (spiropyran to merocyanine). Left (spiropyran-like): gap voltage ΔU of the STM is sufficiently strong for the resonant tunnelling through the energy level of the dyad; right (merocyanine-like): the additional gap voltage ΔU_{dipole}, due to the stronger dipole moment of the merocyanine, results in an additional resonant tunnelling through the dyad energy level.

A further explanation is based on the stacking character of spiropyran and merocyanin to each other [120–125, 127, 129]. Spiropyran has a quite strong dipole moment of about 3 -5 D [119] (water 1.85 D), as well as a turned geometry (not planar), whereby the molecules cannot stack, because the process is sterically hindered. The process of aggregation is different to merocyanine. The isomer is available in a stretched form with a high probability and has a very strong dipole moment of about 15 – 18 D. The stack is thus not sterically hindered and the strong dipole moment significantly supports the aggregation process. The dyad is a composition of the porphyrin and the spiropyran as well as the merocyanine isomers. The aggregation can only comprise a dimer. From geometrical considerations, one has to recognize that the dimer is flanked through the porphyrins from two opposite sides, whereby a third dyad cannot aggregate in addition to the dimer. In the case of adsorbed dyads at the solid-liquid interface where these are arranged in dense packing, the dissolved and freely moveable dyads can only aggregate with the adsorbed dyads if both molecules are available in their stretched merocyanin form (Fig. 4.14). The STM

measurement thus only measures the height differences between the dimers and the monomers, whereby the bright spheres are the dimers and the dark regions constitute the monomers.

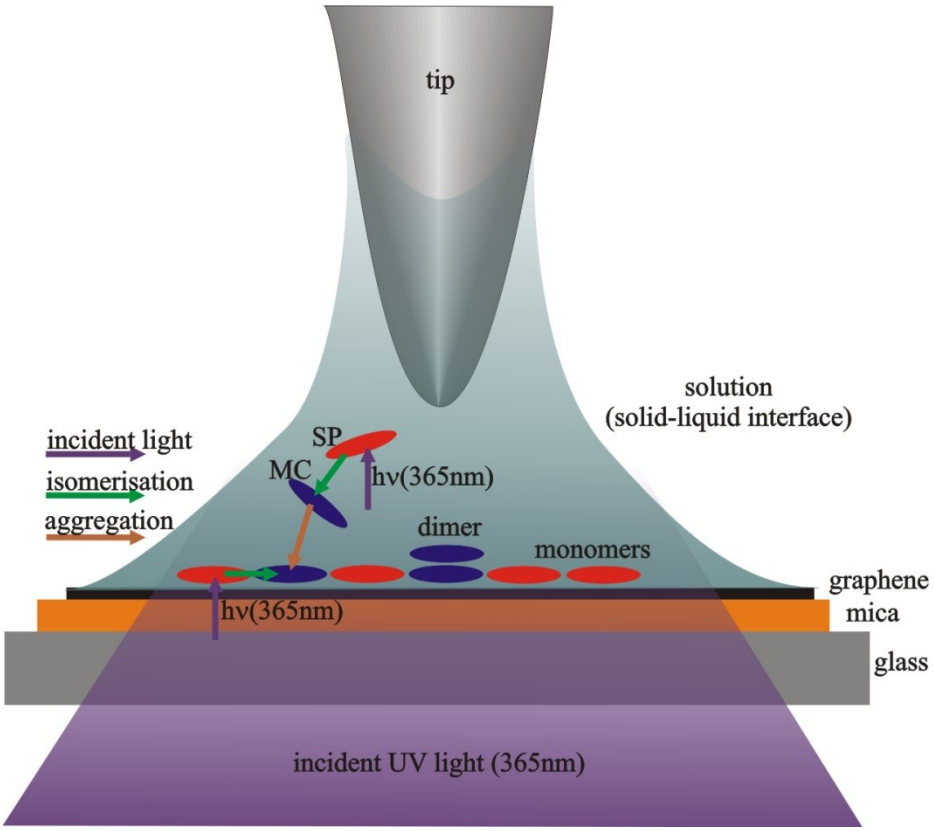

Figure 4.14 The illustration explains the process of stacking. At the beginning, there are only dyads in the spiropyran (SP-dyad) form (red). During the irradiation of adsorbed SP-dyads as well as the solutes with light of 365 nm, the SP-dyad becomes the dyad with the merocyanin isomer (MC-dyad; dark blue). Only two MC-dyads can aggregate on each other. On the surface, there are dimers and monomers due to the irradiation.

4.2.2.3 Conclusion

In this chapter, the aim was to investigate the switching behaviour of an adsorbed porphyrin-spiropyran dyad in a solid-liquid interface with a STM, where the SP is the switch and porphyrin the anchor. For this purpose, the dyads were dissolved in 1-octanol and deposited with a solute-solvent drop onto graphene, where a balance was established between dissolved and adsorbed dyads. It could be shown that the switch of the dyad was not adsorbed onto the surface. Rather, the switch pointed away from the surface and hence into the solvent. This state had the advantage over the conceivable state of an adsorbed switch, that there is no steric hindrance during the switch process through the near to the surface. During the irradiation with light at 365 nm, the spiropyran form was transformed to the corresponding merocyanine form. After the irradiation, the STM measurements revealed a change in the brightness of the spherical molecules. Regardless of conceivable explanations for this phenomenon at first, the same thermal back reaction time of adsorbed molecules ($\tau = 33 \pm 3$) as that of the solute ($\tau = 36 \pm 2$) could be determined. It should be assumed that the dyad on the surface switched through the irradiation as well as switched back again in darkness. In terms of explanations, there are two conceivable possibilities: at first, the resonant tunnelling effect through additional molecule orbitals caused by the dipole change from spiropyran (3-5 D) to merocyanine (15-18 D) and at second, the stacking character of the dyad (dimers) which is only feasible if the dimer is formed by two dyads in the stretched and planar merocyanine form. It should be noted that the indication of identical time constants does not imply that the influence is on the solute system is also identical.. In fact, it has to be stated that all conceivable influence factors of this complex system compensate each other, i.e. the “identical” time constants have to be considered as identical in terms of their averaged statistical fluctuations.

5. Summary and Outlook

Nanotechnology will become a key technology in the future. Both microelectronic technologies as well as medical products for diagnostics and therapy already show the enormous potential of a development, in which the miniaturization of materials and functional units allow a precise design and functionalisation. However, with this development, physical phenomena such as the surface and interface physics gain in importance. The study of these interfaces goes hand in hand with appropriate and convenient measurement methods by which the interfaces can be detected with atomic resolution and their dynamics can be analysed.

The first part of this work deals with the STM investigation of an interface in the surrounding natural atmosphere, which is formed by the adsorption of the conductive graphene onto a freshly-cleaved mica surface and which is characterised by a local carrier density. In this interface (slit pore), an a few angstrom thin water layer was formed by the surrounding humidity. By varying the relative humidity, the slit pore is rewetted, dewetted and manifests itself in star-shaped, growing fractals where the height of graphene is approximately decreased by the diameter of a water molecule. The STM investigation - which is primarily sensitive to the density of states of graphene – had shown that additional, significant changes in the density of states of graphene are formed within the fractal, unlike in the SFM investigations. This suggests that the water layers are subdivided in water domains with the same height in the slit pore, where the fractals lie upon. The slit pore also affects the LDOS of graphene differently via the polarisation alignment of these water domains. However, this is equivalent to the assumption that there are two or more water layers, whose polarisation varies both regarding its alignment and distribution, respectively.

The further investigation of this system should be continued using liquids with slightly up to distinctly different geometries, dipole moments (alignment) and dielectrics. The measurement methods should be primarily AFM, Raman and, under certain preconditions, surface enhanced NMR spectroscopy. The obtained phase diagrams may reveal dependencies between physical variables.

The second part of this work deals with a functionalized surface, characterised by a functionalized dyad adsorbed onto graphene at a solid-liquid interface, which was also investigated by STM. This dyad essentially comprises a zinc-tetraphenylporphyrin (ZnTPP) and is connected with a spiropyran derivative via a flexible linker. This changes its conformation through irradiation with light with a suitable wavelength. In that way, the dipole moment is also strongly changed, whereby the behaviour could be investigated with an STM at a solid-liquid interface. It was found that the

switching behaviour of a graphene-based conductive surface is comparable with the switching behaviour of a dyad which itself can move freely in solution.

Even though the switch has been shown, the true reasons and mechanisms which caused the measured STM signals, are concealed.. There are three possible ideas for an explanation, which might not be necessarily independent of each other. The three separate mechanisms are : i) the Fermi level shift by the additional dipole moment (see Eq. 4.12); ii) the stacking effect on the surface of the dyad (dimer) by the stretched merocyanine which has a strong dipole moment; and iii) the central ion Zn^{2+} of the ZnTPP could form a complex bonding (octahedral six-fold coordination) with the merocyanin, whereby the energy level of the dyad will be shifted (compare it with the spin-stateswitch, and spin-crossover of azopyridine-substituted Ni-porphyrins, respectively). Here, further measurement methods should be performed in the UV/VIS, as fluorescence spectroscopy and magnetic resonance imaging which are carried out in solution and on the assumption that the mentioned three phenomena also exist in the two systems (as solute and on the surface).

List of abbreviations

ITRS - International Technology Roadmap of Semiconductors
STM - Scanning tunnelling Microscope
SFM - Scanning force Microscope
SPM - Scanning probe microscope
LDOS - local density of state
RH - relative humidity
TD - top-down
BU - bottom-up
mRNA - messenger Ribonucleic acid
HOPG - Highly oriented pyrolytic graphite
ZnTPP - zinc-tetraphenylporphyrin
SP & MC - are the isomers Spripyran SP and Merocyanine MC
EA - electron affinity
IE - ionisation energy
EN - electronegativity
vdW - van-der-Waals
FWHM - full width of half maximum
AD - analogue digital (amplifier)
eV - electron voltage
GMQ - graphene mica quartz glass (sample)
G, H, S, T, μ, N - thermodynamic variable: Gibbs energy, enthalpy, entropy, temperature, chemical potential, number of molecules; respectively
LUMO - Lowest Unoccupied Molecular Orbital
HOMO - Highest Occupied Molecular Orbital
LG - Loop Gain
v - scan speed
c - object cut out in μm in the STM scan window
g - grid number of the STM scan window
R_i - resolution of STM
S_i - roughness; rms
f - frequency
t - time constant
PTE - periodic table of elements

Danksagung

Keine wissenschaftliche Arbeit ist wohl wirklich unabhängig; es erfordert sowohl finanzielle und materielle Mittel, als auch intellektuelle Unterstützung. Zum Ende kommt der Moment, da man all jenen Dank sagen sollte, die nicht nur jene Arbeit zu dem gemacht haben, die sie geworden ist, sondern auch jenen danken, die einen selbst geprägt und geformt haben, welches eben nicht aus den schriftlichen Arbeiten geschlussfolgert werden kann; oder wie Aristoteles schrieb "Das Ganze ist mehr als die Summe seiner Teile"[1]. Meine Wahl zur experimentellen Physik ist wohl eher damit begründet, da alle Erkenntnis mit der sinnlichen Wahrnehmung anhebt und so zur Erfahrung wird[2], aber allein durch die Vernunft kann der Weg über das Sinnliche hinaus gehen zu apriorischen Prinzipien der Gegenstände. Nur müssen all unsere Produkte unserer Vernunft den Weg in die Welt aus uns zurück finden, um den rechtmäßigen Anspruch, der aus ihren Prinzipien hervorgeht, aufs strengste zu prüfen. Die Faszination die in der experimentellen Physik liegt, ist in der untrennbaren Verbindung im Wirken der Vernunft mit notwenigen praktischen Rechtfertigung ihrer selbst zu begreifen, die Kant so vortrefflich zusammenfasste in dem Satz: "Die Vernunft muß mit ihren Prinzipien, nach denen allein übereinkommende Erscheinungen für Gesetze gelten können, in einer Hand, und mit dem Experiment, das sie nach jenen ausdachte, in der anderen, an die Natur gehen, zwar um von ihr belehrt zu werden, aber nicht in der Qualität eines Schülers, der sich alles vorsagen läßt, was der Lehrer will, sondern eines bestallten Richters, der die Zeugen nötigt, auf die Fragen zu antworten, die er ihnen vorlegt."[3].

Ich danke der Humboldt Universität zu Berlin und der vielen lieben und hilfsbereiten Mitarbeitern, der Deutsche Forschungsgemeinschaft (DFG), jenen des SFB 658 und der Firma JPK Instruments.

Ich danke Prof. J.P. Rabe, Prof. Hecht, Dr. Chandan Maity, PD Dr. Stefan Kirstein, Sabine Schönherr, Evi Poblenz, Lothar Geyer, Hans Scholz (Elektronikwerkstatt), Yvonne Kunath (IRIS) und Dr. Ralf-Peter Blum.

Weiter besonderer Dank gilt Dr. Nikolai Severin, Dr. Hendrik Glowatzki, Manuel Gensler, Dr. Philipp Lange, Dr. Stefan Eilers, Dr. Daniel Trawny, Dr. Vitalij Scenev, Egon Steeg, Valentin

[1] verkürztes Zitat aus Metaphysik

[2] I., Kant; KrV I: " In dem Sinnlichen aber und den Erscheinungen heißt das, was dem logischen Gebrauche des Verstandes vorhergeht, das Erscheinende, dagegen die reflektierte Erkenntnis, welche aus der mittelst des Verstandes erfolgenden Vergleichung mehrerer Erscheinungen hervorgeht, heißt Erfahrung. Der Weg von dem Erscheinen zur Erfahrung führt daher nur durch die Reflexion gemäß dem logischen Gebrauche des Verstandes."

[3] KrV I

Reiter, Bita Rezania, Andre Schilo, Lars Nicolai, Caroline Falk, Jörg Barner, Björn Goldenbogen und meiner ganzen Familie, sowie in Gedenken an meinem verstorbenen Vater.

Eidesstattliche Erklärung

Hiermit erkläre ich, die Dissertation selbständig und nur unter Verwendung der angegebenen Hilfen und Hilfsmittel angefertigt zu haben.
Ich habe mich anderwärts nicht um einen Doktorgrad beworben und besitze einen entsprechenden Doktorgrad nicht.

References

[1] Ladd, T. D. *et al,* "Quantum computers," *Nature*, vol. 464, no. 7285, pp. 45–53, http://www.nature.com/doifinder/10.1038/nature08812, 2010.

[2] S. V. Aradhya and L. Venkataraman, "Single-molecule junctions beyond electronic transport," *Nature Nanotechnology*, vol. 8, no. 6, pp. 399–410, http://www.nature.com/doifinder/10.1038/nnano.2013.91, 2013.

[3] G. Ribes *et al,* "Review on high-k dielectrics reliability issues," *IEEE Transactions on Device and Materials Reliability*, vol. 5, no. 1, pp. 5–19, http://ieeexplore.ieee.org/lpdocs/epic03/wrapper.htm?arnumber=1435384, 2005.

[4] ITRS, "ITRS 2013 Report: System Drivers Abstract," http://www.itrs.net/reports.html.

[5] Gooding, J. Justin, "Advances in Interfacial Design for Electrochemical Biosensors and Sensors: Aryl Diazonium Salts for Modifying Carbon and Metal Electrodes," (en), *Electroanalysis*, vol. 20, no. 6, pp. 573–582, http://onlinelibrary.wiley.com/doi/10.1002/elan.200704124/epdf, 2008.

[6] I. Willner, "Biomaterials for Sensors, Fuel Cells, and Circuitry," (en), *Science*, vol. 298, no. 5602, pp. 2407–2408, http://www.sciencemag.org/content/298/5602/2407, 2002.

[7] O. Yehezkeli *et al,* "Generation of Photocurrents by Bis-aniline-Cross-Linked Pt Nanoparticle/Photosystem I Composites on Electrodes †," (en), *The Journal of Physical Chemistry B*, vol. 114, no. 45, pp. 14383–14388, http://pubs.acs.org/doi/abs/10.1021/jp100454u, 2010.

[8] J. Lee *et al,* "Two-dimensional Layered MoS2 Biosensors Enable Highly Sensitive Detection of Biomolecules," *Scientific Reports*, vol. 4, p. 7352, http://www.nature.com/doifinder/10.1038/srep07352, 2014.

[9] B. Kang, S. Lim, W. H. Lee, S. B. Jo, and K. Cho, "Work-Function-Tuned Reduced Graphene Oxide via Direct Surface Functionalization as Source/Drain Electrodes in Bottom-Contact Organic Transistors," (en), *Advanced Materials*, vol. 25, no. 41, pp. 5856–5862, http://doi.wiley.com/10.1002/adma.201302358, 2013.

[10] J. Huang, X. Zhong, L. Wang, L. Yang, and H. Mao, "Improving the Magnetic Resonance Imaging Contrast and Detection Methods with Engineered Magnetic Nanoparticles," (en), *Theranostics*, vol. 2, no. 1, pp. 86–102, http://www.thno.org/v02p0086.htm, 2012.

[11] M. H. Cho *et al,* "A magnetic switch for the control of cell death signalling in in vitro and in vivo systems," *Nature Materials,* http://www.nature.com/doifinder/10.1038/nmat3430, 2012.

[12] N'Guyen, Thuy T. T. *et al,* "Functional Iron Oxide Magnetic Nanoparticles with Hyperthermia-Induced Drug Release Ability by Using a Combination of Orthogonal Click Reactions," (en), *Angewandte Chemie*, vol. 125, no. 52, pp. 14402–14406, http://doi.wiley.com/10.1002/ange.201306724, 2013.

[13] G. Binnig, H. Rohrer, C. Gerber, and E. Weibel, "Surface Studies by Scanning Tunneling Microscopy," (en), *Physical Review Letters*, vol. 49, no. 1, pp. 57–61, http://link.aps.org/doi/10.1103/PhysRevLett.49.57, 1982.

[14] G. Binnig, Quate, C. F, and C. Gerber, "Atomic Force Microscope," (en), *Physical Review Letters*, vol. 56, no. 9, pp. 930–933, http://link.aps.org/doi/10.1103/PhysRevLett.56.930, 1986.

[15] N. Severin *et al,* "Nanophase separation in monomolecularly thin water-ethanol films controlled by graphene," (eng), *Nano letters*, vol. 15, no. 2, pp. 1171–1176, http://pubs.acs.org/doi/abs/10.1021/nl5042484, 2015.

[16] N. Severin, P. Lange, I. M. Sokolov, and J. P. Rabe, “Reversible dewetting of a molecularly thin fluid water film in a soft graphene-mica slit pore,” (eng), *Nano letters*, vol. 12, no. 2, pp. 774–779, http://pubs.acs.org/doi/abs/10.1021/nl2037358, 2012.

[17] J. Shim *et al,* “Water-gated charge doping of graphene induced by mica substrates,” (eng), *Nano letters*, vol. 12, no. 2, pp. 648–654, 2012.

[18] K. Xu, P. Cao, and Heath, J. R, “Graphene Visualizes the First Water Adlayers on Mica at Ambient Conditions,” (en), *Science*, vol. 329, no. 5996, pp. 1188–1191, http://www.sciencemag.org/cgi/doi/10.1126/science.1192907, 2010.

[19] O. Ochedowski, Bussmann, B. Kleine, and M. Schleberger, “Graphene on Mica - Intercalated Water Trapped for Life,” *Scientific Reports*, vol. 4, http://www.nature.com/doifinder/10.1038/srep06003, 2014.

[20] J. M. Tour, “Top-Down versus Bottom-Up Fabrication of Graphene-Based Electronics,” (en), *Chemistry of Materials*, vol. 26, no. 1, pp. 163–171, http://pubs.acs.org/doi/abs/10.1021/cm402179h, 2014.

[21] F. Schreiber, “Structure and growth of self-assembling monolayers,” (en), *Progress in Surface Science*, vol. 65, no. 5-8, pp. 151–257, http://linkinghub.elsevier.com/retrieve/pii/S0079681600000241, 2000.

[22] A. Ulman, “Formation and Structure of Self-Assembled Monolayers,” (en), *Chemical Reviews*, vol. 96, no. 4, pp. 1533–1554, http://pubs.acs.org/doi/abs/10.1021/cr9502357, 1996.

[23] L. H. Dubois and R. G. Nuzzo, “Synthesis, Structure, and Properties of Model Organic Surfaces,” (en), *Annual Review of Physical Chemistry*, vol. 43, no. 1, pp. 437–463, http://www.annualreviews.org/doi/abs/10.1146/annurev.pc.43.100192.002253, 1992.

[24] F. Schreiber, “Self-assembled monolayers: from simple model systems to biofunctionalized interfaces,” *Journal of Physics: Condensed Matter*, vol. 16, no. 28, pp. R881, http://stacks.iop.org/0953-8984/16/i=28/a=R01?key=crossref.f4e6517105eeab297efeb13b456825de, 2004.

[25] G. Whitesides, J. Mathias, and C. Seto, “Molecular self-assembly and nanochemistry: a chemical strategy for the synthesis of nanostructures,” (en), *Science*, vol. 254, no. 5036, pp. 1312–1319, http://www.sciencemag.org/cgi/doi/10.1126/science.1962191, 1991.

[26] R. Klajn, Stoddart, J. Fraser, and B. A. Grzybowski, “Nanoparticles functionalised with reversible molecular and supramolecular switches,” (en), *Chemical Society Reviews*, vol. 39, no. 6, p. 2203, http://xlink.rsc.org/?DOI=b920377j, 2010.

[27] J. Mielke *et al,* “Imine Derivatives on Au(111): Evidence for “Inverted” Thermal Isomerization,” (en), *ACS Nano*, vol. 5, no. 3, pp. 2090–2097, http://pubs.acs.org/doi/abs/10.1021/nn103297e, 2011.

[28] K. Tamada, H. Akiyama, and T. X. Wei, “Photoisomerization Reaction of Unsymmetrical Azobenzene Disulfide Self-Assembled Monolayers Studied by Surface Plasmon Spectroscopy: Influences of Side Chain Length and Contacting Medium,” (en), *Langmuir*, vol. 18, no. 13, pp. 5239–5246, http://pubs.acs.org/doi/abs/10.1021/la0157667, 2002.

[29] K. Tamada *et al,* “Structure and Growth of Hexyl Azobenzene Thiol SAMs on Au(111),” (en), *Langmuir*, vol. 14, no. 12, pp. 3264–3271, http://pubs.acs.org/doi/abs/10.1021/la971348j, 1998.

[30] S.-H. Hsu, D. N. Reinhoudt, J. Huskens, and A. H. Velders, “Lateral interactions at functional monolayers,” (en), *J. Mater. Chem,* vol. 21, no. 8, pp. 2428–2444, http://xlink.rsc.org/?DOI=C0JM02696D, 2011.

[31] Evans, S. D, Johnson, S. R, H. Ringsdorf, Williams, L. M, and H. Wolf, “Photoswitching of Azobenzene Derivatives Formed on Planar and Colloidal Gold Surfaces,” (en), *Langmuir*, vol. 14, no. 22, pp. 6436–6440, http://pubs.acs.org/doi/abs/10.1021/la980450t, 1998.

[32] J. Hu *et al,* “Competitive Photochemical Reactivity in a Self-Assembled Monolayer on a Colloidal Gold Cluster,” (en), *Journal of the American Chemical Society*, vol. 123, no. 7, pp. 1464–1470, http://pubs.acs.org/doi/abs/10.1021/ja003180l, 2001.

[33] A. Mattiuzzi *et al,* “Electrografting of calix[4]arenediazonium salts to form versatile robust platforms for spatially controlled surface functionalization,” *Nature Communications*, vol. 3, p. 1130, http://www.nature.com/doifinder/10.1038/ncomms2121, 2012.

[34] H. Wang *et al,* “Chain-length-adjusted assembly of substituted porphyrins on graphite,” (en), *Surface and Interface Analysis*, vol. 32, no. 1, pp. 266–270, http://doi.wiley.com/10.1002/sia.1051, 2001.

[35] V. I. Minkin, “Photo-, Thermo-, Solvato-, and Electrochromic Spiroheterocyclic Compounds,” (en), *Chemical Reviews*, vol. 104, no. 5, pp. 2751–2776, http://pubs.acs.org/doi/abs/10.1021/cr020088u, 2004.

[36] J. C. Slater and J. G. Kirkwood, “The Van Der Waals Forces in Gases,” *Phys. Rev,* vol. 37, no. 6, pp. 682–697, 1931.

[37] G. Mie, “Zur kinetischen Theorie der einatomigen Körper,” *Ann. Phys,* vol. 316, no. 8, pp. 657–697, 1903.

[38] R. A. Buckingham, “The Classical Equation of State of Gaseous Helium, Neon and Argon,” *Proceedings of the Royal Society A: Mathematical, Physical and Engineering Sciences*, vol. 168, no. 933, pp. 264–283, 1938.

[39] J. E. Jones, “On the Determination of Molecular Fields. II. From the Equation of State of a Gas,” *Proceedings of the Royal Society A: Mathematical, Physical and Engineering Sciences*, vol. 106, no. 738, pp. 463–477, 1924.

[40] L. Meirovitch, *Fundamentals of vibrations*. Boston: McGraw-Hill, 2001.

[41] M. H. Korayem, N. Ebrahimi, and M. S. Sotoudegan, “Frequency response of atomic force microscopy microcantilevers oscillating in a viscous liquid: A comparison of various methods,” *Scientia Iranica*, vol. 18, no. 5, pp. 1116–1125, 2011.

[42] J. E. Sader, “Frequency response of cantilever beams immersed in viscous fluids with applications to the atomic force microscope,” *Journal of Applied Physics*, vol. 84, no. 1, p. 64, 1998.

[43] Van Eysden, Cornelis A. and J. E. Sader, “Resonant frequencies of a rectangular cantilever beam immersed in a fluid,” *Journal of Applied Physics*, vol. 100, no. 11, p. 114916, 2006.

[44] S. Weigert, M. Dreier, and M. Hegner, “Frequency shifts of cantilevers vibrating in various media,” *Appl. Phys. Lett,* vol. 69, no. 19, p. 2834, 1996.

[45] H. Hölscher, A. Schwarz, W. Allers, U. D. Schwarz, and R. Wiesendanger, “Quantitative analysis of dynamic-force-spectroscopy data on graphite(0001) in the contact and noncontact regimes,” *Phys. Rev. B*, vol. 61, no. 19, pp. 12678–12681, 2000.

[46] R. García and A. San Paulo, “Attractive and repulsive tip-sample interaction regimes in tapping-mode atomic force microscopy,” *Phys. Rev. B*, vol. 60, no. 7, pp. 4961–4967, 1999.

[47] R. Wiesendanger, *Scanning probe microscopy and spectroscopy: Methods and applications*. Cambridge [England], New York: Cambridge University Press, 1994.

[48] D. A. Bonnell, *Scanning tunneling microscopy and spectroscopy: Theory, techniques, and applications*. New York, N.Y.: VCH, 1993.

[49] J. Nicol, S. Shapiro, and P. H. Smith, “Direct Measurement of the Superconducting Energy Gap,” *Physical Review Letters*, vol. 5, no. 10, pp. 461–464, 1960.
[50] I. Giaever, “Electron Tunneling Between Two Superconductors,” *Physical Review Letters*, vol. 5, no. 10, pp. 464–466, 1960.
[51] J. Bardeen, “Tunnelling from a Many-Particle Point of View,” *Physical Review Letters*, vol. 6, no. 2, pp. 57–59, 1961.
[52] J. Tersoff and D. R. Hamann, “Theory and Application for the Scanning Tunneling Microscope,” *Physical Review Letters*, vol. 50, no. 25, pp. 1998–2001, 1983.
[53] J. Tersoff and D. R. Hamann, “Theory of the scanning tunneling microscope,” *Phys. Rev. B*, vol. 31, no. 2, pp. 805–813, 1985.
[54] G. Wentzel, “Eine Verallgemeinerung der Quantenbedingungen f�r die Zwecke der Wellenmechanik,” *Z. Physik*, vol. 38, no. 6-7, pp. 518–529, 1926.
[55] H. A. Kramers, “Wellenmechanik und halbzahlige Quantisierung,” *Z. Physik*, vol. 39, no. 10-11, pp. 828–840, 1926.
[56] D. Nünnecke *et al,* “Electroreduction of Organic Compounds 32. Indirect Electrodehalogenation of Chloroarenes in Methanol Mediated by Nickel Complexes,” *Acta Chem. Scand,* vol. 53, pp. 824–829, 1999.
[57] Q. Zhuang and X. Gao, “Electrochemical studies of tetraphenylporphyrin and vanadyl porphyrin,” *Sc. China Ser. B-Chem,* vol. 40, no. 2, pp. 215–224, 1997.
[58] T. Guena, L. Wang, M. Gattrell, and B. MacDougall, “Mediated Approach for the Electrochemical Reduction of Chlorobenzenes in Nonaqueous Media,” *J. Electrochem. Soc,* vol. 147, no. 1, p. 248, 2000.
[59] K.-J. Paeng, C. Lim, B.-Y. Lee, N. Myung, and I. R. Paeng, “Electrochemical Dechlorination of 1,2,4-Trichlorobenzene Using a Reticulated Vitreous Carbon Electrode,” *Bulletin of the Korean Chemical Society*, vol. 24, no. 9, pp. 1329–1332, 2003.
[60] A. G. Whittaker, “Carbon: a new view of its high-temperature behavior,” (eng), *Science (New York, N.Y.)*, vol. 200, no. 4343, pp. 763–764, 1978.
[61] R. W. Cahn, “Physics of graphite,” *Journal of Nuclear Materials*, vol. 114, no. 1, p. 116, 1983.
[62] H. O. Pierson, *Handbook of carbon, graphite, diamond, and fullerenes: Properties, processing, and applications*. Park Ridge, N.J.: Noyes Publications, 1993.
[63] D. R. Cooper *et al,* “Experimental Review of Graphene,” *ISRN Condensed Matter Physics*, vol. 2012, no. 4, pp. 1–56, 2012.
[64] F. Rozpłoch, J. Patyk, and J. Stankowski, “Graphenes Bonding Forces in Graphite,” *Acta Phys. Pol. A*, vol. 112, no. 3, pp. 557–562, 2007.
[65] M. Flores, E. Cisternas, J. D. Correa, and P. Vargas, “Moiré patterns on STM images of graphite induced by rotations of surface and subsurface layers,” *Chemical Physics*, vol. 423, pp. 49–54, 2013.
[66] D. Bonifazi, S. Mohnani, and A. Llanes-Pallas, “Supramolecular chemistry at interfaces: molecular recognition on nanopatterned porous surfaces,” (eng), *Chemistry (Weinheim an der Bergstrasse, Germany)*, vol. 15, no. 29, pp. 7004–7025, 2009.
[67] K. Tahara *et al,* “Synthesis of dehydrobenzo[18]annulene derivatives and formation of self-assembled monolayers: implications of core size on alkyl chain interdigitation,” (eng), *Langmuir : the ACS journal of surfaces and colloids*, vol. 23, no. 20, pp. 10190–10197, 2007.
[68] P. Samorì, “Scanning probe microscopies beyond imaging,” *J. Mater. Chem,* vol. 14, no. 9, pp. 1353–1366, 2004.

[69] T. Aizawa, R. Souda, S. Otani, Y. Ishizawa, and C. Oshima, “Bond softening in monolayer graphite formed on transition-metal carbide surfaces,” *Phys. Rev. B*, vol. 42, no. 18, pp. 11469–11478, 1990.

[70] S. Siebentritt, R. Pues, K.-H. Rieder, and A. M. Shikin, “Surface phonon dispersion in graphite and in a lanthanum graphite intercalation compound,” *Phys. Rev. B*, vol. 55, no. 12, pp. 7927–7934, 1997.

[71] J. Maultzsch, S. Reich, C. Thomsen, H. Requardt, and P. Ordejón, “Phonon dispersion in graphite,” (eng), *Physical Review Letters*, vol. 92, no. 7, p. 075501, 2004.

[72] Y. Zhang, L. Zhang, and C. Zhou, “Review of chemical vapor deposition of graphene and related applications,” (eng), *Accounts of Chemical Research*, vol. 46, no. 10, pp. 2329–2339, 2013.

[73] D. R. Dreyer, S. Park, C. W. Bielawski, and R. S. Ruoff, “The chemistry of graphene oxide,” (eng), *Chemical Society Reviews*, vol. 39, no. 1, pp. 228–240, 2010.

[74] M. Aliofkhazraei, *Advances in Graphene Science*: InTech, 2013.

[75] C. Lee, X. Wei, Kysar, J. W, and J. Hone, “Measurement of the Elastic Properties and Intrinsic Strength of Monolayer Graphene,” (en), *Science*, vol. 321, no. 5887, pp. 385–388, http://www.sciencemag.org/cgi/doi/10.1126/science.1157996, 2008.

[76] Geim, A. K. and Novoselov, K. S, “The rise of graphene,” *Nature Materials*, vol. 6, no. 3, pp. 183–191, http://www.nature.com/doifinder/10.1038/nmat1849, 2007.

[77] Castro Neto, A. H, F. Guinea, Peres, N. M. R, Novoselov, K. S, and Geim, A. K, “The electronic properties of graphene,” (en), *Reviews of Modern Physics*, vol. 81, no. 1, pp. 109–162, http://link.aps.org/doi/10.1103/RevModPhys.81.109, 2009.

[78] X. Du, I. Skachko, A. Barker, and E. Y. Andrei, “Approaching ballistic transport in suspended graphene,” *Nature Nanotechnology*, vol. 3, no. 8, pp. 491–495, http://www.nature.com/doifinder/10.1038/nnano.2008.199, 2008.

[79] Nair, R. R. *et al,* “Fine Structure Constant Defines Visual Transparency of Graphene,” (en), *Science*, vol. 320, no. 5881, p. 1308, http://www.sciencemag.org/cgi/doi/10.1126/science.1156965, 2008.

[80] H. Tomori *et al,* “Introducing Nonuniform Strain to Graphene Using Dielectric Nanopillars,” *Appl. Phys. Express*, vol. 4, no. 7, p. 075102, 2011.

[81] J. Zabel *et al,* “Raman Spectroscopy of Graphene and Bilayer under Biaxial Strain: Bubbles and Balloons,” *Nano letters*, vol. 12, no. 2, pp. 617–621, 2012.

[82] I. Polyzos *et al,* “Suspended monolayer graphene under true uniaxial deformation,” (eng), *Nanoscale*, vol. 7, no. 30, pp. 13033–13042, 2015.

[83] R. C. Tatar and S. Rabii, “Electronic properties of graphite: A unified theoretical study,” *Phys. Rev. B*, vol. 25, no. 6, pp. 4126–4141, 1982.

[84] Novoselov, K. S. *et al,* “Two-dimensional gas of massless Dirac fermions in graphene,” (eng), *Nature*, vol. 438, no. 7065, pp. 197–200, 2005.

[85] H. Bross, “From Graphite to Graphene: The Confinement of the Fermi Surface to the Line KH,” *ISRN Condensed Matter Physics*, vol. 2013, no. 20, pp. 1–9, 2013.

[86] G. Lee, G. Yang, A. Cho, J. W. Han, and J. Kim, “Defect-engineered graphene chemical sensors with ultrahigh sensitivity,” (ENG), *Physical chemistry chemical physics : PCCP*, 2015.

[87] P. Matyba *et al,* “Controlling the electronic structure of graphene using surface-adsorbate interactions,” *Phys. Rev. B*, vol. 92, no. 4, 2015.

[88] N. Dontschuk *et al,* “A graphene field-effect transistor as a molecule-specific probe of DNA nucleobases,” (eng), *Nature Communications*, vol. 6, p. 6563, 2015.

[89] T. Natsuki, “Theoretical Analysis of Vibration Frequency of Graphene Sheets Used as Nanomechanical Mass Sensor,” *Electronics*, vol. 4, no. 4, pp. 723–738, 2015.
[90] O. Leenaerts, B. Partoens, and F. M. Peeters, “Adsorption of H2O NH3 CO, NO2 and NO on graphene: A first-principles study,” *Phys. Rev. B*, vol. 77, no. 12, 2008.
[91] F. Schedin *et al,* “Detection of individual gas molecules adsorbed on graphene,” (eng), *Nature Materials*, vol. 6, no. 9, pp. 652–655, 2007.
[92] T. Feininger, “Rock-Forming Minerals. 3A. Sheet Silicates: Micas (2nd edition).: By Michael E. Fleet. The Geological Society, London, 2003. xxii + 758 pages. US$209 ($125 to members of GSA, SEPM, AAPG; $104 to members of MSA). Available from AAPG Bookstore, P.O. Box 979, Tulsa, Oklahoma 74101-0979, U.S.A. ISBN 1-86239-142-4,” *The Canadian Mineralogist*, vol. 43, no. 2, pp. 837–838, 2005.
[93] S. Jähnert *et al,* “Melting and freezing of water in cylindrical silica nanopores,” (eng), *Physical chemistry chemical physics : PCCP*, vol. 10, no. 39, pp. 6039–6051, 2008.
[94] Koop, Luo, Tsias, and Peter, “Water activity as the determinant for homogeneous ice nucleation in aqueous solutions,” (Eng), *Nature*, vol. 406, no. 6796, pp. 611–614, 2000.
[95] M. Matsumoto, S. Saito, and I. Ohmine, “Molecular dynamics simulation of the ice nucleation and growth process leading to water freezing,” (eng), *Nature*, vol. 416, no. 6879, pp. 409–413, 2002.
[96] H. Iglev, M. Schmeisser, K. Simeonidis, A. Thaller, and A. Laubereau, “Ultrafast superheating and melting of bulk ice,” (eng), *Nature*, vol. 439, no. 7073, pp. 183–186, 2006.
[97] A. Malani and K. G. Ayappa, “Adsorption isotherms of water on mica: redistribution and film growth,” (eng), *The journal of physical chemistry. B*, vol. 113, no. 4, pp. 1058–1067, 2009.
[98] R. Debbarma and A. Malani, “Comparative Study of Water Adsorption on a H(+) and K(+) Ion Exposed Mica Surface: Monte Carlo Simulation Study,” (eng), *Langmuir : the ACS journal of surfaces and colloids*, vol. 32, no. 4, pp. 1034–1046, 2016.
[99] J. Ma *et al,* “Adsorption and diffusion of water on graphene from first principles,” *Phys. Rev. B*, vol. 84, no. 3, 2011.
[100] M. E. Tuckerman, D. Marx, and M. Parrinello, “The nature and transport mechanism of hydrated hydroxide ions in aqueous solution,” (eng), *Nature*, vol. 417, no. 6892, pp. 925–929, 2002.
[101] J. Tomlinson-Phillips *et al,* “Structure and dynamics of water dangling OH bonds in hydrophobic hydration shells. Comparison of simulation and experiment,” (eng), *The journal of physical chemistry. A*, vol. 115, no. 23, pp. 6177–6183, 2011.
[102] M. Thämer, L. de Marco, K. Ramasesha, A. Mandal, and A. Tokmakoff, “Ultrafast 2D IR spectroscopy of the excess proton in liquid water,” (eng), *Science (New York, N.Y.)*, vol. 350, no. 6256, pp. 78–82, 2015.
[103] O. Markovitch *et al,* “Special pair dance and partner selection: elementary steps in proton transport in liquid water,” (eng), *The journal of physical chemistry. B*, vol. 112, no. 31, pp. 9456–9466, 2008.
[104] G. Cassone, P. V. Giaquinta, F. Saija, and A. M. Saitta, “Proton conduction in water ices under an electric field,” (eng), *The journal of physical chemistry. B*, vol. 118, no. 16, pp. 4419–4424, 2014.
[105] S. T. Bramwell, “Condensed-matter science: Ferroelectric ice,” *Nature*, vol. 397, no. 6716, pp. 212–213, 1999.

[106] S. Wei, X. Xiaobin, Z. Hong, and X. Chuanxiang, “Effects of dipole polarization of water molecules on ice formation under an electrostatic field,” (eng), *Cryobiology*, vol. 56, no. 1, pp. 93–99, 2008.

[107] S. V. Shevkunov and A. Vegiri, “Electric field induced transitions in water clusters,” *Journal of Molecular Structure: THEOCHEM*, vol. 593, no. 1-3, pp. 19–32, 2002.

[108] I. Danielewicz-Ferchmin and A. R. Ferchmin, “Phase diagram of electrostricted H2O at surfaces of electrodes at 273-373 K: electric critical point of water,” (eng), *Chemphyschem : a European journal of chemical physics and physical chemistry*, vol. 6, no. 8, pp. 1499–1509, 2005.

[109] N. Güven, “The crystal structures of 2 M1 phengite and 2 M1 muscovite,” *Zeitschrift für Kristallographie - Crystalline Materials*, vol. 134, no. 1-6, 1971.

[110] G. L. GAINES, “Adhesion and Ion-Exchange between Mica Surfaces,” *Nature*, vol. 183, no. 4668, pp. 1109–1110, 1959.

[111] U. Raviv, P. Laurat, and J. Klein, “Time dependence of forces between mica surfaces in water and its relation to the release of surface ions,” *J. Chem. Phys,* vol. 116, no. 12, p. 5167, 2002.

[112] A. G. Slater *et al,* “Thymine functionalised porphyrins, synthesis and heteromolecular surface-based self-assembly,” *Chem. Sci,* vol. 6, no. 2, pp. 1562–1569, 2015.

[113] I. Destoop *et al,* “'Sergeants-and-Corporals' principle in chiral induction at an interface,” (eng), *Chemical communications (Cambridge, England)*, vol. 49, no. 68, pp. 7477–7479, 2013.

[114] D. den Boer *et al,* “Detection of different oxidation states of individual manganese porphyrins during their reaction with oxygen at a solid/liquid interface,” (eng), *Nature chemistry*, vol. 5, no. 7, pp. 621–627, 2013.

[115] B. Chilukuri, U. Mazur, and K. W. Hipps, “Effect of dispersion on surface interactions of cobalt(II) octaethylporphyrin monolayer on Au(111) and HOPG(0001) substrates: a comparative first principles study,” (eng), *Physical chemistry chemical physics : PCCP*, vol. 16, no. 27, pp. 14096–14107, 2014.

[116] M.-S. Liao and S. Scheiner, “Electronic structure and bonding in metal porphyrins, metal=Fe, Co, Ni, Cu, Zn,” *J. Chem. Phys,* vol. 117, no. 1, p. 205, 2002.

[117] Y. Sheng *et al,* “Comprehensive Theoretical Study of the Conversion Reactions of Spiropyrans: Substituent and Solvent Effects,” *The Journal of Physical Chemistry B*, vol. 108, no. 41, pp. 16233–16243, 2004.

[118] C. Bronner, G. Schulze, K. J. Franke, J. I. Pascual, and P. Tegeder, “Switching ability of nitro-spiropyran on Au(111): electronic structure changes as a sensitive probe during a ring-opening reaction,” (eng), *Journal of physics. Condensed matter : an Institute of Physics journal*, vol. 23, no. 48, p. 484005, 2011.

[119] M. Bletz, U. Pfeifer-Fukumura, U. Kolb, and W. Baumann, “Ground- and First-Excited-Singlet-State Electric Dipole Moments of Some Photochromic Spirobenzopyrans in Their Spiropyran and Merocyanine Form †,” *J. Phys. Chem. A*, vol. 106, no. 10, pp. 2232–2236, 2002.

[120] G. Berkovic, V. Krongauz, and V. Weiss, “Spiropyrans and Spirooxazines for Memories and Switches,” *Chemical Reviews*, vol. 100, no. 5, pp. 1741–1754, 2000.

[121] V. A. Krongauz, “Quasi-Crystals,” *Isr. J. Chem,* vol. 18, no. 3-4, pp. 304–311, 1979.

[122] Y. Lia, J. Zhou, Y. Wang, F. Zhang, and X. Song, “Reinvestigation on the photoinduced aggregation behavior of photochromic spiropyrans in cyclohexane,” *Journal of Photochemistry and Photobiology A: Chemistry*, vol. 113, no. 1, pp. 65–72, 1998.

[123] Y. Onai *et al,* “Colored merocyanine aggregates: long-lived crystals of large size (10-100 .mu.m) and deaggregation of small aggregates in solutions,” *J. Phys. Chem,* vol. 97, no. 37, pp. 9499–9505, 1993.

[124] P. Uznanski, “From spontaneously formed aggregates to J-aggregates of photochromic spiropyran,” *Synthetic Metals*, vol. 109, no. 1-3, pp. 281–285, 2000.
[125] A. K. Chibisov and H. Görner, “Photoprocesses in Spiropyran-DerivedMerocyanines,” *J. Phys. Chem. A*, vol. 101, no. 24, pp. 4305–4312, 1997.
[126] T. Yoshida and A. Morinaka, “Irreversible photochromism of spiropyran films at low temperatures,” *Journal of Photochemistry and Photobiology A: Chemistry*, vol. 78, no. 2, pp. 179–183, 1994.
[127] A. K. Chibisov and H. Görner, “Complexes of spiropyran-derived merocyanines with metal ions: relaxation kinetics, photochemistry and solvent effects,” *Chemical Physics*, vol. 237, no. 3, pp. 425–442, 1998.
[128] H. Görner, “Photochromism of nitrospiropyrans: effects of structure, solvent and temperature,” *Phys. Chem. Chem. Phys,* vol. 3, no. 3, pp. 416–423, 2001.
[129] H. Görner and A. K. Chibisov, “Complexes of spiropyran-derived merocyanines with metal ions Thermally activated and light-induced processes,” *Faraday Trans,* vol. 94, no. 17, pp. 2557–2564, 1998.
[130] M. Gouterman, “Spectra of porphyrins,” *Journal of Molecular Spectroscopy*, vol. 6, pp. 138–163, 1961.
[131] M. Gouterman, G. H. Wagnière, and L. C. Snyder, “Spectra of porphyrins,” *Journal of Molecular Spectroscopy*, vol. 11, no. 1-6, pp. 108–127, 1963.
[132] K. T. He, J. D. Wood, G. P. Doidge, E. Pop, and J. W. Lyding, “Scanning tunneling microscopy study and nanomanipulation of graphene-coated water on mica,” (eng), *Nano letters*, vol. 12, no. 6, pp. 2665–2672, 2012.
[133] N. Severin, M. Dorn, A. Kalachev, and J. P. Rabe, “Replication of single macromolecules with graphene,” (eng), *Nano letters*, vol. 11, no. 6, pp. 2436–2439, 2011.
[134] K. Müller and C. C. Chang, “Electric dipoles on clean mica surfaces,” *Surface Science*, vol. 14, no. 1, pp. 39–51, 1969.
[135] E. Riedel, *Anorganische Chemie,* 6th ed. Berlin, New York: W. de Gruyter, 2004.
[136] R. D. Shannon, “Revised effective ionic radii and systematic studies of interatomic distances in halides and chalcogenides,” *Acta Cryst A*, vol. 32, no. 5, pp. 751–767, 1976.
[137] F. Franks, *Water: A matrix of life,* 2nd ed. Cambridge, UK: Royal Society of Chemistry, 2000.
[138] J. L. Finney, “The water molecule and its interactions: the interaction between theory, modelling, and experiment,” *Journal of Molecular Liquids*, vol. 90, no. 1-3, pp. 303–312, 2001.
[139] A. N. Rudenko, F. J. Keil, M. I. Katsnelson, and A. I. Lichtenstein, “Graphene adhesion on mica: Role of surface morphology,” *Phys. Rev. B*, vol. 83, no. 4, 2011.
[140] O. Leenaerts, B. Partoens, and F. M. Peeters, “Water on graphene: Hydrophobicity and dipole moment using density functional theory,” *Phys. Rev. B*, vol. 79, no. 23, 2009.
[141] Freitas, R R Q, R. Rivelino, Mota, F de Brito, and de Castilho, C M C, “DFT studies of the interactions of a graphene layer with small water aggregates,” (eng), *The journal of physical chemistry. A*, vol. 115, no. 44, pp. 12348–12356, 2011.
[142] M. Odelius, M. Bernasconi, and M. Parrinello, “Two Dimensional Ice Adsorbed on Mica Surface,” *Physical Review Letters*, vol. 78, no. 14, pp. 2855–2858, 1997.
[143] H. Ren *et al,* “Interfacial structure and wetting properties of water droplets on graphene under a static electric field,” (eng), *Physical chemistry chemical physics : PCCP*, vol. 17, no. 36, pp. 23460–23467, 2015.

[144] J. Hu, X. D. Xiao, D. F. Ogletree, and M. Salmeron, “Imaging the condensation and evaporation of molecularly thin films of water with nanometer resolution,” (eng), *Science (New York, N.Y.)*, vol. 268, no. 5208, pp. 267–269, 1995.

[145] D. Beaglehole and H. K. Christenson, “Vapor adsorption on mica and silicon: entropy effects, layering, and surface forces,” *J. Phys. Chem,* vol. 96, no. 8, pp. 3395–3403, 1992.

[146] T. E. Balmer, H. K. Christenson, N. D. Spencer, and M. Heuberger, “The effect of surface ions on water adsorption to mica,” (eng), *Langmuir : the ACS journal of surfaces and colloids*, vol. 24, no. 4, pp. 1566–1569, http://pubs.acs.org/doi/abs/10.1021/la702391m, 2008.

[147] R. Muthyala, *Chemistry and applications of leuco dyes*. New York: Plenum Press, 1997.

[148] P. C. Rusu and G. Brocks, “Surface dipoles and work functions of alkylthiolates and fluorinated alkylthiolates on Au(111),” (eng), *The journal of physical chemistry. B*, vol. 110, no. 45, pp. 22628–22634, 2006.